Study on Production and Reactions of Radiation-induced Defects

in Ceramic Materials

2008

Kimikazu Moritani

Contents

Chapter 1
Introduction

1.1 Backgrounds

The breeding blanket is a key component of the fusion reactor since it involves tritium breeding and energy extraction, both of which are critically important for the development of fusion power. Particularly because of their safety advantages, lithium-containing ceramics such as Li_2O, $LiAlO_2$, Li_4SiO_4 and Li_2ZrO_3 have been recognized as promising tritium breeding materials, and extensive studies have been performed on these ceramics [1-3]. According to the current database, these ceramics exhibit acceptable overall behaviors including thermal, mechanical, chemical and irradiation behavior. However, the materials behavior at high burn-up levels is the issues since the database is still limited to rather low burn-up levels.

In a fusion reactor solid blanket system, tritium breeding lithium ceramics are attacked by high energy neutrons and energetic particles from nuclear reactions, and severe irradiation damage may be expected. The irradiation behavior of lithium ceramics is thus important for the performance assessment of fusion reactor blanket systems. Considering the two functions of blanket systems, which are tritium breeding and energy extraction, the effects of long-term irradiation on tritium release behaviors and microstructural changes of lithium ceramics are of special concern for the design of blanket systems. Then the experimental efforts have been devoted to the irradiation performance testing at higher burn-up levels as seen in the BEATRIX II experiments [4]. Also, fundamental studies on the irradiation behavior of lithium ceramics have been performed in order to understand and control the phenomena [5].

As summarized in Table 1, the formation of the irradiation-induced defects has been observed in various lithium ceramics [7, 8, 11, 13-22]. Irradiation-induced defects of F-type centers, colloidal metals and some other decomposition products have been observed to be formed in lithium ceramics such as Li_2O. Noda et al. have reported the results of electron spin resonance (ESR) and optical-absorption measurements of irradiation-induced defects formed in Li_2O [5-11]. The formation of the F^+ center, which is an oxygen vacancy trapping an electron and has a positive charge, was observed in both Li_2O single crystals and sintered pellets irradiated by thermal neutrons to a fluence of 10^{20}-$10^{23}m^{-2}$. The formation of the colloidal lithium metals was also observed in the sintered pellets irradiated to $10^{23}m^{-2}$ by thermal neutrons, in the single crystals irradiated to $3x10^{20}m^{-2}$ by 100MeV oxygen ions [11] and in the Li_2O samples of the BEATRIX-II experiments [12] which were irradiated to $3.9x10^{26}m^{-2}$ in FFTR for 300 effective full power days at 375°C. Although intensive studies have been performed, the knowledge on the formation conditions of temperature, dose rate and absorbed dose for each species is still insufficient and needs further studies.

For the assessment of tritium release behavior of Li_2O under irradiation, a model reaction scheme has been presented by taking into account the interactions of irradiation defects with tritium [22]. Tritium is produced in Li_2O grains by nuclear reactions and

stabilized in the chemical states of T^+(LiOT) or T^-(LiT).   The tritium species interact with the F^0 centers and O_2 molecules which are predominantly produced at higher temperatures, and diffuse to the grain surface where the following surface reactions take place.

$$LiT + LiT \rightarrow 2\ Li + T_2 \uparrow \tag{1-1}$$
$$LiT + LiOT \rightarrow Li_2O + T_2 \uparrow \tag{1-2}$$
$$LiOT + LiOT \rightarrow Li_2O + T_2O \uparrow \tag{1-3}$$

Tritium is thus released in the form of T_2 or T_2O to the sweep gas.   By taking this reaction scheme, some predictions have been made and compared with the observations in the BEATRIX-II experiment [4, 23-26].   The observed tritium release behavior has successfully been interpreted.

It is important that irradiation defects participate in the reaction mechanisms even at such high temperatures, because material stability will be affected as well as tritium release kinetics.   For the further development of the model, the equilibrium constant and rate constant of each reaction are to be determined.   Such data are still lacking at the present time, and are needed to be determined.   As well as the steady state chemistry, the dynamic behavior of tritium release may be studied for the determination of these constants.

1.2 Scope of the present study

On the backgrounds mentioned above, the present study was performed to understand the mechanism of production and reactions of radiation-induced defects in some typical ceramic materials such as silica and alumina in relation with the effect of irradiation on tritium recovery.

In chapter 2, tritium release kinetics of lithium ortho- and metasilicates with irradiation defects was studied by out-of-pile experiments.   The samples were irradiated with thermal neutrons, and annealed in an infrared furnace under the controlled temperature and sweep gas conditions, and the tritium species released on annealing were removed with a helium sweep gas which contained no or 1% H_2.   The obtained results were discussed by considering the effect of neutron fluence, that is of irradiation defects.

In chapter 3, for the performance assessment of fusion reactor solid breeder materials, the production behavior of irradiation defects in the ternary lithium ceramics of Li_2SiO_3 and Li_4SiO_4 were studied by an in-situ luminescence measurement technique under ion beam irradiation of H^+ and He^+.   For comparison the measurement was also performed with vitreous SiO_2.   The temperature dependence of the luminescence intensity, as well as the transient behavior of the luminescence intensity on temperature changes, were measured, and discussed by considering the production mechanisms and kinetics of the irradiation defects.

In chapter 4, the production behavior of irradiation defects in α-alumina and sapphire was studied by the in-situ luminescence measurement technique under ion beam irradiation of H^+ and He^+.   Similarly to the case of lithium ceramics, the luminescence spectra were measured under ion beam irradiation, and the temperature dependence of the

luminescence intensity was analyzed by considering the production mechanism and reaction kinetics of the irradiation defects.

In chapter 5, the electron spin resonance (ESR) measurement of irradiation defects in vitreous silica was performed. In the case of neutron irradiation of vitreous silica, the effects of the OH content, neutron fluence, and postirradiation isochronal anneal behaviors on the ESR spectra were studied. For comparison, measurements were also performed with the specimens irradiated with ion beams, and the results were discussed by considering the dpa values. In isothermal annealing experiments, sequential reactions of the E' centers with oxygen atoms to form the NBOHCs and PORs were measured to determine the rate constants and activation energies of those reactions.

In chapter 6, the conclusions of these studies are summarized.

References

[1] C. Johnson, T. Kondo, N. Roux, S. Tanaka, D. Vollath, Fusion Engng. Design 16 (1991) 127.

[2] N. Roux, G. Hollenberg, C. Johnson, K. Noda and R. Verrall, Fusion Engng. Design 27 (1995) 154.

[3] H. Moriyama, S. Tanaka and K. Noda, Irradiation Effects in Ceramic Breeder Materials, J. Nucl. Mater. 258-263 (1998) 587-594.

[4] G. W. Hollenberg, H. Watanabe, I. J. Hastings and S. E. Berk, J. Nucl. Mater. 191-194 (1992) 23.

[5] K. Noda, J. Nucl. Mater. 179-181 (1991) 37.

[6] K. Uchida, K. Noda, Y. Tanifuji and S. Nasu, Phys. Stat. Sol. (a)58 (1980) 557.

[7] K. Noda, K. Uchida, T. Tanifuji and S. Nasu, J. Nucl. Mater. 91 (1980) 234.

[8] K. Noda, K. Uchida, T. Tanifuji and S. Nasu, Phys. Rev. B24 (1981) 3736.

[9] K. Noda, T. Tanifuji, Y. Ishii, H. Matsui, N. Masaki, S. Nasu and H. Watanabe, J. Nucl. Mater. 122&123 (1984) 908.

[10] K. Noda, Y. Ishii, H. Matsui and H. Watanabe, J. Nucl. Mater. 133&134 (1985) 205.

[11] K. Noda, Y. Ishii, H. Matsui and H. Watanabe, Radiation Effects 97 (1986) 297.

[12] N. M. Masaki, K. Noda, H. Watanabe, R. G. Clemmer and G. W. Hollenberg, J. Nucl. Mater. 212-215 (1994) 908.

[13] Y. Asaoka, H. Moriyama, K. Iwasaki, K. Moritani and Y. Ito, J. Nucl. Mater. 183 (1991) 174.

[14] V. Grishmanov, S. Tanaka, K. Ogikubo and Q. Hu, presented at REI-9 Conference, Knoxville, TN, USA, Sept. 14-19, 1997.

[15] V. Grishmanov, S. Tanaka and T. Yoneoka, Rad. Eff. Def. Solids 143 (1997) 203-211.

[16] S. Tanaka, D. Yamaki, M. Yamawaki, T. Miyamura and R. Kiyose, Fusion Eng. Des. 28 (1995) 292.

[17] M. H. Auvray-Gely, A. Dunlop and L. W. Hobbs, J. Nucl. Mater. 133&134 (1985) 230.

[18] M. H. Auvray-Gely, A. Perez and A. Dunlop, Philos. Mag. B57 (1988) 137.

[19] Y. Asaoka, H. Moriyama, K. Iwasaki, K. Moritani and Y. Ito, J. Nucl. Mater. 191-194

(1992) 268.

[20] H. Moriyama, T. Nagae, K. Moritani and Y. Ito, Proc. 17th Symp. on Fusion Technology, Rome, Sept. 14-18, 1992, p. 1434

[21] H. Moriyama, T. Nagae, K. Moritani and Y. Ito, Nucl. Instrum. Methods B91 (1994) 317.

[22] K. Moritani and H. Moriyama, J. Nucl. Mater. 248 (1997) 132.

[23] H. Moriyama and T. Kurasawa, J. Nucl. Mater. 212-215 (1994) 932.

[24] T. Kurasawa, O. D. Slagle, G. W. Hollenberg and R. A. Verrall, Fusion Technol. 19 (1991) 931.

[25] D. E. Baker, T. Kurasawa, J. M. Miller and O. D. Slagle, Fusion Technol. 19 (1991) 1640.

[26] T. Kurasawa, O. D. Slagle, G. W. Hollenberg and R. A. Verrall, in: Ceramic Transactions, eds. I. J. Hasting and G. W. Hollenberg, Vol. 27, (American ceramic Society, Westerville, OH, 1991), p. 299.

Table 1-1. Irradiation-induced defects observed in lithium ceramics.

Lithium ceramics	Defects	Methods
Li_2O	F^+	ESR/absorption [8]
	F^0	Luminescence [13-16]
	F_2	Luminescence [13-16]
	F-aggregates	Luminescence [13-16]
	Colloidal Li	ESR [7,11]
$LiAlO_2$	F^+	ESR/absorption [17,18]
		Luminescence [19]
	F^0	Luminescence [19]
Li_4SiO_4, Li_2SiO_3	E'	Luminescence [20,21]
	NBOHC*	Luminescence [20,21]
	peroxy species	Luminescence [20,21]
Li_2TiO_3, Li_2ZrO_3, Li_2SnO_3	F^+	Luminescence [22]
	F^0	Luminescence [22]

Chapter 2
Tritium release kinetics of lithium silicates with irradiation defects

2.1. Introduction

In a fusion reactor solid blanket system, tritium breeding lithium ceramics are attacked by high energy neutrons and energetic particles from nuclear reactions, and severe irradiation damage may be expected. The irradiation behavior of lithium ceramics is thus important for the performance assessment of fusion reactor blanket systems [1]. The effects of irradiation on the tritium release behaviors and microstructural changes of lithium ceramics are particularly important. For a clearer understanding of such effects, we have studied the production behavior of irradiation defects in Li_2O [2,3], $LiAlO_2$ [4], Li_2SiO_3 and Li_4SiO_4 [5,6] by an in-situ luminescence measurement technique under ion beam irradiation. In Li_2O and $LiAlO_2$, it has been confirmed that the F^+ center (an oxygen vacancy trapping an electron) and the F^0 center (an oxygen vacancy trapping two electrons), which are commonly observed in ionic crystals, are formed by irradiation [2-4]. These defects have been found to play an important role in the tritium behavior [7]. Similarly, the irradiation defects of the E' center ($\equiv$Si$\bullet$), the nonbridging oxygen hole center ($\equiv$Si-O$\bullet$) and the peroxy radical ($\equiv$Si-O-O$\bullet$) are produced in Li_2SiO_3 and Li_4SiO_4 [5,6], and are considered to affect the tritium behavior. For comparison, the tritium release kinetics of lithium silicates with irradiation defects has been studied in the present study.

2.2. Experimental

Li_4SiO_4 and Li_2SiO_3 were prepared by solid-state reactions [8]. Lithium carbonate and silica of reagent grade were obtained from Nacalai Tesque, Inc. and were used without further purification. Stoichiometric amounts of the reagents were milled together and calcined above 1100K for 10 h. The formation of each silicate was confirmed by X-ray diffraction after calcination. Pellet-type samples of each silicate, several mm in diameter and about 1 mm in thickness, were sintered at 1300K for 10h and the average grain size was measured by an electron microscope to be around 41.8mm and 43.3 mm for Li_4SiO_4 and Li_2SiO_3, respectively.

The samples were sealed in a quartz ampoule and irradiated with thermal neutrons from the TRIGA MARK II, Rikkyo University, and from the Kyoto University Research Reactor. The irradiation temperature was estimated to be a few tens degrees higher than the room temperature at the highest. After irradiations, tritium release experiments were performed with the usual apparatus. The irradiated samples were annealed in an infrared furnace under the controlled temperature and sweep gas conditions and the tritium species released on annealing were removed with a helium sweep gas which contained no or 1% H_2. The condensable tritium species (HTO) were recovered in a cold trap (195K) and the non-condensable (HT) were recovered after oxidization to a condensable form. As well as the recovered tritium, the tritium remaining in the sample was measured after the recovery experiments. All the tritium measurements were performed with a liquid scintillation

counter.

2.3. Results

2.3.1. Constant heating rate experiments

Figs. 2-1 and 2-2 show typical tritium release behaviors from both lithium silicates which have been observed with a constant heating rate of 5K/min.   The observations are summarized as follows:

(1) Tritium was released mainly as HTO in all the cases, but the HT yield increased with the increasing partial pressure of H_2 in the sweep gas.

(2) In the case of Li_2SiO_3, the effect of neutron fluence was clearly observed and the increasing neutron fluence resulted in the HTO release at the higher temperatures.   A similar effect was also observed on the HT release with the H_2 containing sweep gas.

(3) In the case of Li_4SiO_4, on the other hand, the effect of neutron fluence was not so clearly observed, but it seemed essentially the same for the two materials.

The irradiation defects have thus been observed to affect the tritium release behavior from both lithium silicates with different extents.   For this difference, it may be remembered that the luminescence intensities of Li_2SiO_3 have been observed to be higher than those of Li_4SiO_4 in the in-situ luminscence measurements of irradiation defects [5,6].   The present results are consistent with the previous observations and different microscopic structures of the two materials may be considered for some details.

2.3.2. Isothermal annealing experiments

Isothermal annealing experiments were performed to know the tritium release kinetics of Li_2SiO_3 in which the effect of neutron fluence is clearer.   The samples were annealed at the constant temperatures up to 873K and the tritium species of HTO and HT were separately recovered.   There are two typical regimes for analyzing the tritium release kinetics.   One is the diffusion-contorolled kinetics as given by [9]

$$y_1 = y_1^{\infty}\left[1 - 6\pi^{-2}\sum_{n=1}^{\infty}n^{-2}\exp\left(-Dn^2\pi^2ta^{-2}\right)\right] \tag{2-1}$$

where y_1 and y_1^{∞} are the fractional yield of the diffusion-controlled tritium release up to time t and the total yield, respectively, D the diffusion coefficient of tritium, and a the sample radius.   The other is the first-order reaction kinetics and is given by

$$y_2 = y_2^{\infty}\left[1 - \exp\left(-kt\right)\right] \tag{2-2}$$

where y_2 and y_2^{∞} are the fractional yield of the first-order reaction controlled tritium release up to time t and the total yield, respectively, and k the reaction rate constant.   These two regimes have been applied to the present data and it has been found that the present data are interpreted by neither of the two regimes but by a combined regime as

$$y = y_1 + y_2 \qquad\qquad\qquad\qquad (2\text{-}3)$$

where y is the yield of the tritium release up to time t.

2.3.3. Observed chemistry of released tritium

Fig. 2-3 shows the neutron fluence dependence of the total yield y^∞ for HT. The experimental data are rather scattered possibly due to different irradiation conditions, but similarly to the constant heating rate experiments, it can be seen that the yield of HT is much higher in the presence of H_2. Furthermore an effect of neutron fluence on the yield of HT may be recognized. The higher the neutron fluence, the higher the yield of HT is. A similar effect has been observed in Li_2O irradiated with 14 MeV neutrons [10]. By comparing both results, it can be said that the HT enhancement is effected by irradiation defects.

In Fig. 2-4, the total yield y_2^∞ of the first-order reaction controlled HTO release are plotted as a function of neutron fluence. In spite of some scatters among the data, the yield may be recognized to decrease with the increasing neutron fluence. This means that the total yield y_1^∞ of the diffusion-controlled HTO release increases with the increasing neutron fluence. From these results, the irradiation defects are considered to affect tritium chemistry inside of the grains.

2.3.4. Diffusion coefficient and reaction rate constant

Fig.2-5 shows the Arrhenius plots of the diffusion coefficient obtained for HTO. In this figure, the effect of neutron fluence is clearly observed and the diffusion coefficient becomes lower at the higher fluence. The difference in the diffusion coefficient reaches up to 2 or 3 orders of magnitude. The obtained diffusion coefficients are summarized in Table 1. The activation energy ranges from 73.7 kJ/mol to 167.0 kJ/mol, and it may be noted that the value increases with the increasing neutron fluence. Similar values and trends have been observed for the diffusion coefficient of HT, and no clear difference between both the tritium species has been found. The irradiation defects are then considered to interact with both the species in grains.

Fig. 2-6 shows the Arrhenius plots of the first-order reaction rate constant k for HTO. No temperature dependence is observed in this case. This indicates that the reaction itself may be very rapid irrespective of temperature as often observed in usual radical reactions. Also, no clear effect of neutron fluence is observed and the irradiation defects may not participate in the reaction.

2.3.5. Interactions of tritium with irradiation defects

From the observations, the following characteristics of the tritium release kinetics of lithium silicates may be summarized:

(1) There are at least two components in the grains of which one follows the diffusion controlled kinetics and the other the first-order reaction controlled kinetics. The yield of

the former increases with the increasing neutron fluence and the diffusion coefficient is strongly affected, indicating that the latter is transformed into the former through the interactions with the irradiation defects.   The reaction rate constant is not affected with neutron fluence and the component of the reaction controlled kinetics may not interact with the irradiation defects.

(2) Tritium is released as HTO and HT from the grain surface.   The yield of HTO decreases and that of HT increases in the presence of the H_2 in the sweep gas, indicating the participation of some surface reactions with H_2.   The production of HT is also effected by the irradiation defects.

Considering these characteristics, some details of the interaction of tritium with the irradiation defects are discussed here.

Tritium is produced in lithium ceramic grains by nuclear reactions and is considered to be stabilized in the chemical states of T^+, T^- and T^0 as observed for Li_2O [10,11].

$$^6Li\ (n, \gamma)\ T \rightarrow T^+, T^-, T^0 \tag{2-4}$$

The components of T^+ and T^- are ionic and diffuse more slowly than that of T^0 which is electrically neutral.   These are expected to follow the diffusion controlled kinetics.   On the other hand, the T^0 is free from any ionic interactions and diffuses rapidly to be released at the grain surface in the form of HTO or HT.   The T^0 is thus considered to be of the reaction controlled kinetics.

In the presence of the irradiation defects, tritium interacts with these defects before its release from the grain surface.   In our previous study [5,6], it has been shown that the irradiation defects of the E' center ($\equiv Si\bullet$), the nonbridging oxygen hole center ($\equiv Si\text{-}O\bullet$) and the peroxy radical ($\equiv Si\text{-}O\text{-}O\bullet$) are produced in Li_2SiO_3 and Li_4SiO_4.   Accordingly, the presently observed effects of neutron fluence on the tritium release kinetics may be interpreted by considering the participation of these irradiation defects.   One of such effects is expressed by

$$T^0 + (\equiv Si\bullet) \rightarrow T^- \tag{2-5}$$
$$T^0 + (\equiv Si\text{-}O\bullet, \equiv Si\text{-}O\text{-}O\bullet) \rightarrow T^+ \tag{2-6}$$

The T^0 interacts with the reducing defects ($\equiv Si\bullet$) and the oxidizing defects ($\equiv Si\text{-}O\bullet$ and $\equiv Si\text{-}O\text{-}O\bullet$) to form T^- and T^+, respectively, and its yield, that is the yield of the component of the reaction controlled kinetics, is then decreased.   Similar reactions of T^+ and T^- are expected to occur and the diffusion coefficient of these species may be affected.

At the grain surface, T^+, T^- and T^0 react with surface species such as $(\equiv Si\text{-}OH)_s$.   For example, the following reactions may be expected.

$$T^+ + (\equiv Si\text{-}OH)_s \rightarrow (\equiv Si+)_s + HTO \uparrow \tag{2-7}$$
$$T^- + (\equiv Si\text{-}OH)_s \rightarrow (\equiv Si\text{-}O\text{-})_s + HT \uparrow \tag{2-8}$$

9

$$T^0 + (\equiv\text{Si-OH})_s \rightarrow (\equiv\text{Si}\bullet)_s + \text{HTO} \uparrow \qquad\qquad (2\text{-}9)$$
$$\rightarrow (\equiv\text{Si-O}\bullet)_s + \text{HT} \uparrow \qquad\qquad (2\text{-}10)$$

The irradiation defects thus affect the chemical state distribution of tritium in the T^+, T^- and T^0 and that of the released tritium in the HTO and HT.   In the presence of H_2, the irradiation defects also react with H_2 as

$$(\equiv\text{Si-O-O}\bullet)_s + H_2 \rightarrow (\equiv\text{Si-O}\bullet)_s + H_2O \uparrow \qquad\qquad (2\text{-}11)$$
$$(\equiv\text{Si-O}\bullet)_s + H_2 \rightarrow (\equiv\text{Si}\bullet)_s + H_2O \uparrow \qquad\qquad (2\text{-}12)$$

So the number of the reducing defects $(\equiv\text{Si}\cdot)s$ increases at the grain surface and the production of HT increases through the following reactions.

$$(\equiv\text{Si}\bullet)_s + H_2 \rightarrow 2\,(\equiv\text{Si-H})_s \qquad\qquad (2\text{-}13)$$
$$T^+ + (\equiv\text{Si-H})_s \rightarrow (\equiv\text{Si}^+)_s + \text{HT} \uparrow \qquad\qquad (2\text{-}14)$$

The enhanced HT production with the irradiation defects is well explained by the present reaction scheme.

2.4. Conclusions

Two types of temperature controlled annealing experiments were performed with lithium silicates and the following conclusions were drawn.

(1) Tritium was released mainly as HTO in all the cases, and the HT yield increased with the increasing partial pressure of H_2 in the sweep gas.   Some dependence of the HT yield on neutron fluence was observed.

(2) The tritium release kinetics of HTO and HT were well interpreted by taking a combined regime of diffusion and first-order reaction.   The dependence of the diffusion kinetics on neutron fluence was observed but any clear dependence of the reaction kinetics was not found.

(3) The observed characteristics of the tritium release kinetics were well interpreted by a reaction scheme, in which the irradiation defects of $\equiv$Si•, $\equiv$Si-O• and $\equiv$Si-O-O• play an important role.

(4) In the studied range, the effects of neutron fluence were observed more clearly for Li_2SiO_3 than for Li_4SiO_4, although those seemed essentially the same for the two materials.

References
1. N. Roux, C. Johnson and K. Noda, Properties and performance of tritium breeding ceramics, J. Nucl. Mater. 191-194 (1992) 15-22.
2. Y. Asaoka, H. Moriyama, K. Iwasaki, K. Moritani and Y. Ito, In-situ luminescence measurement of irradiation defects in lithium oxide, J. Nucl. Mater. 183 (1991) 174-179.
3. Y. Asaoka, H. Moriyama and Y. Ito, Production behavior and its modeling of irradiation

defects in lithium oxide under ion beam irradiation, Fusion Technol. 21 (1992) 1944-1948.

4. Y. Asaoka, H. Moriyama, K. Iwasaki, K. Moritani and Y. Ito, In-situ luminescence measurement of lithium aluminate under ion beam irradiation, J. Nucl. Mater. 191-194 (1992) 268-271.

5. H. Moriyama, T. Nagae, K. Moritani and Y. Ito, A comparison of production behaviour of irradiation defects in lithium ceramics, in: Fusion Technol. 1992, eds. C. Ferro, M. Gasparotto and H. Knoepfel (North-Holland, Amsterdam, 1993) pp. 1434-1438.

6. H. Moriyama, T. Nagae, K. Moritani and Y. Ito, In-situ luminescence measurement of irradiation defects in lithium silicates, Nucl. Instr. Methods in Physics Res., B91 (1994) 317-321.

7. H. Moriyama and T. Kurasawa, Tritium release kinetics of solid lithium ceramics with irradiation defects, J. Nucl. Mater. 212-215 (1994) 932-936.

8. D. Vollath and H. Wedemeyer, Alminum doped lithium orthosilicate as a breeder material, in: Advances in Ceramics, eds. I. Hastings and G. Hollenberg (American Chemical Society, Columbus, 1990) pp.3-12.

9. J. Crank, The mathematics of diffusion, (Oxford University Press, Oxford, 1975), p.89.

10. H. Moriyama, J. Oishi, T. Teral and K. Kawamura, The effect of 14MeV neutron irradiation on tritium recovery from lithium oxide, Fusion Engng. Design 8 (1989) 311-315.

11. K. Okuno and H. Kudo, Chemical states of tritium and interaction with radiation damages in Li_2O crystals, J. Nucl. Mater. 133&134 (1985) 205-208.

Table 2-1. Diffusion coefficient of tritium obtained for HTO in Li_2SiO_3.

Neutron fluence [cm^{-2}]	Sweep gas	D = D$_0$ exp (-ΔE/RT)	
		D$_0$ [m^2/s]	ΔE[kJ/mol]
8.0x10^{15}	He	4.51x10^{-7}	105.8
	He+1%H$_2$	1.22x10^{-9}	73.7
3.0x10^{16}	He	4.71x10^{-7}	108.7
	He+1%H$_2$	-	-
4.8x10^{16}	He	2.64x10^{-6}	148.1
	He+1%H$_2$	-	-
1.0x10^{17}	He	3.52x10^{-8}	124.5
	He+1%H$_2$	-	-
1.3x10^{17}	He	2.27x10^{-5}	167.0
	He+1%H$_2$	6.77x10^{-9}	120.1
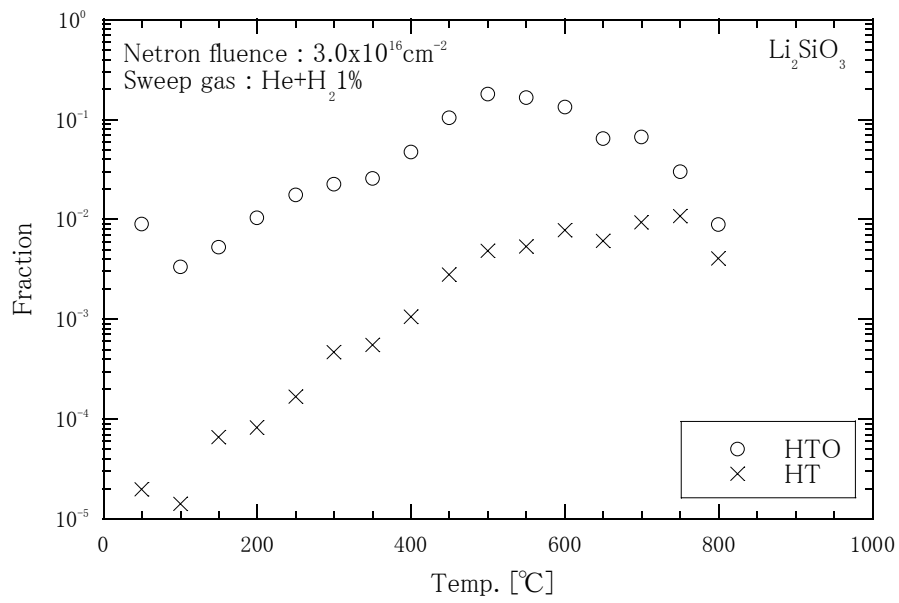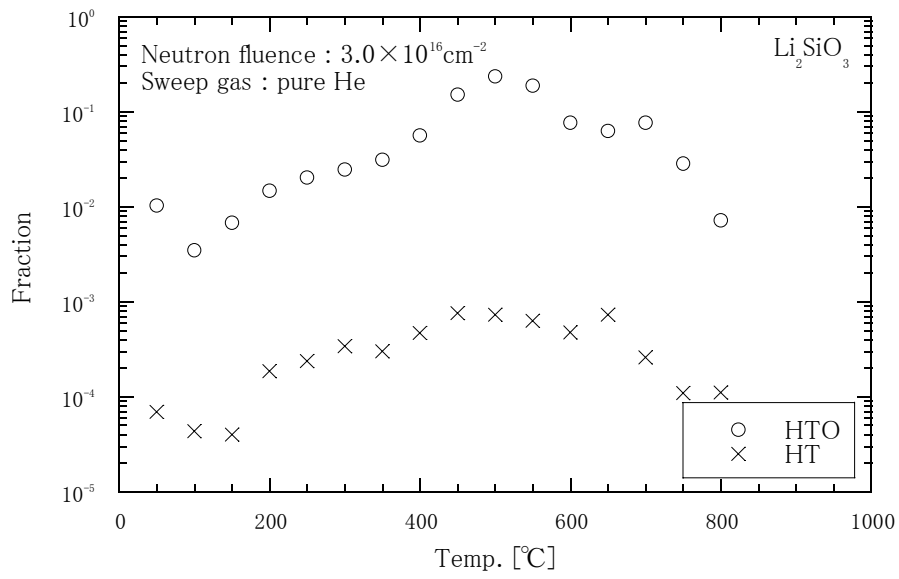
Fig. 2-1. Typical tritium release behaviors from Li_2SiO_3 observed in annealing experiments with a constant heating rate of 5K/min.
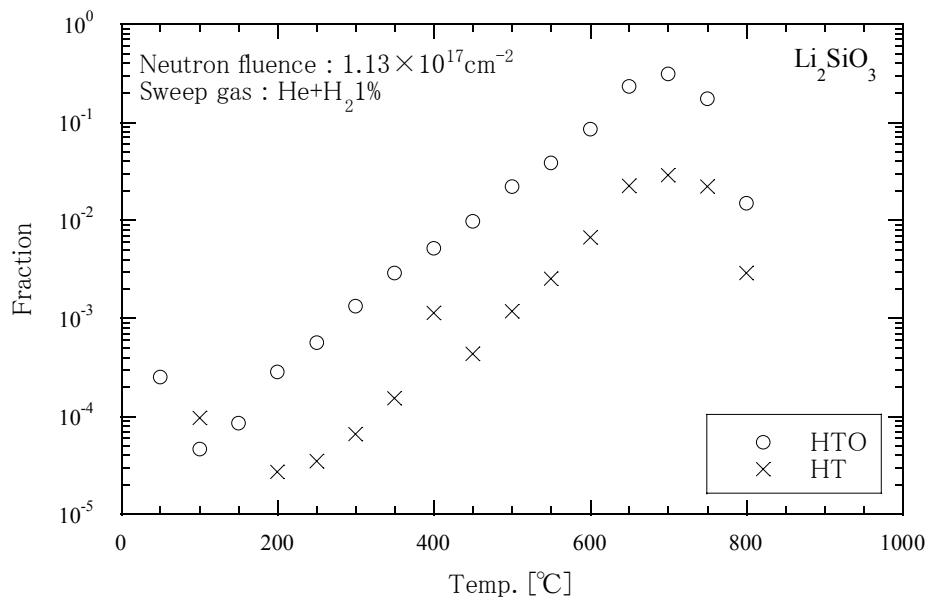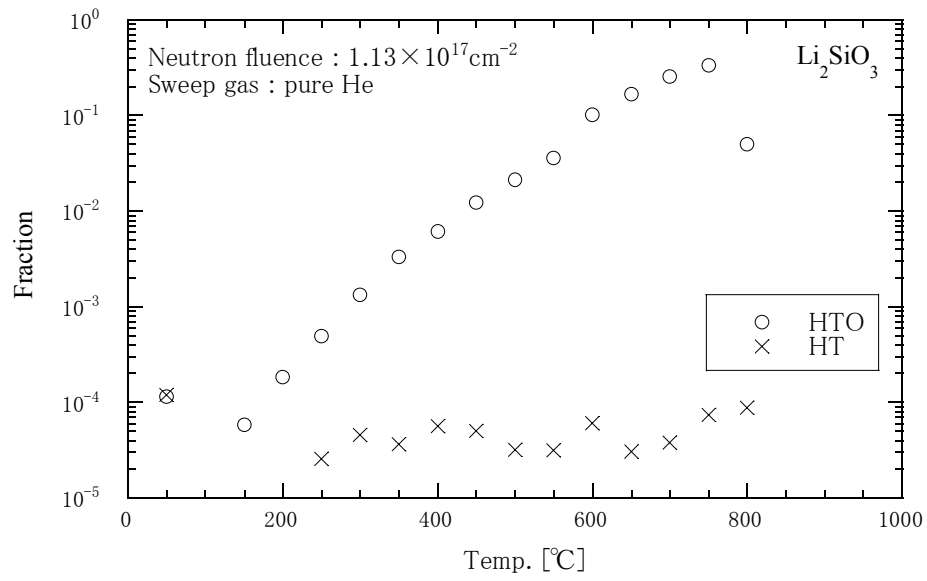
Fig. 2-1 (cont'd). Typical tritium release behaviors from Li_2SiO_3 observed in annealing experiments with a constant heating rate of 5K/min.
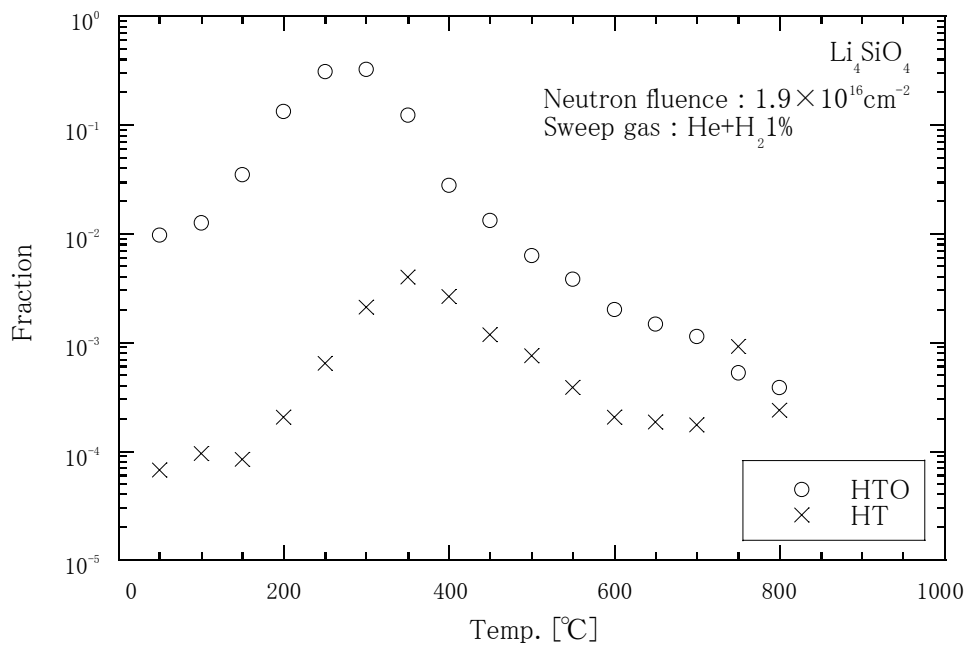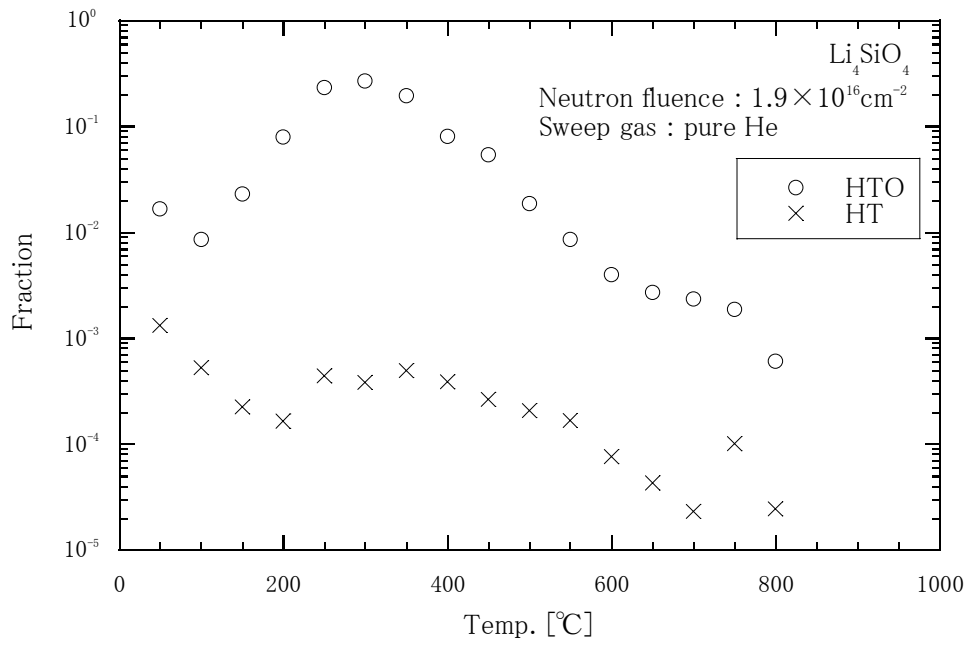
Fig. 2-2. Typical tritium release behaviors from Li$_4$SiO$_4$ observed in annealing experiments with a constant heating rate of 5K/min.
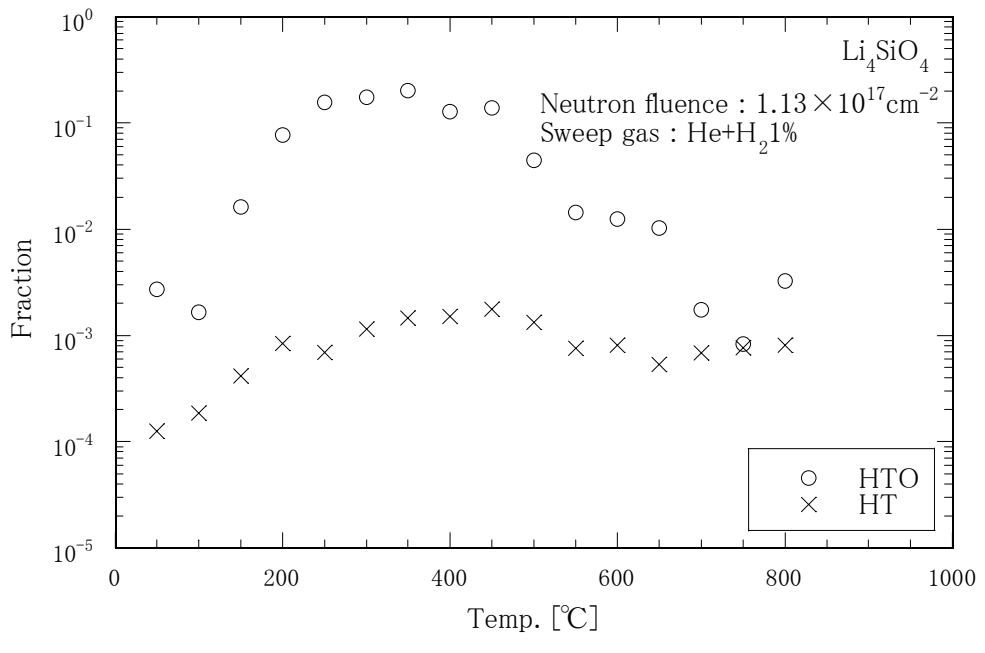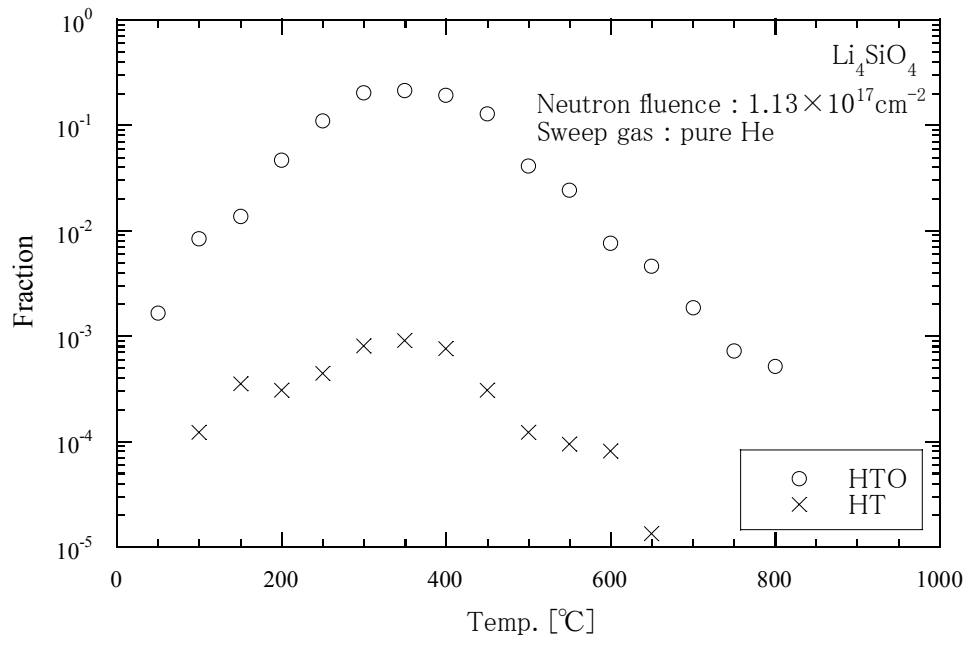
Fig. 2-2 (cont'd). Typical tritium release behaviors from Li_4SiO_4 observed in annealing experiments with a constant heating rate of 5K/min.

16
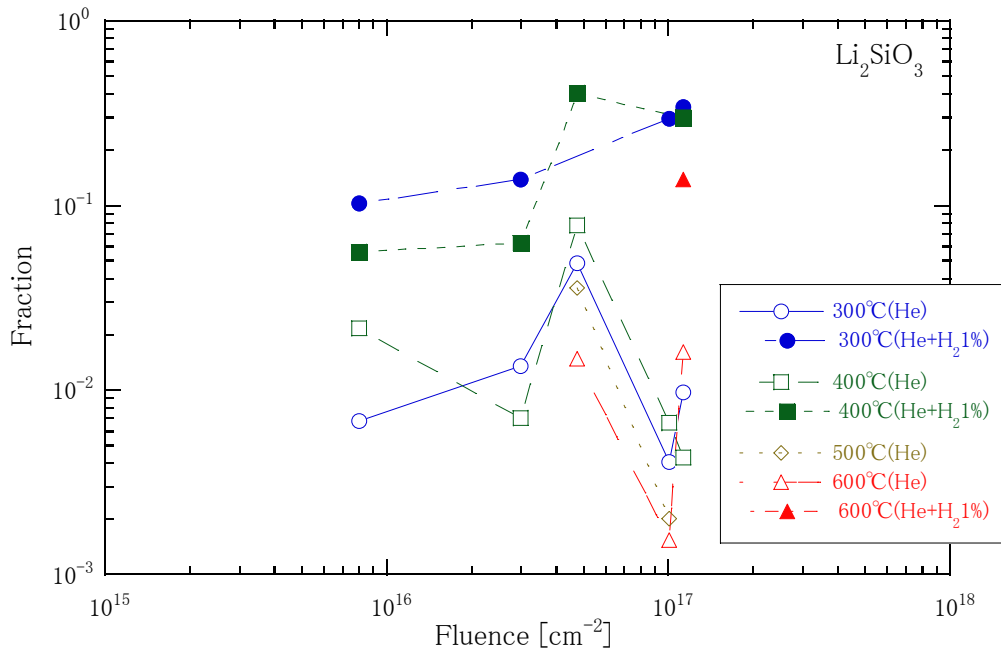
Fig. 2-3. Neutron fluence dependence of the total yield y^{∞} of HT released in isothermal annealing experiments of Li_2SiO_3.
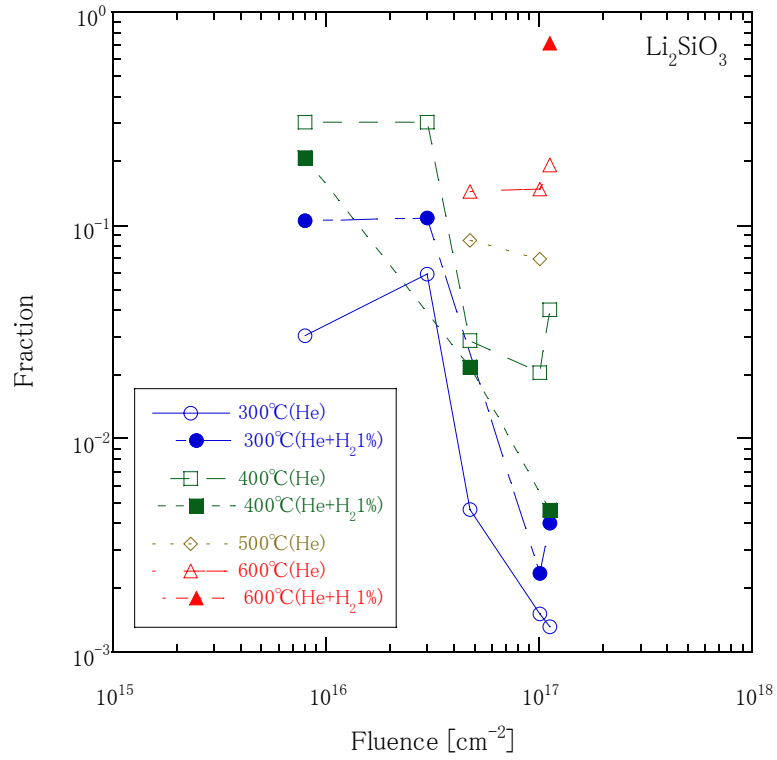
Fig. 2-4. Neutron fluence dependence of the total yield y_2^∞ of HTO released with the reaction controlled kinetics in isothermal annealing experiments of Li_2SiO_3.
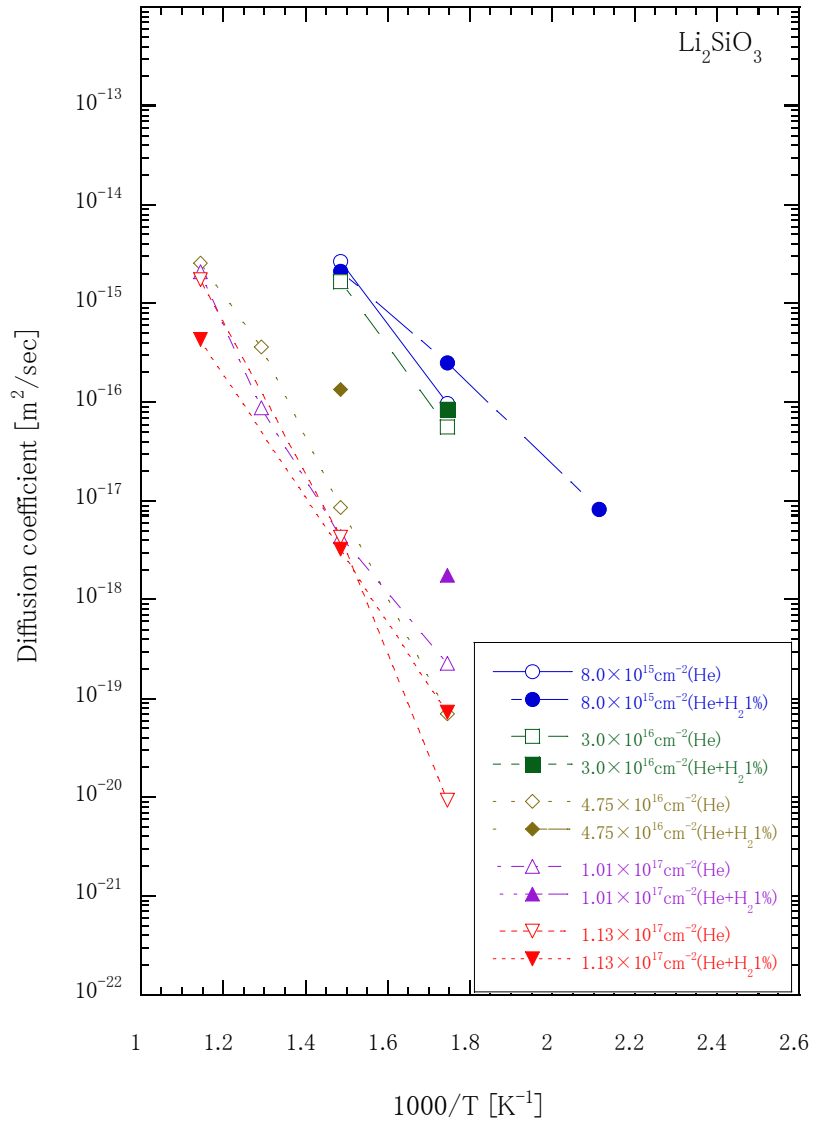
Fig. 2-5. Arrhenius plots of the diffusion coefficient obtained for HTO in isothermal annealing experiments of Li_2SiO_3.
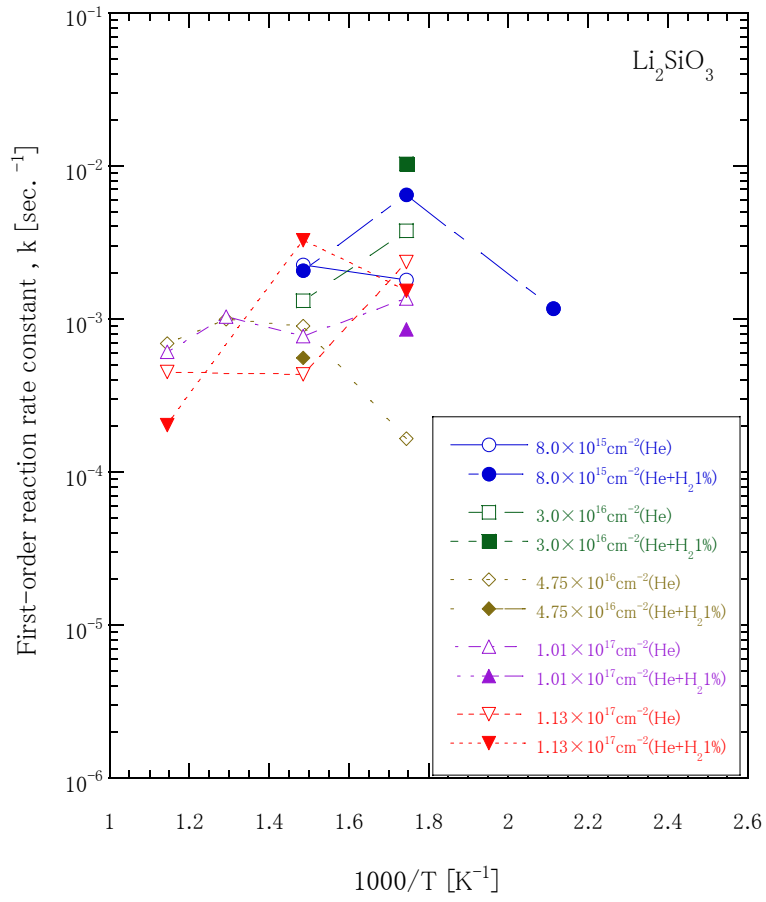
Fig. 2-6. Arrhenius plots of the first-order reaction rate constant k obtained for HTO in isothermal annealing experiments of Li_2SiO_3.

Chapter 3
Production behavior of irradiation defects in lithium silicates and silica under ion beam irradiation

3.1 Introduction

For the performance assessment of fusion reactor blanket systems, the effects of irradiation on the tritium release behaviors and microstructural changes of lithium ceramics are particularly important.   In spite of its importance, however, little is yet known about the mechanism of these effects [1,2].

For a clearer understanding, we have studied the production behavior of irradiation defects in some candidate lithium ceramics by an in-situ luminescence measurement technique under ion beam irradiation.   In Li_2O, it has been confirmed that the F^+ center (an oxygen vacancy trapping an electron) and the F^0 center (an oxygen vacancy trapping two electrons), which are commonly observed in ionic compounds, are formed by irradiation [3,4]. Similarly, the irradiation defects of oxygen vacancies are produced in Li_2SiO_3 and Li_4SiO_4 [5,6].   These defects are considered to play an important role in the tritium behavior [2].

In our recent studies [7,8], the production behavior of irradiation defects in the ternary lithium ceramics of Li_2TiO_3, Li_2ZrO_3 and Li_2SnO_3 was studied, and the production mechanism of irradiation defects in these materials was found to be rather similar to that in Li_2O.   For comparison, the present study deals with kinetic aspects of the production behavior of irradiation defects in Li_2SiO_3, Li_4SiO_4 and SiO_2.   The transient behavior of luminescence intensities for temperature changes was measured and the results were analyzed to determine the values of kinetic parameters of the involved reactions.

3.2 Experimental

The lithium ceramics of Li_2SiO_3 and Li_4SiO_4 were prepared by solid-state reactions. Powders of SiO_2 of reagent grade from Nacalai Tesque, Inc. were milled with Li_2CO_3 in stoichiometric amounts and calcined at 1223K for 8 hours.   The formation of each compound was confirmed by X-ray diffraction.   The contents of Li_2SiO_3 in Li_4SiO_4 and of Li_4SiO_4 in Li_2SiO_3 were found to be negligible (<1%) by diffraction peak analysis. Pellet-type samples of 10 mm in diameter and about 1 mm in thickness were sintered at 1423K for 8 hours.   Specimens of vitreous silica (T-1030, T-2030, T4040) of the same size were obtained from Toshiba Ceramics Co.

A 2 MeV H^+ or He^+ ion beam, accelerated with a Van de Graaff accelerator, was led the target sample at 90°.   The size of the ion beam was about 3 mm in diameter and its current was monitored.   The luminescence from the target sample was led to monochromaters, Ritsu MC-20N, and counted with photo-mutipliers, Hamamatsu R585.   The temperature of the sample holder was controlled with an electric heater and a thermocouple while another thermocouple was attached to the sample surface to monitor its temperature. The OH contents of each specimen (T-1030, T-2030, T4040) and the irradiation conditions are summarized in Table 3-1.

3.3 Results of lithium silicates

3.3.1 Luminescence bands

Fig. 3-1 shows typical luminescence spectra of Li_2SiO_3, Li_4SiO_4 and SiO_2 under He^+ ion beam irradiation. For comparison, the ordinate represents luminescence intensity normalized to the beam current of 1 μA; the peak heights have been observed to be proportional to the beam current and then all of the spectra in the present study are corrected with the beam current. Similar spectra were also observed under H^+ irradiation. As shown in Fig. 3-1, the observed luminescence spectra are decomposed into a number of luminescence bands, namely 330, 380, 420 and 490 nm for Li_2SiO_3, 350, 420, 470 and 520 nm for Li_4SiO_4, and 280, 450 and 490 nm for SiO_2. For the decomposition, following the manner in the previous study [7], energy-based Gaussian functions were taken for all the luminescence bands and the peak heights and positions were determined. For a proper convergence, the peak width has been assumed to be given by an empirical correlation that y = cx^{-2} where y denotes the peak width in eV, x the peak position in eV and c the constant.

Although no clear difference in the luminescence spectra between Li_2SiO_3 and Li_4SiO_4 has been observed in the previous studies [5,6], the spectra of Li_2SiO_3 and Li_4SiO_4 are found to differ from each other in the present study. By considering the higher purity (>99%) of the presently used samples which has been confirmed by X-ray diffraction, however, the present results are believed to be more reliable. The previous results are thus considered to show some contamination of Li_4SiO_4 with a small amount of Li_2SiO_3.

Figs. 3-2 and 3-3 show the Arrhenius plots of the luminescence intensity at fixed bands for Li_2SiO_3 (380 nm) and Li_4SiO_4 (470 nm), respectively. As shown in Fig. 3-2 for Li_2SiO_3, the intensity increases with temperature and reaches the maximum value at around 650K and then decreases above the temperature. In Fig. 3-3, a similar trend is also recognized for Li_4SiO_4 though it is not so significant. Thus the observed temperature dependences are not monotonic, and at least two different sources of the luminescence are considered to be present in these ceramics. A similar situation is also considered to hold for SiO_2 as shown in Fig. 3-4.

3.3.2 Temperature-transient behavior

Fig. 3-5 shows a typical result for the temperature-transient behavior of luminescence intensity in Li_2SiO_3. For a temperature increase, the luminescence intensity first increases, thereafter it decreases and settles down to an equilibrium value. The phenomena are so-called excess luminescence as reported for Li_2O [4] and for other lithium ceramics of Li_2TiO_3, Li_2ZrO_3 and Li_2SnO_3 [8]. In the case of Li_2O [4], the excess luminescence was observed to depend on the irradiation time before the temperature change and to increase with increasing irradiation time. Also, it was found that the excess luminescence intensity saturated at some equilibrium value which was roughly proportional to the second power of the beam current. It was then suggested that the second-order reactions of irradiation defects were involved in the reaction mechanism. In the case of the ternary ceramics such

as Li_2TiO_3, on the other hand, it was found that the excess luminescence was little dependent on the irradiation time except for the very early stage of irradiation and that the equilibrium condition was attained very rapidly for the involved reactions.

The results of Li_2SiO_3 and Li_4SiO_4 in the present study have been found to a little differ from those of Li_2O and of Li_2TiO_3, Li_2ZrO_3 and Li_2SnO_3. In Fig. 3-6, the excess luminescence is plotted as a function of irradiation time before the temperature increase. It can be seen that the excess luminescence decreases with increasing irradiation time when the irradiation temperature is kept high while it is rather constant at lower irradiation temperatures. This indicates that the excess luminescence is associated with the formation of irradiation defects for which some activation energy is needed. At lower temperatures, such a defect could not be formed by irradiation before the temperature increase, and any irradiation history might not be observed. At higher temperatures, on the other hand, the defect will be formed before the temperature increase and because of the effect of saturation, its formation following the temperature change will decrease with increasing irradiation time.

3.3.3 Production mechanism of irradiation defects

It is important to address the observed luminescence bands to respective sources. However, such an information is still lacking for lithium silicates, and extensive studies of SiO_2 are referred for the interpretation of the observed phenomena and for the suggestion of a possible production mechanism of irradiation defects.

In the case of SiO_2, there have been reported two types of irradiation defects [9]. One is the oxygen-deficiency-related defects of the so-called E' centers and some variants of oxygen deficiency centers (ODCs), and the other the oxygen-excess-related defects such as the nonbridging oxygen hole centers and the peroxy radicals. As for the luminescence of irradiation defects, it is known that the luminescence of ODCs is observed at the UV region around 2.7eV (460nm) and 4.4eV (280nm) while that of the others like the nonbridging oxygen hole centers is observed at rather low photon energy region. Thus the presently observed luminescence from SiO_2 which is centered around 440nm can be attributed to ODCs. Also, by considering a structural analogy between SiO_2 and silicates, the formation of similar type irradiation defects may be expected for lithium silicates. According to recent studies of silica, the luminescence intensity is linearly dependent not only on electronic excitation rate [10] but also on displacement rate [11], and it is reasonable to assume that the luminescence comes from the relaxation process of newly formed ODCs trapping electrons.

In our previous study [6], it has been reported that the observed temperature dependent behavior is associated with the formation of the oxygen vacancy centers in the LiO_n polyhedra like ODCs in SiO_2 which is accompanied with the incorporation of the removed oxygen atom into an adjacent SiO_4 tetrahedra to form a peroxy linkage. In general, however, the formation of ODCs is not necessarily accompanied with the formation of peroxy linkages but of oxygen interstitials. Considering these two processes, the following production mechanism of irradiation defects in $Li_{2n}SiO_{n+2}$ (n=0,1,2) can be suggested:

23

$Li_{2n}SiO_{n+2} \rightarrow Li_{2n}SiO_{n+2}*$ (3-1)

$Li_{2n}SiO_{n+2}* \rightarrow ODC + O_i + h\nu$ (3-2)

$Li_{2n}SiO_{n+2}* \rightarrow ODC + (-O-) + h\nu$ (3-3)

Reaction (3-1) represents the production of an excited $Li_{2n}SiO_{n+2}$ ($Li_{2n}SiO_{n+2}*$) by ion beam irradiation, and reactions (3-2) and (3-3) represent the formation of an ODC accompanied with the formation of an oxygen interstitial (O_i) and a peroxy linkage (-O-), respectively. There are two types of ODCs of the relaxed ODC(I) and the non-relaxed ODC(II) for SiO_2 [9], and then some differences may be expected for ODCs in reactions (3-2) and (3-3).   Because of the lack of information available, however, any distinction of ODCs has not been made in the present study.   Such a distinction is not so easy since ODCs are diamagnetic and thus invisible to electron paramagnetic resonance (EPR) techniques.

Reaction (3-3) requires some thermal activation and will take place at high temperatures since the moved oxygen atom is incorporated into a peroxy linkage.   This is the reason why the luminescence of reaction (3-3) is observed at high temperatures.   Reaction (3-3) is also consistent with the observation in which the excess luminescence decreases with increasing irradiation time at higher temperatures since the formation of peroxy linkages is saturated by irradiation before the temperature change.

3.3.4 Determination of kinetic parameters

It is interesting and important to obtain the rate constants of reactions involved in the production of irradiation defects.   Based on the suggested reaction scheme, the observed temperature dependence of the luminescence intensity can be analyzed.

Following the reaction scheme, the observed luminescence intensity I is expressed as:

$I = I_1 + I_2 = k_1[Li_{2n}SiO_{n+2}*] + k_2[Li_{2n}SiO_{n+2}*]$ (3-4)

where I_1 and I_2 are the luminescence intensities and k_1 and k_2 the rate constants of reactions (3-2) and (3-3), respectively.   The life-time of $Li_{2n}SiO_{n+2}*$ is assumed to be very short and a steady-state approximation is applied to $Li_{2n}SiO_{n+2}*$, that is:

$$d[Li_{2n}SiO_{n+2}*]/dt = g' - k_1[Li_{2n}SiO_{n+2}*] - k_2[Li_{2n}SiO_{n+2}*] - \sum_{i \geqq 3} k_i[Li_{2n}SiO_{n+2}*] = 0 \quad (3\text{-}5)$$

where g' is the apparent generation rate of $Li_{2n}SiO_{n+2}*$ by reaction (3-1) and k_i ($i \geqq 3$) the rate constants of the reverse reaction of reaction (3-1) and of some other non-radiative transition of $Li_{2n}SiO_{n+2}*$.   In order to calculate the luminescence intensity, the steady-state concentration of $Li_{2n}SiO_{n+2}*$ is obtained from equation (3-5) and substituted into equation (3-4).

In the present analysis, the obtained data for the temperature dependence of the luminescence intensity are fitted to equations (3-4) and (3-5) by least-squares method.   The rate constants are assumed to be of the Arrhenius type and hence the pre-exponential term A_i

and activation energy term E_i are determined.   For a proper convergence, the number of free parameters is reduced as much as possible.   The energies needed for the production of $Li_{2n}SiO_{n+2}*$ and for its reactions are essentially the same in each lithium ceramic.   Thus the generation rate per unit deposited energy and the activation energy terms are assumed to be the same in each lithium ceramic irrespective of the different projectile ions of H^+ or He^+. On the other hand, the pre-exponential terms are treated to be different for different projectile ions since different reaction conditions may be expected due to different linear energy transfers.   As shown in Figs. 3-1 to 3-3, the observed temperature dependence of the luminescence intensity is well fitted to equations (3-4) and (3-5), and the values of kinetic parameters of the involved reactions are obtained as given in Table 3-2.

As can be expected for the first-order reactions, all the ratios of A_2/A_1, A_3/A_1 and A_4/A_1 are not so dependent on the projectile ions.   However, it may be found that the A_2/A_1 value for both ceramics is slightly larger for H^+ ions than for He^+ ions.   This difference will be explained by considering different linear energy transfers of the projectile ions.   As mentioned above, reaction (3-3) for the formation of the ODCs accompanies the incorporation of the moved oxygen into a peroxy linkage, and it will be reduced when the sites for peroxy linkages are saturated.   This is the reason why the different A_2/A_1 values are obtained for different projectile ions.   In the case of H^+ ions of the lower linear energy transfer, the specific ionization and hence the local concentration of $Li_{2n}SiO_{n+2}*$ will be low in the ion tracks and the sites for peroxy linkages are hardly saturated, leading to the higher yield of reaction (3-3).   In the case of He^+ ions, on the other hand, those sites will be more easily saturated and then reaction (3-3) will be reduced.

3.4 Results of vitreous silica
3.4.1 Luminescence bands

Fig. 3-7 shows typical luminescence spectra of T-1030, T-2030 and T-4040 under He^+ ion beam irradiation.   For comparison, the ordinate represents luminescence intensity normalized to the beam current of 1 nA; the peak heights have been observed to be proportional to the beam current and then all of the spectra in the present study are corrected with the beam current.   Similar spectra were also observed for T-4040 under H^+ irradiation. As shown in Fig. 3-7, the observed luminescence spectra are decomposed into a number of luminescence bands, namely 280, 460 and 490 nm for each vitreous silica.   For the decomposition, following the manner in 3.3.1, energy-based Gaussian functions were taken for all the luminescence bands and the peak heights and positions were determined.   For a proper convergence, the peak width has been assumed to be given by an empirical correlation that $y = cx^{-2}$ where y denotes the peak width in eV, x the peak position in eV and c a constant.

In the case of SiO_2, there have been reported two types of irradiation defects [9].   One is the oxygen-deficiency-related defects of the so-called E' centers ($\equiv$Si•) and some variants of oxygen deficiency centers (ODCs, $\equiv$Si:Si$\equiv$), and the other the oxygen-excess-related defects such as the nonbridging oxygen hole centers ($\equiv$Si-O•) and the peroxy radicals ($\equiv$Si-O-O•). As for the luminescence of irradiation defects, it is known that the luminescence of ODCs is

observed at the UV region around 2.7eV (460nm) and 4.4eV (280nm) while that of the others like the nonbridging oxygen hole centers is observed at rather low photon energy region. Thus the presently observed luminescence from SiO_2 which is centered at 280 and 460nm can be attributed to ODCs. As already suggested in 3.3.3, the luminescence intensity is linearly dependent not only on electronic excitation rate [10] but also on displacement rate [11], and it is reasonable to assume that the luminescence comes from the relaxation process of newly formed ODCs trapping electrons.

As shown in Fig. 3-7, no apparent difference was observed in the luminescence spectra of the specimens of different OH contents. This means that the OH does not play so important role in the present luminescence behavior.
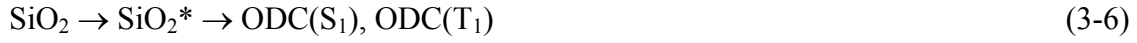
3.4.2 Temperature-transient behavior

Figs. 3-8, 3-9 and 3-10 show the Arrhenius plots of the luminescence intensity at fixed bands for T-1030, T-2030 and T-4040, respectively. As shown in these figures, the intensity decreases rather monotonically with temperature. This is a little different result from that of 3.3, in which some non-monotonic temperature dependence has been observed for the luminescence at 460nm from T-1030. According to the results in 3.3, however, such a non-monotonic temperature dependence is due to the contribution of irradiation defects which are easily saturated, and then this difference is explained by considering different beam currents between two cases. In fact, the beam current of 20-50 nA in the present case is much higher than that of 3 nA in 3.3. The irradiation defects might be so saturated that their contribution could not been observed in the present case. The present result of the temperature dependence is thus consistent with that in 3.3.

For confirmation, the result of 3.3 was re-examined here in some details. In that case, the luminescence intensity was measured by increasing temperature up to 830K and then by decreasing temperature to ambient one, and an interesting temperature dependence of the luminescence intensity was found in the temperature region above 450K as shown in Fig. 3-11. It can be seen that the luminescence intensity with decreasing temperature is a little higher than that with increasing temperature in this region. This hysteresis effect can be explained by considering the irradiation history. According to the results in 3.3, a considerable part of the luminescence in this region is attributed to the formation of ODCs accompanied with peroxy linkages, which are likely to be saturated by irradiation. Thus it can be considered that the luminescence intensity with increasing temperature is reduced by the effect of saturation while the luminescence with decreasing temperature is increased by the recovery of peroxy linkages at the higher temperature.

3.4.3 Production mechanism of irradiation defects

As is known [9], the luminescence at 2.7 eV (460nm) and 4.4 eV (280nm) is attributed to the triplet (T_1 to S_0) and the singlet (S_1 to S_0) emissions of ODCs. It is also known that the singlet-triplet conversion (S_1 to T_2) occurs with the activation energy of 0.13 eV [9], and that the luminescence at 460nm is due to the formation of ODCs accompanied with the formation

of peroxy linkages (-O-) and/or oxygen interstitials (O_i), as suggested in 3.3.　By considering these known facts, the following production mechanism of irradiation defects in SiO_2 can be suggested:

$$SiO_2 \rightarrow SiO_2^* \rightarrow ODC(S_1), ODC(T_1) \tag{3-6}$$
$$ODC(S_1) \rightarrow ODC(S_0) + h\nu_{280} \tag{3-7}$$
$$ODC(S_1) \rightarrow ODC(T_2) \rightarrow ODC(T_1) \tag{3-8}$$
$$ODC(T_1) \rightarrow ODC(S_0) + O_i + h\nu_{460} \tag{3-9}$$
$$ODC(T_1) \rightarrow ODC(S_0) + (-O-) + h\nu_{460} \tag{3-10}$$
$$ODC(T_1) \rightarrow recombination\ with\ O_i \tag{3-11}$$
$$ODC(T_1) \rightarrow recombination\ with\ (-O-) \tag{3-12}$$

As shown in Fig. 3-12, reaction (3-6) represents the production of an excited SiO_2 (SiO_2^*) by ion beam irradiation, which is de-excited to $ODC(S_1)$ and $ODC(T_1)$.　Reaction (3-7) represents the de-excitation of the $ODC(S_1)$ accompanied with the luminescence at 280nm, and reaction (3-8) the singlet-triplet conversion [9].　Because of rather monotonic temperature dependence of the 280nm luminescence, no other reaction is considered for the $ODC(S_1)$.　As suggested in 3.3, on the other hand, a number of competitive reactions are considered for the 460nm luminescence, namely reactions (3-9) to (3-12).　Reactions (3-9) and (3-10) represent the de-excitation of the $ODC(T_1)$ accompanied with the formation of an oxygen interstitial (O_i) and a peroxy linkage (-O-),　respectively, and reactions (3-11) and (3-12) the recombination with the oxygen interstitial and peroxy linkage, respectively.

Reaction (3-10) requires some thermal activation and will take place at high temperatures since the moved oxygen atom is incorporated into a peroxy linkage.　This is the reason why the luminescence at 460nm has been observed at high temperatures in 3.3. In the present case, however, the contribution of these reactions is considered to be much smaller as mentioned above.

3.4.4 Determination of kinetic parameters

It is interesting and important to obtain the rate constants of reactions involved in the production of irradiation defects.　Based on the suggested reaction scheme, the observed temperature dependence of the luminescence intensity is analyzed here.

Following the reaction scheme, the observed luminescence intensities I_{280} and I_{460} at 280nm and 460nm are expressed as:

$$I_{280} = k_7[ODC(S_1)] \tag{3-13}$$
$$I_{460} = k_9[ODC(T_1)] + k_{10}[ODC(T_1)] \tag{3-14}$$

where k_i is the rate constant of reaction (i).　The lifetimes of $ODC(S_1)$ and $ODC(T_1)$ are assumed to be very short and a steady-state approximation is applied to these ODCs, that is:

27

$$d[ODC(S_1)]/dt = g_{S1}' - k_7[ODC(S_1)] - k_8[ODC(S_1)] = 0 \qquad (3\text{-}15)$$

$$d[ODC(T_1)]/dt = g_{T1}' + k_8[ODC(S_1)]$$
$$- k_9[ODC(T_1)] - k_{10}[ODC(T_1)] - k_{11}[ODC(T_1)] - k_{12}[ODC(T_1)] = 0$$
$$(3\text{-}16)$$

where g_{S1}' and g_{T1}' are the apparent generation rate of $ODC(S_1)$ and $ODC(T_1)$ by reaction (3-6).   For simplicity, reactions (3-11) and (3-12) are assumed to be the first-order reactions in the present study.   In order to calculate the luminescence intensities, the steady-state concentrations of $ODC(S_1)$ and $ODC(T_1)$ are obtained   from equations (3-15) and (3-16), respectively, and substituted into equations (3-13) and (3-14), respectively.

In the present analysis, the obtained data for the temperature dependence of the luminescence intensity are fitted to equations (3-13) and (3-14) by least-squares method. The rate constants are assumed to be of the Arrhenius type and hence the pre-exponential term A_i and activation energy term E_i are determined.   For a proper convergence, however, the number of free parameters is reduced as much as possible.   Fortunately, the activation energies for reactions (3-10) to (3-12) have been determined in 3.3, and are assumed to be the same for all specimens in the present study by considering the similarities in the temperature dependence of the luminescence as shown in Figs. 3-8 to 3-10.   Then, the pre-exponential terms and the generation rates are treated as fitting parameters in the present study.   As shown in Figs. 2-4, the observed temperature dependence of the luminescence intensity is well fitted to equations (3-13) and (3-14), and the values of kinetic parameters of the involved reactions are obtained as given in Table 3-3.

The activation energy value of reaction (3-8) is obtained to be 16.8 kJ/mol (0.17 eV), 19.5 kJ/mol (0.20 eV), 16.5 kJ/mol (0.17 eV) for T-1030, T-2030, T-4040, respectively. These values are found to be consistent with the reported value of 0.13 eV for the singlet-triplet conversion [12], supporting the present interpretation of observations. Although no other reaction is considered for the 280nm luminescence in the present study, this is also consistent with a very short lifetime (τ = 4.2ns [13,14]) of the $ODC(S_1)$.   In such a case, its recombination reaction is considered to hardly occur since it needs a longer time for the diffusion of oxygen interstitials and peroxy linkages.   In the case of the 460nm luminescence, on the other hand, the lifetime of the $ODC(T_1)$ is much longer (τ = 10.2ms [15,16]) and then its recombination reactions will occur as observed in the present study.

3.4 Conclusions

In order to know the production behavior of irradiation defects in the ternary lithium ceramics of Li_2SiO_3 and Li_4SiO_4, the transient behavior of luminescence intensities for temperature changes was studied as well as the temperature dependence of the luminescence intensity.   The results of Li_2SiO_3 and Li_4SiO_4 were found to a little differ from those of Li_2O and of the other ternary ceramics, and the production mechanism of irradiation defects was suggested   in which ODCs were formed together with oxygen interstitials and peroxy

linkages.

The temperature dependence of the 280nm luminescence was well explained by considering the radiative transition of ODC(S_1) to ODC(S_0) competing only with the singlet-triplet conversion of ODC(S_1). In the case of the 460nm luminescence, on the other hand, its temperature dependence was interpreted by considering a number of competing reactions including its recombination with oxygen interstitials and peroxy linkages. The different temperature dependence is due to different lifetimes of the two states, and the lifetime of the ODC(S_1) seems to be too short to recombine with oxygen interstitials and peroxy linkages.

References

[1] N. Roux, G. Hollenberg, C. Johnson, K. Noda, R. Verrall, Fusion Engng. Design 27 (1995) 154.

[2] H. Moriyama, S. Tanaka and K. Noda, J. Nucl. Mater. 258-263 (1998)587.

[3] Y. Asaoka, H. Moriyama, K. Iwasaki, K. Moritani and Y. Ito, J. Nucl. Mater. 183 (1991) 174.

[4] Y. Asaoka, H. Moriyama and Y. Ito, Fusion Technol. 21 (1992) 1944.

[5] H. Moriyama, T. Nagae, K. Moritani and Y. Ito, Proc. 17th Symp. on Fusion Technology, Rome, 1992, p.1434.

[6] H. Moriyama, T. Nagae, K. Moritani and Y. Ito, Nucl. Instr. Methods in Physics Res. B91 (1994) 317.

[7] K. Moritani and H. Moriyama, J. Nucl. Mater. 248 (1997) 132.

[8] K. Moritani and H. Moriyama, J. Nucl. Mater. 258-263 (1998) 525.

[9] L. Skuja, J. Non-Cryst. Solids. 239 (1998) 16.

[10] M. Fujiwara, T. Tanabe, H. Miyamaru, K. Miyazaki, Nucl. Intsr. and Meth. B116 (1996) 536.

[11] T. Tanabe, A. Omori, M. Fujiwara, J. Nucl. Mater. 258-263 (1998) 1914.

[12] L. Skuja, J. Non-Cryst. Solids 167 (1994) 229.

[13] H. Nishikawa, E. Watanabe, D. Ito, Y. Ohki, Phys. Rev. Lett. 72 (1994) 2101.

[14] R. Boscanio, M. Cannas, F. M. Gelardi, M. Leone, J. Phys.:Condens. Matt. 8 (1996) L545.

[15] L. N. Skuja, A. N. Streletsky, A. B. Pakovich, Solid State Commun. 50 (1984) 1069.

[16] L. Skuja, J. Non-Cryst. Solids 149 (1992) 77.

Table 3-1. Experimental conditions.

Specimen	OH (ppm)	Irradiation condition		
		Projectile	Beam current (nA)	Temperature (K)
T-1030	200	2MeV He$^+$	15 - 50	301 - 759
T-2030	1	2MeV He$^+$	15 - 50	301 - 771
T-4040	800	2MeV H$^+$	20 - 50	298 - 919
		2MeV He$^+$	15 - 60	305 - 851

Table 3-2. Optimum parameter values obtained from the analysis of in-situ luminescence measurement data.

Ceramics	Projectile	k_2/k_1 $=A_2/A_1\exp[-(E_2-E_1)/RT]$		k_3/k_1 $=A_3/A_1\exp[-(E_3-E_1)/RT]$		k_4/k_1 $=A_4/A_1\exp[-(E_4-E_1)/RT]$		$g'(s^{-1})$
		$A_2/A_1(-)$	E_2-E_1(kJ/mol)	$A_3/A_1(-)$	E_3-E_1(kJ/mol)	$A_4/A_1(-)$	E_4-E_1(kJ/mol)	
Li$_2$SiO$_3$	H$^+$	1.2x10^6	35.1	1.8x10^6	29.9	4.9x10^{13}	134.2	6.7x10^5
	He$^+$	7.0x10^5	(35.1)*	4.6x10^6	(29.9)*	1.8x10^{14}	(134.2)*	(6.7x10^5)*
Li$_4$SiO$_4$	H$^+$	2.3x10^5	50.7	4.3x10^5	41.1	2.7x10^{13}	153.0	5.4x10^4
	He$^+$	5.4x10^4	(50.7)*	9.9x10^5	(41.1)*	1.5x10^{13}	(153.0)*	(5.4x10^4)*
SiO$_2$	H$^+$	9.8x10^6	72.0	3.4x10^3	32.4	1.1x10^{10}	104.1	9.6x10^2
	He$^+$	2.6x10^6	(72.0)*	3.2x10^3	(32.4)*	2.1x10^{10}	(104.1)*	(9.6x10^2)*

* Assumed to be the same for both H$^+$ and He$^+$ ion irradiations of each ceramic.

Table 3-3. Optimum parameter values obtained from the analysis of in-situ luminescence measurement data.

Specimen	Projectile	k_8/k_7 $=A_8/A_7\exp[-(E_8-E_7)/RT]$		$g'_{S1}(s^{-1})$
		$A_8/A_7(-)$	E_8-E_7(kJ/mol)	
T1030	He$^+$	8.4×10^1	16.8	5.8×10^1
T2030	He$^+$	3.8×10^2	19.5	1.2×10^2
T4040	H$^+$	3.6×10^2	16.5	5.5×10^2
	He$^+$	7.5×10^1	(16.5)[a]	7.5×10^1

Specimen	Projectile	k_{10}/k_9 $=A_{10}/A_9\exp[-(E_{10}-E_9)/RT]$		k_{11}/k_9 $=A_{11}/A_9\exp[-(E_{11}-E_9)/RT]$		k_{12}/k_9 $=A_{12}/A_9\exp[-(E_{12}-E_9)/RT]$		$g'_{T1}(s^{-1})$
		$A_{10}/A_9(-)$	$E_{10}-E_9$(kJ/mol)	$A_{11}/A_9(-)$	$E_{11}-E_9$(kJ/mol)	$A_{12}/A_9(-)$	$E_{12}-E_9$(kJ/mol)	
T1030[5]	H$^+$	9.8×10^6	72.0	3.4×10^3	32.4	1.1×10^{10}	104.1	9.6×10^2
T1030	He$^+$	3.2×10^5	(72.0)[b]	2.3×10^3	(32.4)[b]	2.4×10^9	(104.1)[b]	5.1×10^2
T2030	He$^+$	5.5×10^4	(72.0)[b]	5.7×10^3	(32.4)[b]	1.6×10^9	(104.1)[b]	1.0×10^3
T4040	H$^+$	4.1×10^4	(72.0)[b]	7.1×10^3	(32.4)[b]	2.0×10^9	(104.1)[b]	3.4×10^3
	He$^+$	-[c]	(72.0)[b]	2.6×10^3	(32.4)[b]	2.7×10^8	(104.1)[b]	6.6×10^2

[a] Assumed to be the same for both H$^+$ and He$^+$ ion irradiations of each specimen.

[b] Taken from Table 3-2 and assumed to be the same for all specimens.
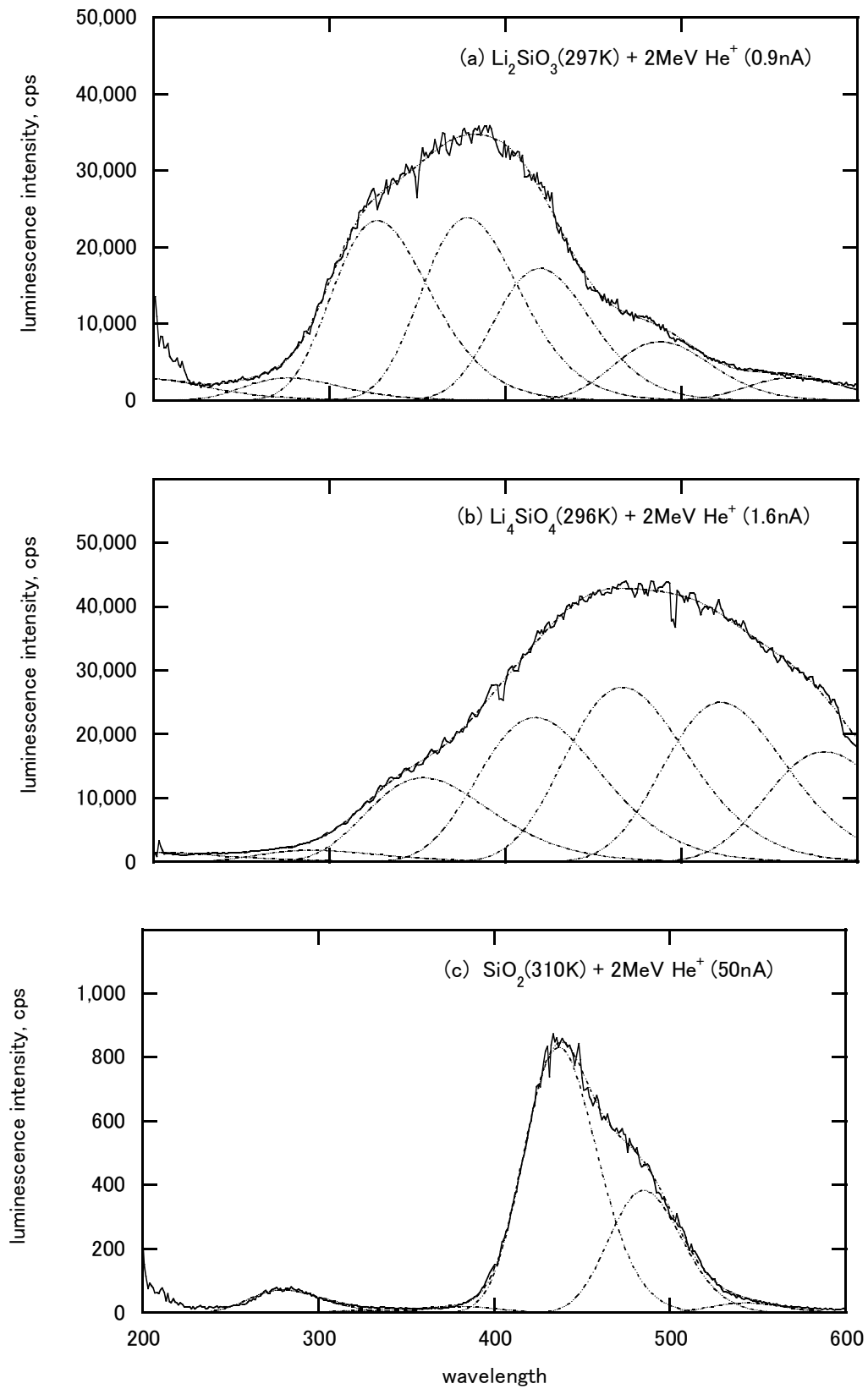
[c] Negligible.

Fig. 3-1. Typical luminescence spectra of Li_2SiO_3, Li_4SiO_4 and SiO_2 under He^+ ion beam irradiation.
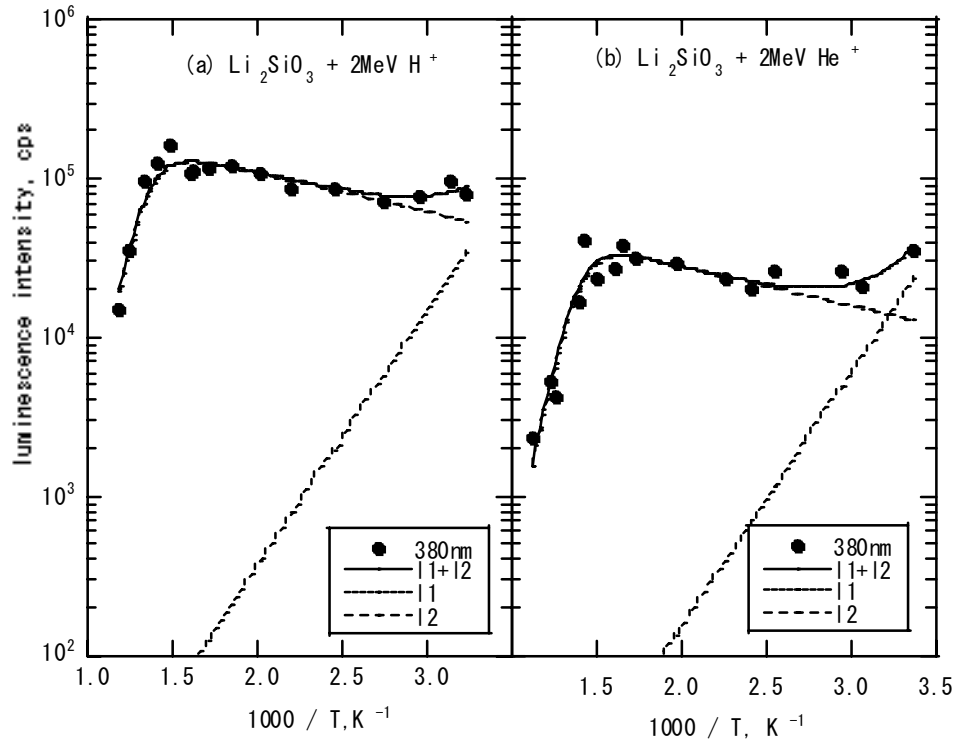
Fig. 3-2. Arrhenius plots of luminscence intensity of Li_2SiO_3 under (a) H^+ and (b) He^+ irradiation. The ordinate represents luminescence intensity corrected for beam current. Marks are experimental and curves represent the least-squares fits of the data by eqs. (3-4) and (3-5).
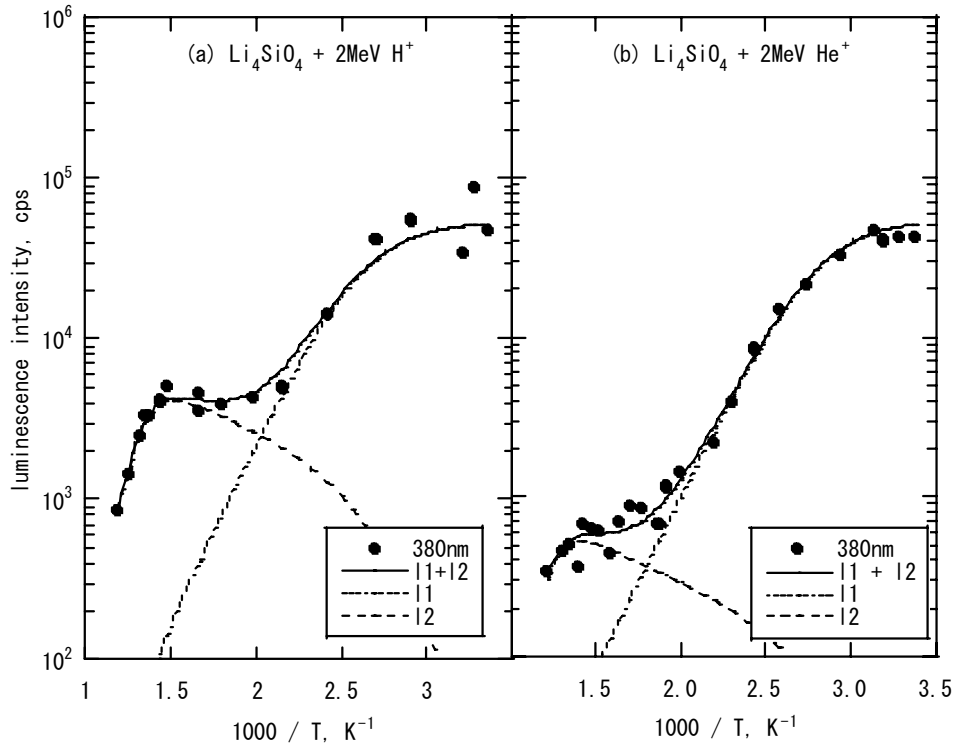
Fig. 3-3. Arrhenius plots of luminscence intensity of Li_4SiO_4 under (a) H^+ and (b) He^+
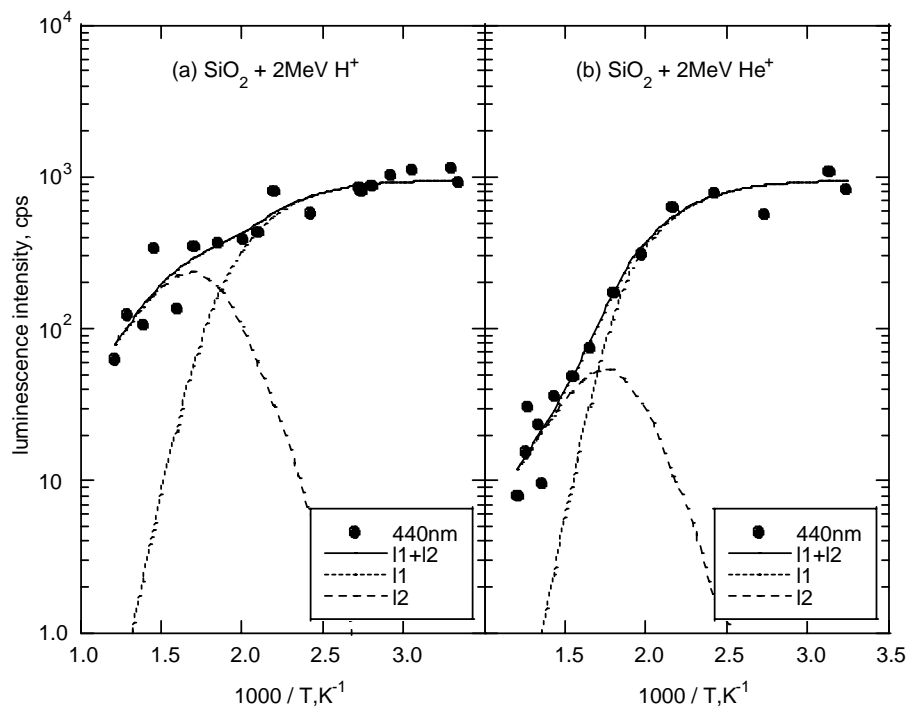irradiation.   See also Fig. 1 captions.

Fig. 3-4. Arrhenius plots of luminscence intensity of SiO_2 under (a) H^+ and (b) He^+ irradiation.   See also Fig. 3-1 captions.
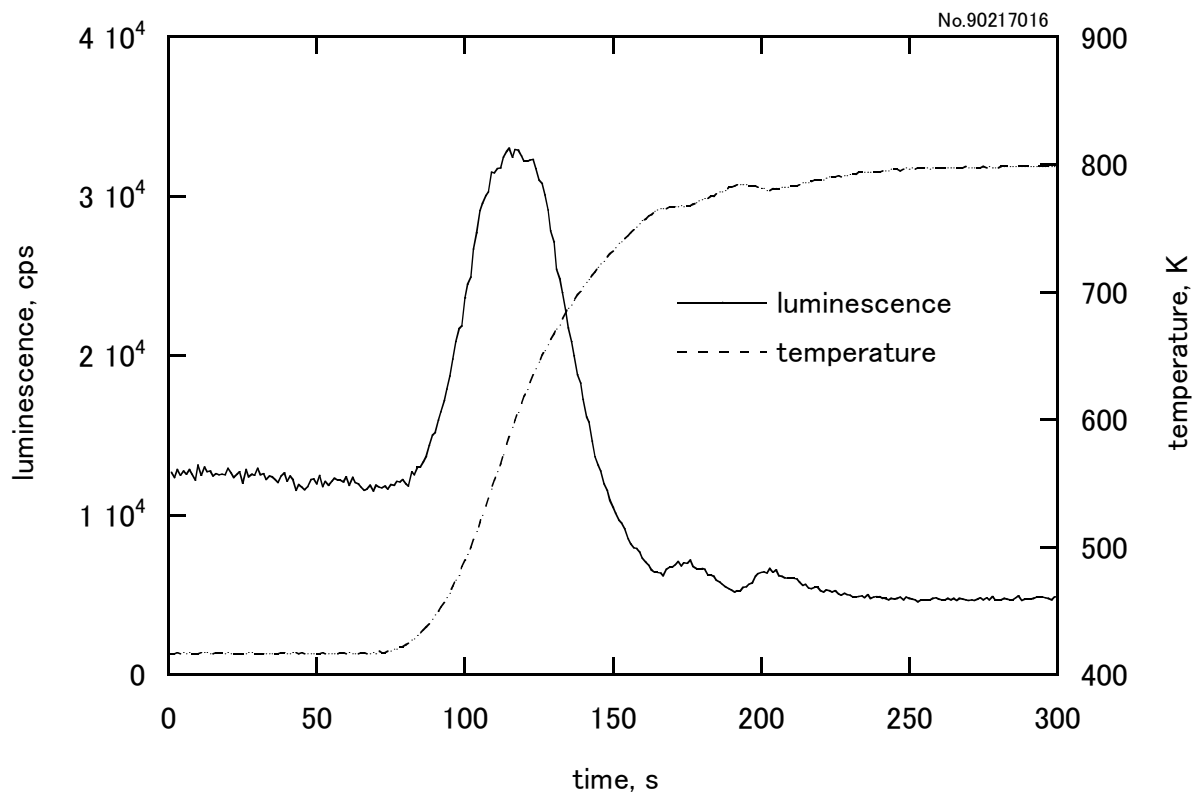
Fig. 3-5.   Temperature-transient behavior of luminescence intensity at 380nm for Li_2SiO_3 irradiated with 2 MeV H^+ ions of 5 nA.   Irradiation time before a temperature increase is 300 sec.
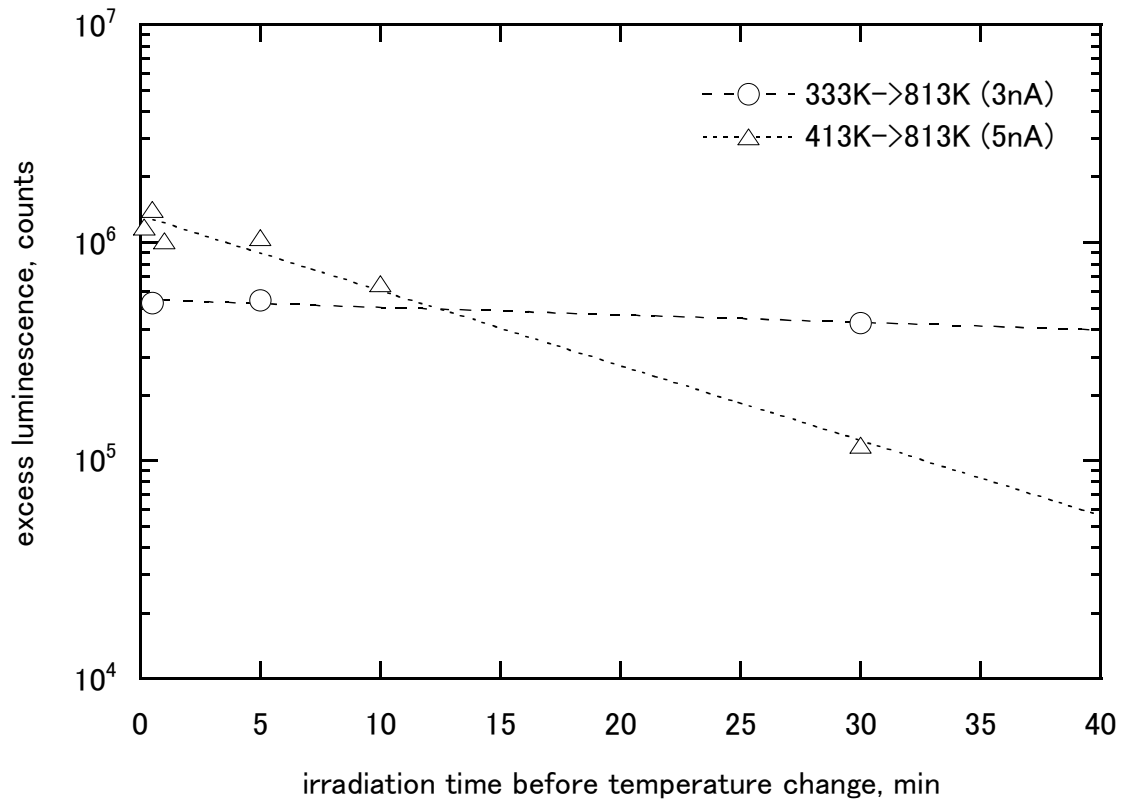
Fig. 3-6.　Dependence of excess luminescence on irradiation time for Li_2SiO_3 irradiated with 2 MeV H^+ ions.
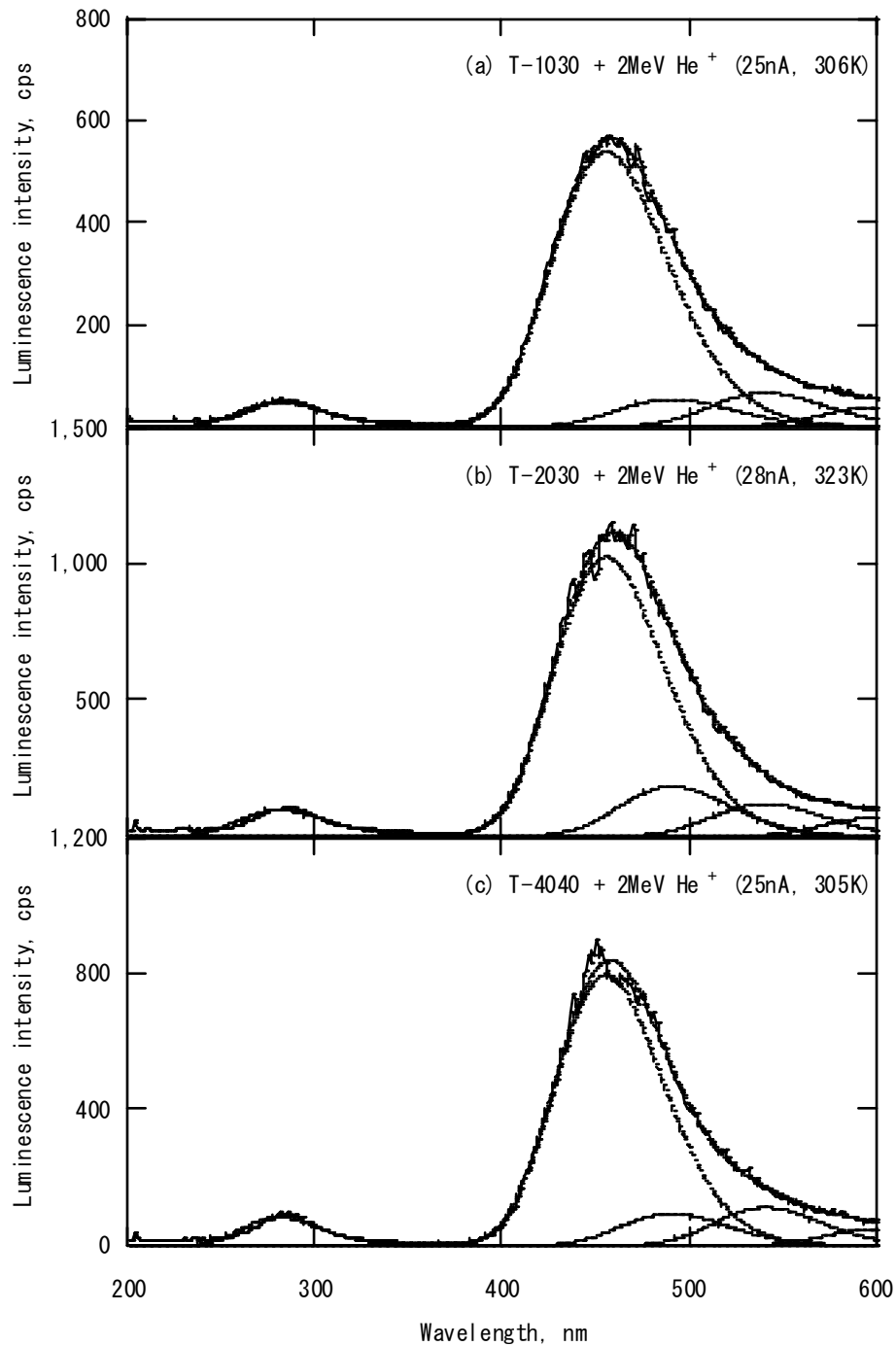
Fig. 3-7. Typical luminescence spectra of T-1030, T-2030 and T-4040 under 2MeV He$^+$ ion beam irradiation. The ordinate represents luminescence intensity normalized to the beam current of 1nA. The dashed curves represent the results of decomposition as described in 3.4.1.
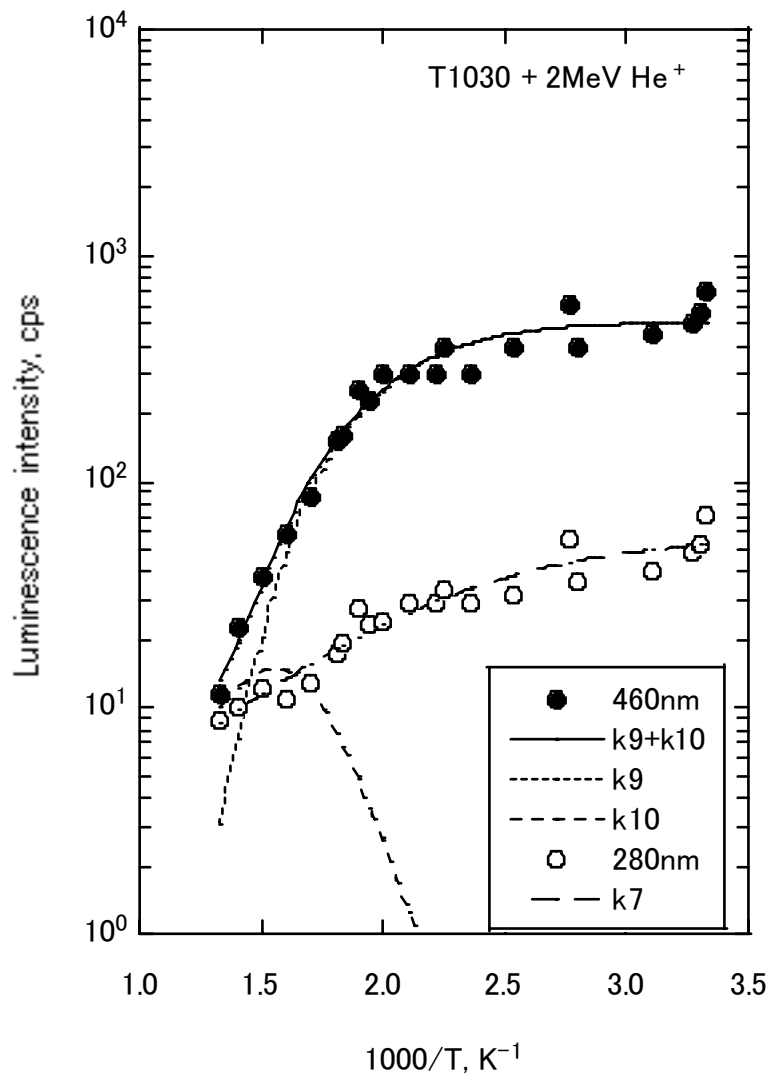
Fig. 3-8. Arrhenius plots of luminescence intensity of T-1030 under 2MeV He$^+$ irradiation. The ordinate represents luminescence intensity normalized to the beam current of 1nA. The marks are experimental and the curves represent the least-squares fits of the data to eqs. (3-13) and (3-14) as described in 3.4.4.
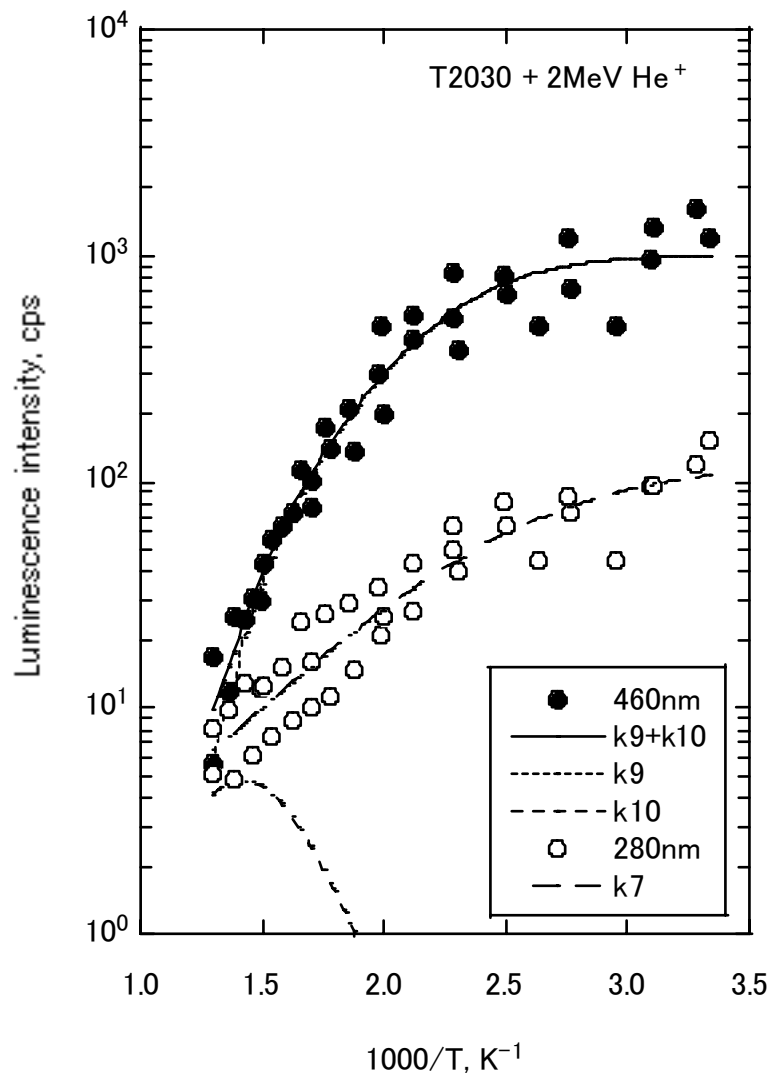
Fig. 3-9.　Arrhenius plots of luminescence intensity of T-2030 under 2MeV He$^+$ irradiation. See also Fig. 3-8 captions.
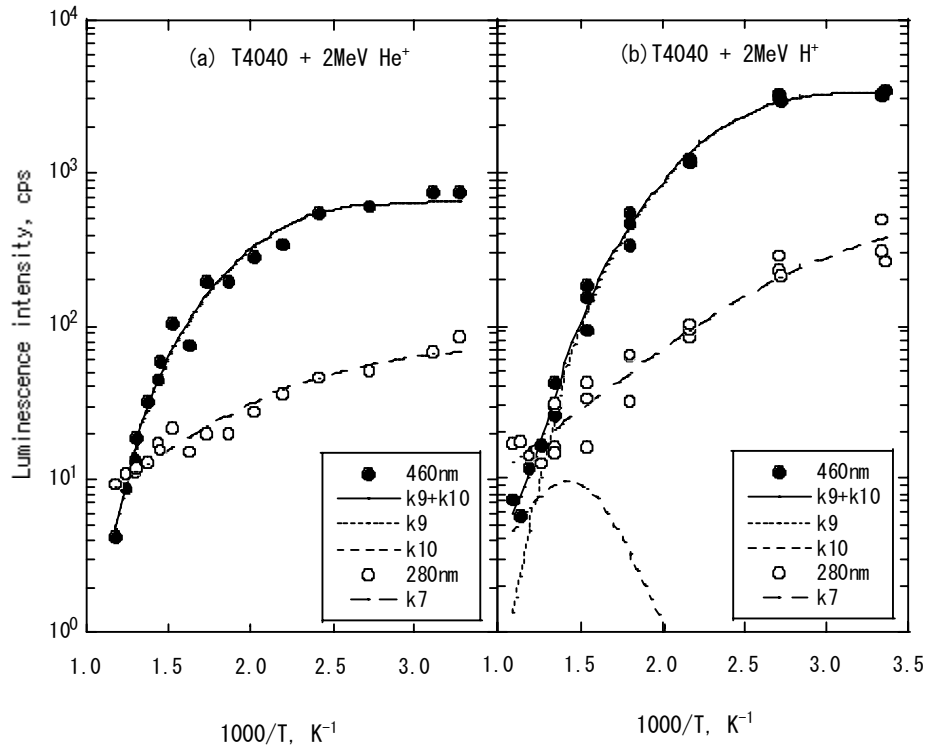
Fig. 3-10. Arrhenius plots of luminescence intensity of T-4040 under (a) H$^+$ and (b) He$^+$ irradiation.   See also Fig. 3-8 captions.
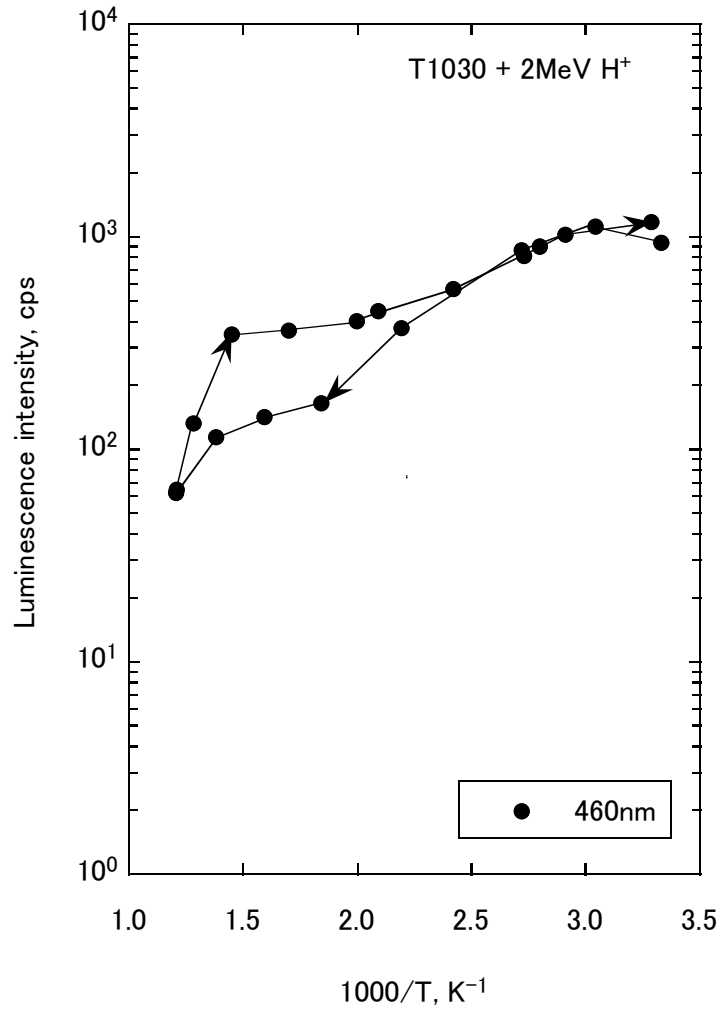
Fig. 3-11. Arrhenius plots of luminscence intensity of T-1030 under 2MeV He$^+$ irradiation with a low beam current of 3nA.

Conduction band

- -

g'_{S1}

T_2

$S_1(\tau=4.2ns)$　　　k_2

$g'_{T1} + g'_{S1}k_8[ODC(S_1)]/(k_7+k_8)$

$T_1(\tau=10.2ms)$

$k_1\ (h\nu_{280})$

k_{11}, k_{12} (recombination)

$k_9, k_{10}\ (h\nu_{460})$

S_0

Valence band

Fig. 3-12. Flat band diagram of vitreous silica summarizing the relative energy positions of ODCs.

Chapter 4

Production and reaction kinetics of radiation-induced defects in α-alumina and sapphire under ion beam irradiation
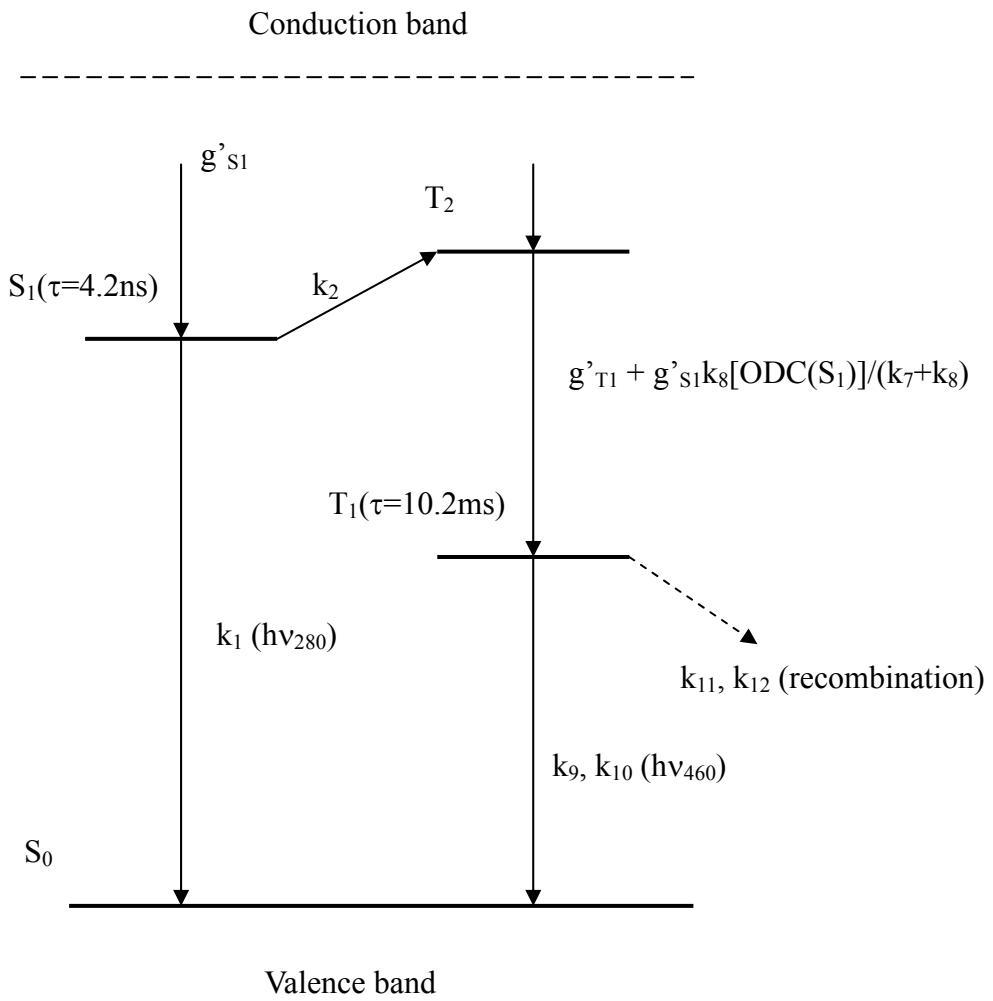
4.1 Introduction

Irradiation behavior of ceramic materials is one of the topics of current interest, since some of these materials are to be used in the strong radiation field of proposed fusion reactors. However, the dynamic production behavior of irradiation defects under irradiation has not been fully clarified in spite of the considerable progress in understanding many aspects of irradiation defects in these ceramic materials.   It is thus important to know the production behavior of irradiation defects by such an in-situ luminescence measurement technique.

For fusion reactor blanket materials, we have already studied the production behavior of irradiation defects in some candidate lithium ceramics by an in-situ luminescence measurement technique under ion beam irradiation [1].   In Li_2O, it has been confirmed that the F^+ center (an oxygen vacancy trapping an electron) and the F^0 center (an oxygen vacancy trapping two electrons), which are commonly observed in ionic compounds, are formed by irradiation [2,3].   Similar irradiation defects of F-type centers are also produced in $LiAlO_2$ [4], Li_2TiO_3, Li_2ZrO_3 and Li_2SnO_3 [5,6].   These defects are considered to play an important role in the tritium behavior [1].

Following the measurement of lithium ceramics, the present study deals with α-alumina and sapphire in which the F-type centers are produced [7-11].   These ceramics are often used as refractory oxide dielectric materials in the radiation field, it is also needed to know the dynamic behavior of the irradiation defects.   In the present study, similarly to the case of lithium ceramics, the luminescence spectra were measured under ion beam irradiation, and the temperature dependence of the luminescence intensity was analyzed by considering the production mechanism and reaction kinetics of the irradiation defects.

4.2 Experimental

The pellet-type specimens of α-alumina (Al_2O_3: 99.9%, SiO_2: 0.04%, Na_2O: 0.02%, MgO: 0.01%, CaO: 0.01%, Fe_2O_3: <0.01% [12]) and sapphire were obtained from Kyocera Co. Ltd., which were of 10 mm in diameter and about 0.5 mm in thickness.   Each specimen was irradiated with a He^+ ion beam, accelerated to 2 MeV with a Van de Graaff accelerator. The range and total number of displacements were estimated to be about 4 μm and 170 displacements/ion, respectively, by using the TRIM code (SRIM-98) with the displacement energies of 20 eV for Al and 50 eV for O.   The size of the ion beam was about 2 mm x 2 mm and its current was monitored.   A photonic multichannel analyzer, Hamamatsu PMA-11 was used to measure the irradiation time dependence of the luminescence.   The temperature of the sample holder was controlled with an electric heater and a thermocouple while another thermocouple was attached to the sample surface to monitor its temperature at a distance close

to beam area.   In the room temperature irradiation, the temperature rise by beam heating was observed to be within a few degrees as estimated by taking the values of thermal diffusion coefficient, density and heat capacity of alumina.   The experimental conditions are summarized in Tables 4.1 and 4.2.

4.3 Results and discussion
4.3.1 Luminescence bands

Fig. 4-1 shows typical luminescence spectra of α-alumina under He$^+$ ion beam irradiation and Fig. 4-2 shows those of sapphire under H$^+$ irradiation.   For comparison, the ordinate represents luminescence intensity normalized to the beam current of 10 nA/cm^2; the peak heights have been observed to be proportional to the beam current and then all of the spectra in the present study are corrected with the beam current.   Similar spectra were also observed for other cases.   As shown in Fig. 4-1, the observed luminescence spectra are decomposed into a number of luminescence bands, namely 330nm, 420 nm and others.   For the decomposition, following the manner in the previous study [5], energy-based Gaussian functions were taken for all the luminescence bands and the peak heights and positions were determined.

In the case of α-alumina and sapphire, there have been reported a number of F-type centers including the F$^+$ and F^0 centers [7].   As for the luminescence of irradiation defects, it is known that the luminescence of the F$^+$ center is observed at the UV region around 3.8eV (325nm) while that of the F^0 centers is observed at a lower photon energy region around 3.0eV (410nm).   Thus the presently observed luminescence from α-alumina and sapphire which is centered at 330 and 420nm can be attributed to the F$^+$ and F^0 centers.   As for the others, it is noted that the luminescence at 250nm and 290nm is also observed in the case of α-alumina.   The luminescence intensity at these bands was found to be sensitive to thermal annealing at higher temperatures, and then might be attributed to the effect of some impurities such as OH.   It was also found that the effect is more clearly observed in the case of H$^+$ irradiation.   This may be explained by considering the local reactions of irradiation defects in the ion tracks.   Specific ionization and hence the local concentration of irradiation defects are lower for H$^+$ than for He$^+$ and are much affected by such impurities.

As shown in Fig. 4-3, in the present experiment, it has been observed that the luminescence intensities at 330 and 420nm show an irradiation history in which the intensities increase with irradiation time and reach the steady-state ones.   By annealing the irradiated specimens above 1073K for some tens minutes, such an irradiation history has been observed repeatedly.   This fact suggests that a considerable part of the luminescence comes from the defects accumulated by irradiation and that the intensities at these bands may reflect the amounts of the F$^+$ and F^0 centers.   A similar irradiation history has also been reported by Al Ghamdi and Townsend [8], who have measured the ion beam induced luminescence of sapphire.   In their case, however, they have observed non-zero values for the luminescence intensity at a low fluence, and have suggested that the luminescence is from intrinsic color centers activated by excited electrons.   In the present case, on the other hand, nearly zero
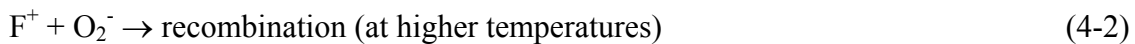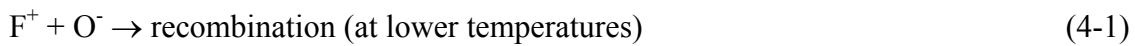
45

values have been observed with annealed specimens and it follows that the luminescence originates from the F^+ and F^0 centers accumulated by irradiation.

In their experiment with electron irradiated sapphire [9], Morono and Hodgson have found that the peak height ratio between the F^+ and F^0 is strongly dependent on the dose rate and that the F^+ luminescence increases with the dose rate while the F^0 luminescence decreases. Since the F^+ is hardly accumulated in the electron irradiated sapphire, this dose rate effect has been explained by considering the conversion of the F^0 to the F^+; the F^0 is excited by electron and hole capture and this excited F^0 is ionized by hole capture giving the F^+ [9]. In the present case, on contrast, such a dose rate effect was hardly observed in the studied region, possibly due to low dose rates compared with the above case. Thus the presently observed luminescence intensities at 330 and 420nm are considered to represent the accumulated F^+ and F^0 centers, respectively.

4.3.2. Temperature dependence of steady-state luminescence intensity

Figs. 4-4(a) and (b) show the Arrhenius plots of the steady-state luminescence intensity of α-alumina under H^+ and He^+ irradiation, respectively. Similarly, Figs. 4-5(a) and (b) show the luminescence intensity of sapphire under H^+ and He^+ irradiation, respectively. As shown in these figures, the intensity at 330nm decreases monotonically with the increasing temperature up to 800K. It seems to show that recombination proceeds at higher temperatures. In the case of the 420nm luminescence, on the other hand, some non-monotonic temperature dependence can be seen; the intensity decreased with the temperature up to 600K, and then increased above this temperature. In this case, not only recombination but also some additional production of the F^0 centers seem to be involved in the reaction scheme.

In the case of ionic compounds such as alumina, it is considered that the formation of such F-type defect centers of the F^+ and F^0 is accompanied with the formation of the interstitial O^- and O^0, respectively. In addition to these, the O_2^- and O_2 may be formed by the reactions of $O^- + O^0 \rightarrow O_2^-$ and $O^0 + O^0 \rightarrow O_2$, although the diffusion of the O_2^- and O_2 will be much slower than the O^- and O^0. Thus the following production mechanism of irradiation defects in α-alumina and sapphire can be suggested:

$$Al_2O_3 \rightarrow Al_2O_3{}^* \rightarrow F^+, F^0 \tag{4-0}$$
$$F^+ + O^- \rightarrow \text{recombination (at lower temperatures)} \tag{4-1}$$
$$F^+ + O_2^- \rightarrow \text{recombination (at higher temperatures)} \tag{4-2}$$
$$F^+ + O_2^- \rightarrow F^0 + O_2 \text{ (additional } F^0 \text{ production at higher temperatures)} \tag{4-3}$$
$$F^0 + O^0 \rightarrow \text{recombination (at lower temperatures)} \tag{4-4}$$
$$F^0 + O_2 \rightarrow \text{recombination (at higher temperatures)} \tag{4-5}$$

Reaction (4-0) represents the production of an excited Al_2O_3 ($Al_2O_3{}^*$) by ion beam irradiation, which is de-excited to F^+ and F^0. Reactions (4-1) and (4-2) represent the recombination of the F^+ with the O^- and O_2^-, respectively, while reaction (4-3) is to account for the additional

production of the F^0 in the higher temperature region. Because of its larger size, the O_2^- is considered to be more responsible for reaction (4-3) in the higher temperature region than the O^-. Similarly to the case of the F^+, reactions (4-4) and (4-5) represent the recombination of the F^0 with the O^0 and O_2, respectively. All the reactions (4-1) to (4-5) are the second-order, but are treated as the first-order of the F^+ or F^0 in the following analysis for simplicity. In fact, for example, such an F^+ center is considered to be associated with an O^- interstitial under Coulomb interaction in the form of $(F^+ \cdot O^-)$ as suggested for Li_2O [2,3], and its reaction may be treated as the first-order.

According to the literature [7], the luminescence at 3.8eV (325nm) is attributed to the singlet (2P to 1S*) emissions of the F^+ centers and 3.0eV (410nm) the triplet (^{3}P to ^{3}S*) of the F^0 centers, as shown in Fig. 4-6. Since the luminescence is caused from the F^+ and F^0 activated by excited electrons, the observed luminescence intensities I_{330} and I_{420} at 330nm and 420nm are proportional to the state densities of $[F^+(1A)]$ and $[F^0(^1S)]$, as given by:

$$I_{330} = c_{F+}[F^+(1A)] \qquad (4\text{-}6)$$
$$I_{420} = c_{F0}[F^0(^1S)] \qquad (4\text{-}7)$$

where c_{F+} and c_{F0} are constants. The steady-state luminescence intensities have been measured in the present experiment, and then a steady-state approximation is applied to these states, that is:

$$d[F^+]/dt = g_{F+} - k_1[F^+] - k_2[F^+] - k_3[F^+] = 0 \qquad (4\text{-}8)$$
$$d[F^0]/dt = g_{F0} + k_3[F^+] - k_4[F^0] - k_5[F^0] = 0 \qquad (4\text{-}9)$$

where g_{F+} and g_{F0} are the generation rate of F^+ and F^0 by reaction (4-0).

For the analysis of the observed temperature dependence of the luminescence intensity, Eqs. (4-8) and (4-9) are solved to obtain the steady-state densities of the F^+ and F^0 which are substituted into Eqs. (4-6) and (4-7). The rate constants are assumed to be of the Arrhenius type, and hence the pre-exponential term A_i and activation energy term E_i are determined in the analysis. Since the number of the parameters is so large and some of those are not independent, further assumptions are made for a proper convergence. By considering that the energy needed for the defect production and the defect reactions are essentially the same in the same specimen, the activation energy is assumed to be the same irrespective of the different projectile ions, H^+ or He^+ Also, the activation energy values for reactions (4-1) and (4-4) which are considered to be low are assumed to be zero, that is $E_1 = 0$ and $E_4 = 0$. As shown in Figs. 4-4 and 4-5, in fact, each luminescence intensity is rather constant in the lower temperature region, indicating very low activation energy of reactions (4-1) and (4-4). The others of the pre-exponential terms and the generation rates are treated to be independent as much as possible in order to make the differences clear. With these assumptions, Eqs. (4-6) and (4-7) are thus rewritten as

$$I_{330} = \frac{\left(\dfrac{C_{F+}g_{F+}}{A_1}\right)}{1 + \left(\dfrac{A_2}{A_1}\right) \cdot \exp\left(-\dfrac{E_2}{RT}\right) + \left(\dfrac{A_3}{A_1}\right) \cdot \exp\left(-\dfrac{E_3}{RT}\right)} \tag{4-10}$$

$$= \frac{g_{F+}'}{1 + k_2' + k_3'}$$

$$I_{420} = \frac{\left(\dfrac{C_{F0}g_{F0}}{A_4}\right) + \left(\dfrac{C_{F0}A_1}{C_{F+}A_4}\right) \cdot \dfrac{\left(\dfrac{C_{F+}g_{F+}}{A_1}\right) \cdot \left(\dfrac{A_3}{A_1}\right) \cdot \exp\left(-\dfrac{E_3}{RT}\right)}{1 + \left(\dfrac{A_2}{A_1}\right) \cdot \exp\left(-\dfrac{E_2}{RT}\right) + \left(\dfrac{A_3}{A_1}\right) \cdot \exp\left(-\dfrac{E_3}{RT}\right)}}{1 + \left(\dfrac{A_5}{A_4}\right) \cdot \exp\left(-\dfrac{E_5}{RT}\right)} \tag{4-11}$$

$$= \frac{g_{F0}' + C' \cdot \dfrac{g_{F+}' \cdot k_3'}{1 + k_2' + k_3'}}{1 + k_5'}$$
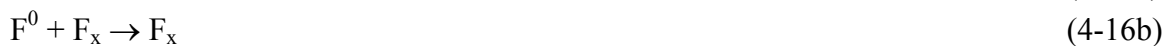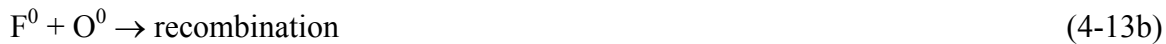
The measured luminescence intensity data were fitted to Eqs. (4-10) and (4-11) by least-squares method, and the parameter values were obtained as summarized in Table 2. As shown in Figs. 4-3(a), 4-3(b), 4-4(a) and 4-4(b), the agreements are satisfactorily good in all the cases.

The activation energy values are obtained to be 78.8 kJ/mol, 141.9 kJ/mol, 37.2 kJ/mol for E_2, E_3, and E_5, respectively, in the case of α-alumina while those are 84.5 kJ/mol, 205.0 kJ/mol, 80.5 kJ/mol in sapphire. In view of the reaction scheme, these values are considered to correspond to those of the diffusion of the O_2^- and O_2. In the present analysis, however, it is reminded that the activation energy values for reactions (4-1) and (4-4) are assumed to be zero, and the obtained E_2, E_3, and E_5 values may be of approximate ones. In spite of this limitation, it seems that the obtained E_2, E_3, and E_5 values are higher in sapphire than those in α-alumina, reflecting some differences in both materials. As for the pre-exponential term A_i, it is noted that the A_2/A_1, A_3/A_1 and A_5/A_4 values with He^+ irradiation are higher than those with H^+ irradiation in every case. This may be due to the difference in specific ionization between both projectile ions. The specific ionization of He^+ is much higher than that of H^+, and all the reactions of irradiation defects are enhanced with He^+ irradiation. An interesting difference is also found in the g'$_{F+}$ and g'$_{F0}$ values. Different g'$_{F0}$ values are obtained with different projectile ions while no apparent difference is obtained for the g'$_{F+}$. By taking into account the lifetimes of $F^+(2P)$ and $F^0(^3P)$, an explanation may be given as follows. In the case of $F^+(2P)$, the lifetime in the order of 10^{-9} s [10,11] is too short to be involved in the defect reactions especially at lower temperatures. On the other hand, the lifetime of the $F^0(^3P)$ in the triplet state is considerably longer (25ms [11]), and the defect reactions are likely to affect and reduce the luminescence yield even at lower temperatures, as observed in the present study.

4.3.3 Irradiation time dependence of luminscence intensity

    Figs. 4-7 and 4-8 show typical results of the measurement of α-alumina and sapphire, respectively, in which the luminescence intensity is given in cps for a fixed window of 0.75nm.　It is shown that the luminescence intensities at 330 and 420 nm show an irradiation history in which the intensities increase with irradiation time and reach the maximum ones, and that the intensities decrease at the longer irradiation in some cases.　By annealing the irradiated specimens above 1073 K for some tens minutes, such an irradiation history has been observed repeatedly, as mentioned in 4.3.1.　This fact suggests that a considerable part of the luminescence comes from the defects accumulated by irradiation and that the intensities at these bands may reflect the amounts of the F^+ and F^0 centers.　The possibility of using this technique to monitor radiation-induced defects is thus indicated.

    In the case of ionic compounds such as alumina, it is considered that the formation of such F-type defect centers of the F^+ and F^0 is accompanied with the formation of the interstitial O^- and O^0, respectively.　In addition to these, the O_2^- and O_2 may be formed by the reactions of $O^- + O^0 \rightarrow O_2^-$ and $O^0 + O^0 \rightarrow O_2$, although the diffusion of the O_2^- and O_2 will be much slower than the O^- and O^0.　Also, the formation of some cluster defects, denoted by F_x inclusively, may be expected from the reactions of F-type defect centers. Thus, similarly to the reaction scheme in 4.3.2, but considering only the reactions at relatively lower temperatures of the present study, the following production and reaction mechanism of radiation-induced defects in α-alumina and sapphire can be suggested:

$$Al_2O_3 \rightarrow Al_2O_3{}^* \rightarrow F^+ + O^- \tag{4-12a}$$

$$Al_2O_3 \rightarrow Al_2O_3{}^* \rightarrow F^0 + O^0 \tag{4-12b}$$

$$F^+ + O^- \rightarrow recombination \tag{4-13a}$$

$$F^0 + O^0 \rightarrow recombination \tag{4-13b}$$

$$O^- + O^0 \rightarrow O_2^- \tag{4-14a}$$

$$O^0 + O^0 \rightarrow O_2 \tag{4-14b}$$

$$F^+ + F_x \rightarrow F_x \tag{4-15}$$

$$F^0 + F^0 \rightarrow F_x \tag{4-16a}$$

$$F^0 + F_x \rightarrow F_x \tag{4-16b}$$

Reactions (4-12a) and (4-12b) represent the production of the F^+ and F^0, respectively, through an excited Al_2O_3 ($Al_2O_3{}^*$) by ion beam irradiation.　Reactions (4-13a) and (4-13b) represent the recombination of the F^+ and F^0 with the O^- and O^0, respectively, while reactions (4-14a) and (4-14b) the formation of the O_2^- and O_2.　Because of their larger sizes, the O_2^- and O_2 are considered to be hardly responsible for further reactions at the lower temperatures. Reactions (4-15), (4-16a) and (4-16b) represent the formation of cluster defects F_x.　It is important to note that the reaction rate constants are treated as the same for similar reactions in the following analysis for simplicity; k_{13} for reactions (4-13a), (4-13b), (4-14a) and (4-14b), k_{15} for reaction (4-15), and k_{16} for reactions (4-16a) and (4-16b).　The values of the rate

constants may be given in atomic fraction for example.

According to the literature [7], the luminescence at 3.8 eV (325 nm) is attributed to the singlet (2P to 1S*) emissions of the F^+ centers and 3.0 eV (410 nm) the triplet (^{3}P to ^{3}S*) of the F^0 centers.   Considering that the luminescence is caused from the F^+ and F^0 activated by excited electrons or electron-hole pairs, the observed luminescence intensities I_{330} and I_{420} at 330nm and 420nm are proportional to the state densities of [F^+(1A)] and [F^0(^{1}S)], as given by:

$$I_{330} = \varepsilon_{F+} \, \phi \, [F^+(1A)] \qquad\qquad (4\text{-}17)$$
$$I_{420} = \varepsilon_{F0} \, \phi \, [F^0(^1S)] \qquad\qquad (4\text{-}18)$$

where ε_{F+} and ε_{F0} represent the luminescence detection efficiencies including geometric factors and excitation probabilities and ϕ the ion beam current.   The variation of the state densities of [F^+(1A)] and [F^0(^{1}S)] with irradiation time can be calculated by solving the following equations:

$$d[F^+]/dt = g_{F+} \, \phi - k_{13}[F^+][O^-] - k_{15}[F^+][F_x] \qquad\qquad (4\text{-}19)$$
$$d[F^0]/dt = g_{F0} \, \phi - k_{13}[F^0][O^0] - 2k_{16}[F^0]^2 - k_{16}[F^0][F_x] \qquad\qquad (4\text{-}20)$$
$$d[O^-]/dt = g_{F+} \, \phi - k_{13}[F^+][O^-] - k_{13}[O^-][O^0] \qquad\qquad (4\text{-}21)$$
$$d[O^0]/dt = g_{F0} \, \phi - k_{13}[F^0][O^0] - k_{13}[O^-][O^0] - 2k_{13}[O^0]^2 \qquad\qquad (4\text{-}22)$$
$$d[F_x]/dt = k_{16}[F^0]^2 \qquad\qquad (4\text{-}23)$$

where g_{F+} and g_{F0} are the generation rate of F^+ and F^0 by reactions (4-12a) and (4-12b), respectively.   One can estimate the values of the g_{F+} and g_{F0} from a conversion factor of 1 dpa (for oxygen) = 1.08×10^{17} ions/cm^2 (2.0 MeV He$^+$), which is obtained as a weighted average value along ion tracks by using the TRIM code (SRIM-98) with the displacement energies of 20 eV for Al and 50 eV for O.   Considering the fractions of the surviving defects from cascade reactions, one tenth of the conversion factor is temporalily taken for each of the g_{F+} and g_{F0} in the present study.

For the analysis of the observed results, Eqs. (4-19) to (4-23) are solved by the Runge-Kutta method to obtain the steady-state densities of the F^+ and F^0 which are substituted into Eqs. (4-17) and (4-18).   As already mentioned above, the reaction rate constants are treated as the same for similar reactions in the present analysis; k_{13} for reactions (4-13a), (4-13b), (4-14a) and (4-14b), k_{15} for reaction (4-15), and k_{16} for reactions (4-16a) and (4-16b). The measured luminescence intensity data were fitted to Eqs. (4-17) and (4-18) combined with Eqs. (4-19) to (4-23) by the least-squares method, and the parameter values were obtained.   As shown in Figs. 4-7 and 4-8, the agreements are satisfactorily good in all the cases.

As typical results of the present analysis, Figs. 4-9(a) and (b) show the variations of the defect densities with irradiation time in alumina and sapphire, respectively, which are simulated by using the obtained parameter values for the observed luminescence in Figs. 4-7(a) and 4-8(b).   The densities of the O^- and O^0 reach the steady state rapidly, and those

50

of the F^+ and F^0 follow to reach a little slowly.   Different kinetics of the F^+ and F^0 are shown in the figure, in which the density of the F^+ increases rather monotonically while the F^0 increases and then decreases.   This difference may be due to different rate constants in Eqs. (4-19) and (4-20); the k_{15} for reaction (4-15) will be smaller than the k_{16} for reactions (4-16a) and (4-16b) possibly because of some repulsive forces between the F^+ and positively charged F_x.   It is interesting to point out that the formation of the cluster defects F_x starts above the dpa value of 10^{-3}, for comparison with the results of other methods such as optical absorption measurements [13].

Figs. 4-10(a), (b) and (c) show the Arrhenius plots of the rate constants of k_1, k_3 and k_4, respectively, which are obtained from the present analysis.   No apparent difference is observed for α-alumina and sapphire.   As shown in Table 4-4, the Arrhenius equations of the rate constants are obtained by the least-squares fitting, and the activation energies are obtained to be 0.14 ± 0.03, 0.11 ± 0.03, and 0.07 ± 0.04 eV for k_{13}, k_{15} and k_{16}, respectively. According to a comprehensive review of Zinkle and Kinoshita [13], there is relatively little information available on the interstitial migration energies for Al_2O_3, though it appears that both Al and O interstitials are mobile in Al_2O_3 near and below room temperature.   It can be considered that reactions (4-13a) to (4-14b) may be limited by the migration of O, of which the activation energy is obtained to be 0.14 eV in the present study.   As for the k_3 and k_4, it is noticed that the activation energies of 0.11 and 0.07 eV are considerably small compared with the migration energies of 1.8-2 eV [13] for O vacancies.   An explanation for this difference is as follows.   In the case of ion irradiation, there will be overlaps of ion tracks, which increase with the increasing dpa value.   Then, defects once formed, including not only point defects of the F^+ and F^0 but also cluster defects F_x, may be involved in another ion track in which reactions (4-15) to (4-16b) proceed.   The activation energies of such reactions will be small as observed in the present study.

It is interesting to compare the present results with the literature ones.   One is for oxygen interstitials.   In the case of alkali halides, different types of oxygen interstitial traps, extrinsic and intrinsic, are known to be present and to affect the F-coloring and F-thermal-annealing curves [14].   Similarly to the case of alkali halides, it has been reported that there are different components related to the different types of oxygen interstitial traps in sapphire under electron beam irradiation [15].   In that case, two types of interstitial traps were identified, of which the activation energies for detrapping the interstitial were obtained to be 0.32 and 0.18 eV.   Compared with those results, a little lower value of 0.14 eV is obtained in the present study, not for the detrapping but for the migration of interstitials. Under the present conditions of ion beam irradiation, an efficient defect production occurs and results in a relatively higher concentration of interstitials.   The effects of various interstitial traps other than the F-type centers are thus negligible, similarly to the case of alkali halides exposed to high dose [16], and the activation energy for the migration of interstitials is successfully determined in the present case.

Another one is for the cluster defects F_x.   Considering the F_x curve in Fig. 3, one would expect the observation of the F_x in the present specimens.   In fact, such aggregate

51

centers as F_2^+ and F_2 have been identified to be formed in neutron-irradiated single crystal α-Al_2O_3 [17]. For comparison, some specimens of sapphire in the present study were subjected to the absorption measurement, but only a slight and broad absorption was observed over the range studied from 200 to 800nm. This might be due to too small (narrow and thin) damage regions which are confined within less than 1% of the specimen volume in the present case. Also, no apparent luminescence of such aggregate centers was identified in the observed luminescence spectra, as mentioned in 4-3-2. Considering possible formation of Al colloids at higher doses, more careful measurements may be needed for observation and details of the F_x.

As for the luminescence detection efficiency, different temperature dependences of the ε_{F+} and ε_{F0} were obtained in the analysis; the ε_{F+} is almost constant while the ε_{F0} decreases at the higher temperatures above 450 K. Then, by eliminating the scatters due to the geometric factors, the ratio of the luminescence detection efficiency of the F^0 to that of the F^+ is plotted in Fig. 4-11. It can be seen that the $\varepsilon_{F0} / \varepsilon_{F+}$ rapidly decreases like a thermal quenching. The following equation is thus tentatively applied for the analysis, which has originally been applied to temperature-dependent F center luminescence in alkali halides by Swank and Brown [18]:

$$(\varepsilon_{F0} / \varepsilon_{F+}) = C / [1 + (\tau_R / \tau_0) \, e^{-\Delta E/kT}] \tag{4-24}$$

where C is a constant, τ_R a radiative life time, and $(1/\tau_0) \, e^{-\Delta E/kT}$ the probability of thermal activation into a nonradiative decay channel, with activation energy ΔE. In the present case, the parameter values are obtained to be $C = 10^{-0.31 \pm 0.07}$, $(\tau_R / \tau_0) = 10^{7.80 \pm 1.72}$ and $\Delta E = 0.70 \pm 0.17$ eV. For details of this thermal quenching, it is noticed that, in addition to thermal ionization, there may be possible contributions of such an ionization of the F^0 by hole capture at some conditions, as suggested for electron irradiated sapphire [9]. Further studies are thus needed for the reaction kinetics above 450K.

4.4 Conclusions

In order to know the production behavior of irradiation defects in α-alumina and sapphire, the temperature dependence of the luminescence intensity was studied by an in-situ luminescence technique. The temperature dependence of the 330nm luminescence was well explained by considering the production of the F^+ centers with some competing reactions. In the case of the 420nm luminescence of the F^0, its non-monotonic temperature dependence was also interpreted by considering a number of competing reactions including the production of the F^0 at higher temperatures. Some of the defect centers were thus confirmed to be formed and to play a critical role in the reaction scheme at high temperatures, at which these ceramic materials would be used.

At lower temperatures, the observed irradiation time dependence of the luminescence intensity under irradiation was confirmed to reflect the accumulation behavior of radiation-induced defects by its reproducibility with annealing. The results were

successfully analyzed by considering a production and reaction mechanism of radiation-induced defects, which included the formation of cluster defects. By taking an estimated generation rate for point defects, the accumulation behavior of radiation-induced defects was obtained in the unit of atomic fraction. It was shown that the formation of the cluster defects F_x starts above the dpa value of 10^{-3}.

References

[1] H. Moriyama, S. Tanaka, K. Noda, J. Nucl. Mater. 258-263 (1998) 587.

[2] Y. Asaoka, H. Moriyama, K. Iwasaki, K. Moritani, Y. Ito, J. Nucl. Mater. 183 (1991) 174.

[3] Y. Asaoka, H. Moriyama, Y. Ito, Fusion Technol. 21 (1992) 1944.

[4] Y. Asaoka, H. Moriyama, K. Iwasaki, K. Moritani and Y. Ito, J. Nucl. Mater. 191-194 (1992) 268.

[5] H. Moriyama, T. Nagae, K. Moritani, Y. Ito, Nucl. Instr. and Meth. B91 (1994) 317.

[6] K. Moritani, S. Tanaka, H. Moriyama, J. Nucl. Mater. 281 (2000) 106.

[7] B. D. Evans, J. Nucl. Mater. 219 (1995) 202.

[8] A. Al Ghamdi, P. D. Townsend, Nucl. Instrum. Methods B46 (1990) 133.

[9] A. Morono, E. R. Hodgson, J. Nucl. Mater. 249 (1997) 128.

[10] S. Y. La, R. H. Bartram, R. T. Cox, J. Phys. Chem. Solids 34 (1973) 1079.

[11] R. Toshima, H. Miyamaru, J. Asahara, T. Murasawa, A. Takahashi, J. Nucl. Sci. Technol. 39 (2002) 15.

[12] K. Oda, T. Yoshio, J. Am. Ceram. Soc. 80 (1997) 3233.

[13] S. J. Zinkle, C. Kinoshita, J. Nucl. Mater. 251 (1997) 200.

[14] E. R. Hodgson, A. Delgado, J. L. Alvarez Rivas, Phys. Rev. B18 (1978) 2911.

[15] A. Morono, E. R. Hodgson, J. Nucl. Mater. 307-311 (2002) 1246.

[16] D. F. Mariani, J. L. Alvarez Rivas, J. Phys. C: Solid St. Phys. 11 (1978) 3499.

[17] K. Atobe, N. Nishimoto, M. Nakagawa, Phys. Stat. Sol. (a) 89 (1985) 155.

[18] R. L. Swank, F. C. Brown, Phys. Rev. 130 (1963) 34.

Table 4-1. Experimental conditions for steady-state luminescence measurement.

Specimen	Irradiation condition		
	Projectile	Beam current (nA/cm^2)	Temperature (K)
α-alumina	2MeV H$^+$	10 - 240	302 - 904
	2MeV He$^+$	10 - 900	300 - 799
sapphire	2MeV H$^+$	20 – 150	298 - 824
	2MeV He$^+$	120 - 900	307 - 789

Table 4-2. Experimental conditions for measurement of irradiation time dependence of luminescence intensity.

Specimen	Irradiation condition			Steady state luminescence intensity (cps) at:	
	Projectile	Temperature[a] (K)	Beam current (nA/cm^2)	330nm	420nm
α-alumina	2MeV He$^+$	298	63	≥6000	≈2000
		298	81	≥6000	≈1000
		423	164	≥14000	≈2800
		423	238	≈8000	≈2000
		448	67	≈3500	≈600
		473	81	>4000	≈100
		473	131	≈13000	≈200
		523	77	≈4500	≈200
Sapphire	2MeV He$^+$	298	66	≈8000	≈2800
		300	133	≥6000	≈1700
		323	119	≈11000	≈2000
		373	514	≈25000	≈6000
		423	133	≈17000	≈6000
		448	75	≥1400	≈500
		523	140	≈7000	≈300

[a] Temperature of the thermocouple attached to the sample surface to monitor its temperature.

Table 4-3.   Optimum parameter values obtained from the analysis of in-situ luminescence measurement data.

Specimen	Projectile	$k_2' = A_2/A_1\exp[-E_2/RT]$		$k_3' = A_3/A_1\exp[-E_3/RT]$		$g_{F+}' = \dfrac{C_{F+}g_{F+}}{A_1}$ (s^{-1})
		A_2/A_1	E_2(kJ/mol)	A_3/A_1	E_3(kJ/mol)	
α-Al$_2$O$_3$	H$^+$	2.3×10^7	78.8	2.7×10^9	141.9	5.3×10^3
	He$^+$	6.4×10^7	$(78.8)^{1)}$	2.6×10^{11}	$(141.9)^{1)}$	3.9×10^3
sapphire	H$^+$	9.1×10^7	84.5	9.3×10^{15}	205.0	5.6×10^3
	He$^+$	9.3×10^8	$(84.5)^{1)}$	2.1×10^{17}	$(205.0)^{1)}$	6.5×10^3

Specimen	Projectile	$k_5' = A_5/A_4\exp[-E_5/RT]$		$C' = \dfrac{C_{F0}A_1}{C_{F+}A_4}$	$g_{F0}' = \dfrac{C_{F0}g_{F0}}{A_4}$ (s^{-1})
		A_5/A_4	E_5(kJ/mol)		
α-Al$_2$O$_3$	H$^+$	2.3×10^4	37.2	2.7×10^0	2.2×10^3
	He$^+$	3.7×10^4	$(37.2)^{1)}$	3.0×10^0	7.1×10^2
sapphire	H$^+$	2.4×10^9	80.5	3.5×10^2	4.7×10^3
	He$^+$	4.2×10^9	$(80.5)^{1)}$	6.3×10^1	8.8×10^2

1) Assumed to be the same for the same specimen.

Table 4-4.   Reaction rate constants obtained from the analysis of in-situ luminescence measurement data.

Rate constants	$k_i = A_i \exp[-E_i/kT]$	
	A_i	E_i (eV)
K_{13}	$10^{2.9\pm0.3}$	0.14 ± 0.02
K_{15}	$10^{1.2\pm0.5}$	0.11 ± 0.03
K_{16}	$10^{1.1\pm0.5}$	0.06 ± 0.04
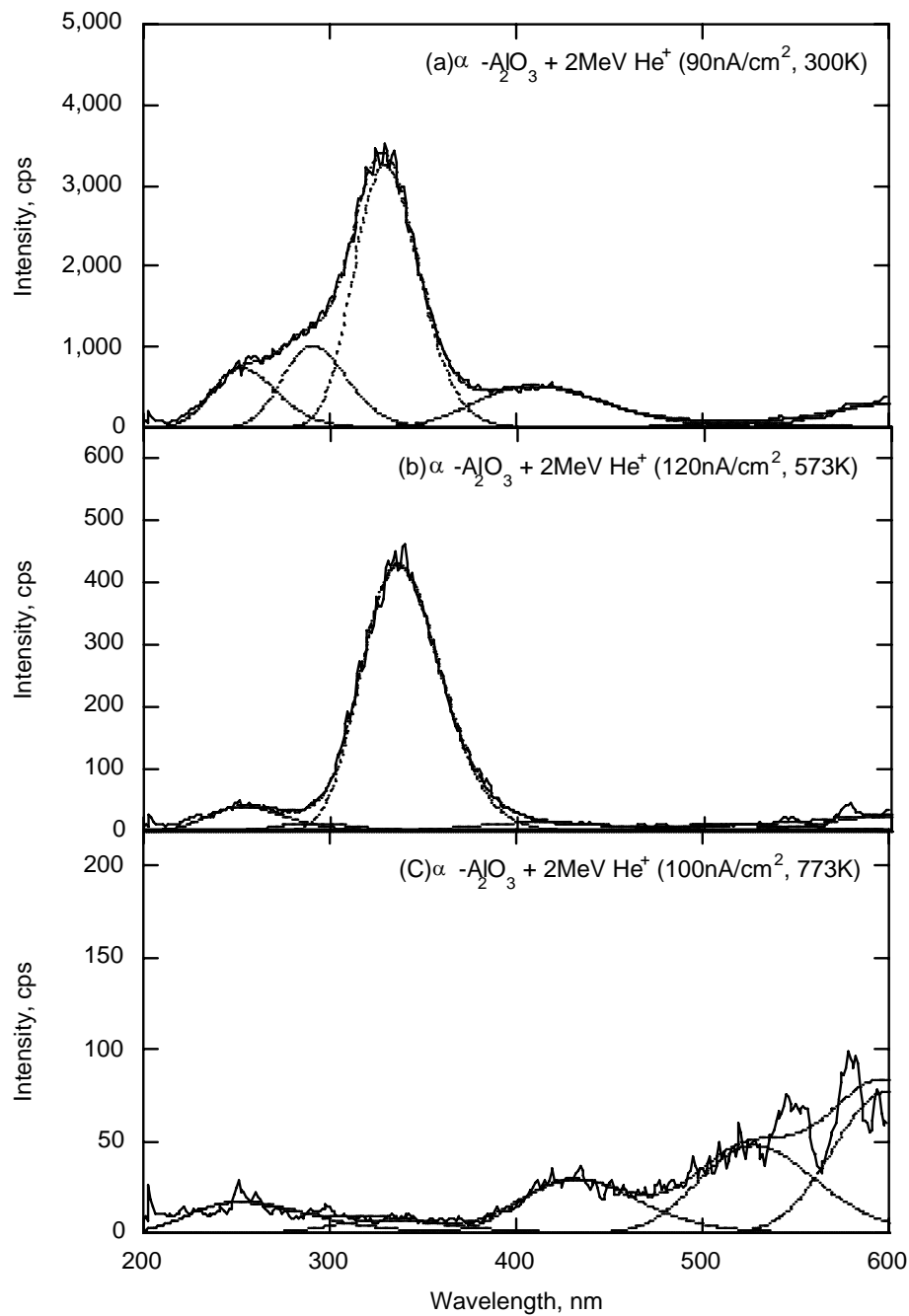
Fig. 4-1. Typical luminescence spectra of α-alumina under 2MeV He$^+$ ion beam irradiation.   The ordinate represents luminescence intensity normalized to the beam current of 10nA/cm^2.   Curves represent the results of decomposition as described in 4.3.1.
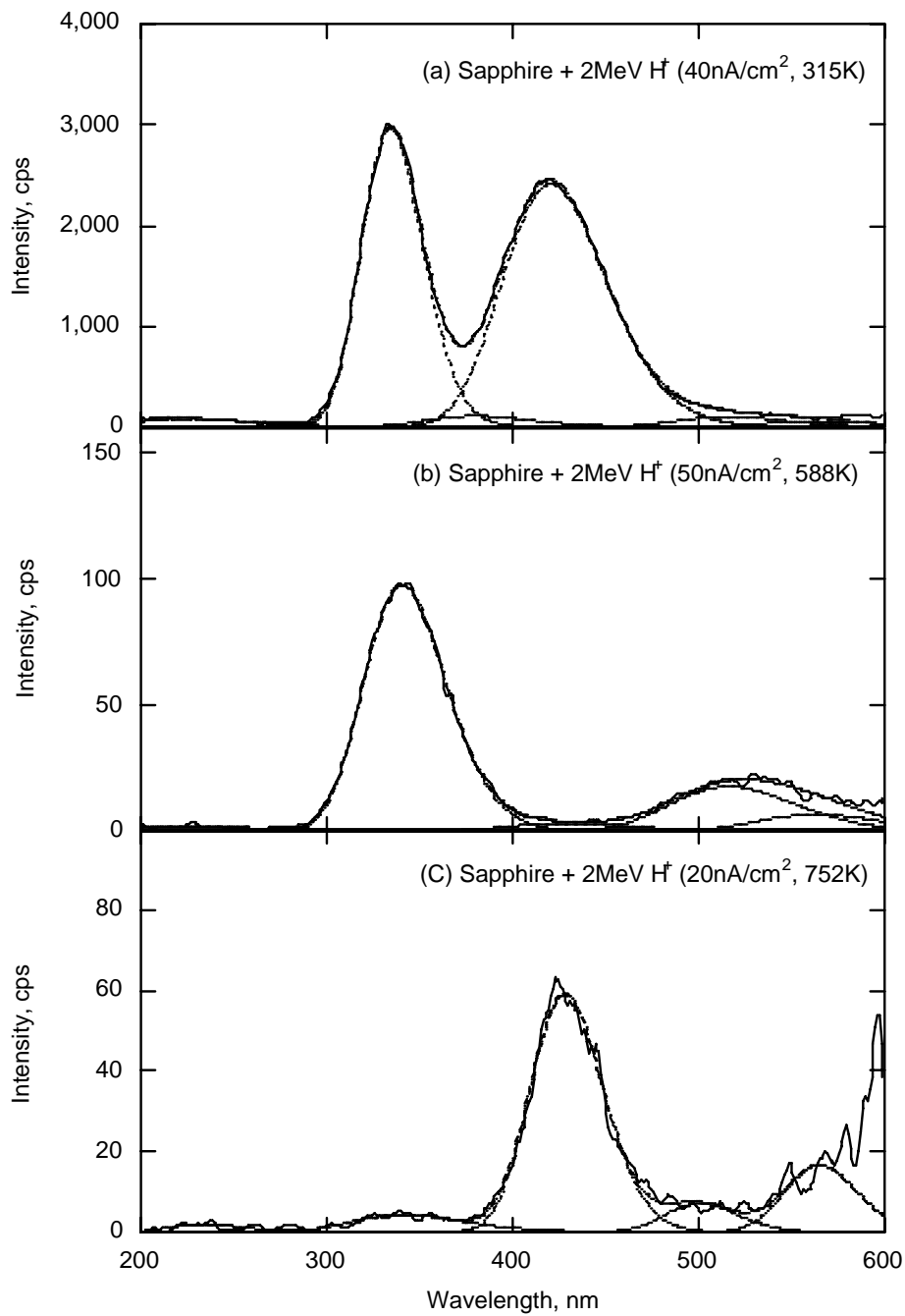
Fig. 4-2. Typical luminescence spectra of sapphire under 2MeV H$^+$ ion beam irradiation. The ordinate represents luminescence intensity normalized to the beam current of 10nA/cm^2.   Curves represent the results of decomposition as described in 4.3.1.
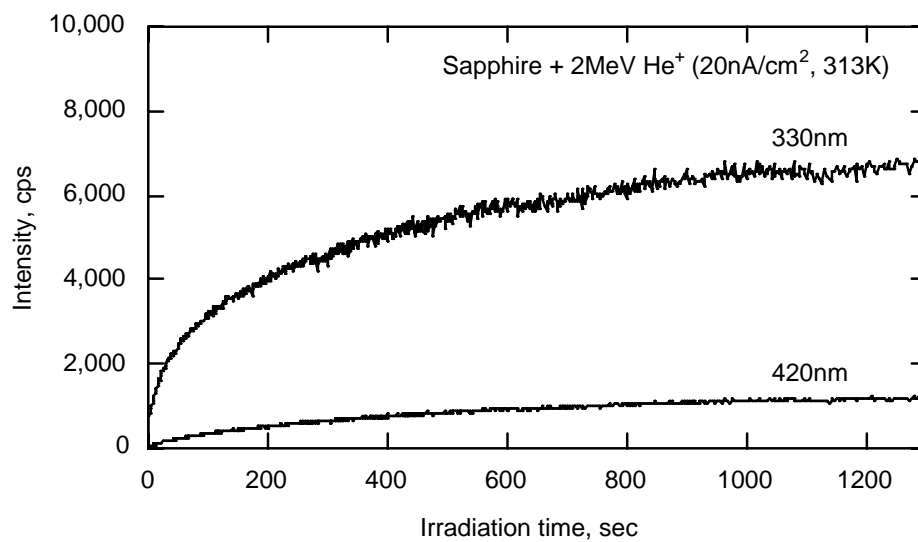
Fig. 4-3.   Irradiation time dependence of the luminescence from sapphire under 2MeV He[+] irradiation at 313K.   The specimen was annealed above 1073K for 10 minutes.
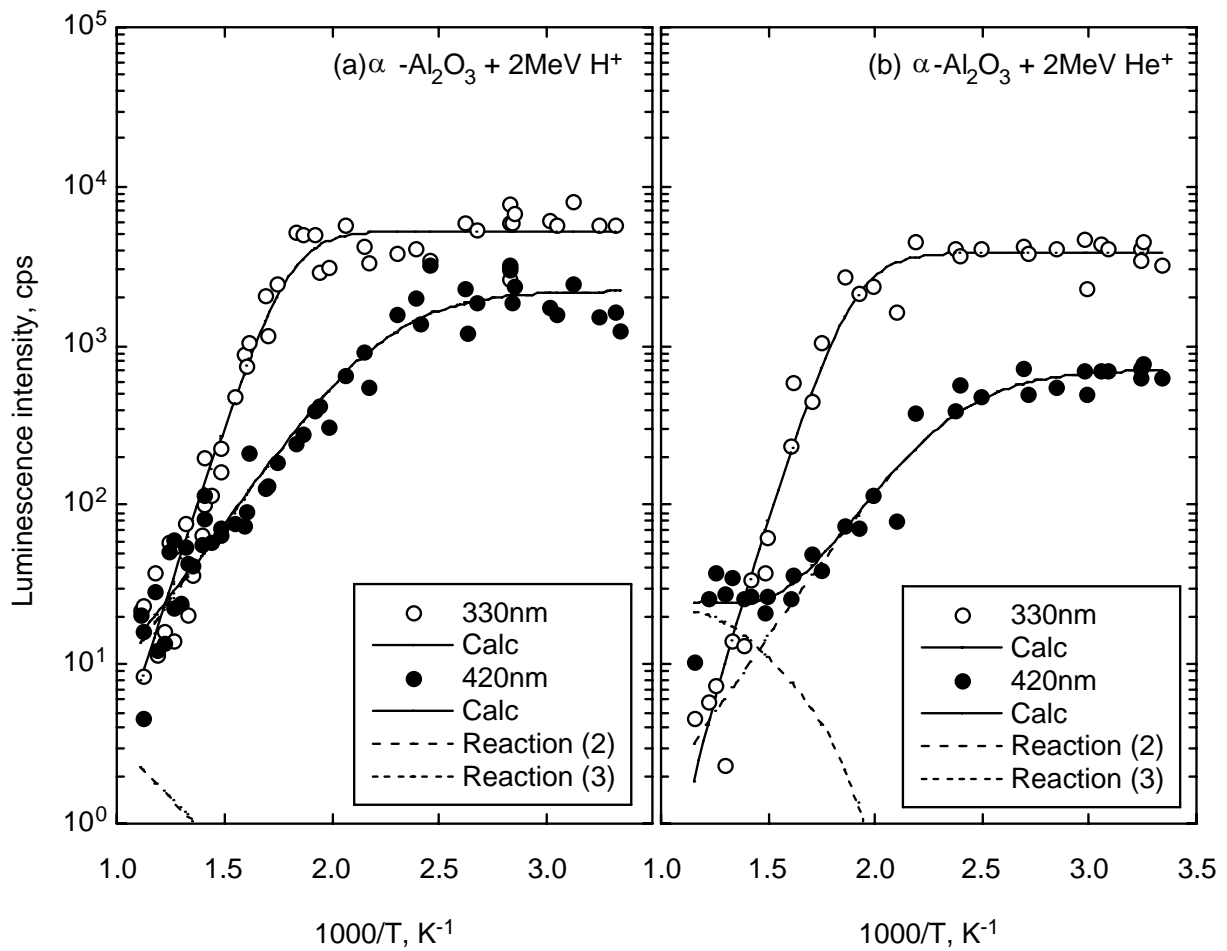
Fig. 4-4. Arrhenius plots of luminscence intensity of α-alumina under (a) 2MeV H$^+$ and (b) 2MeV He$^+$ irradiation. The ordinate represents luminescence intensity normalized to the beam current of 10nA/cm^2. Marks are experimental and curves represent the least-squares fits of the data to Eqs. (4-10) and (4-11) as described in 4.3.2. Contributions of reactions (4-2) and (4-3) are also shown.
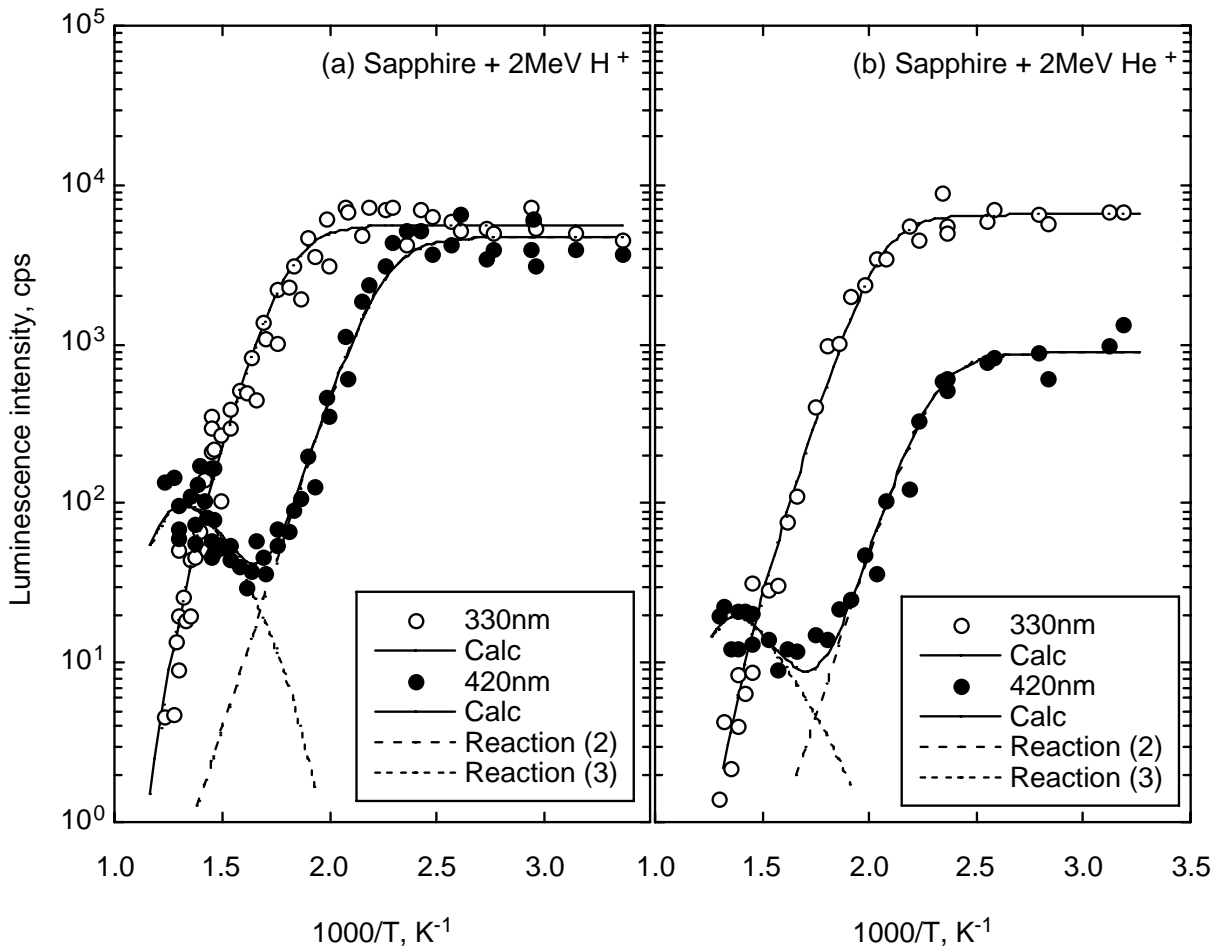
Fig. 4-5.　Arrhenius plots of luminscence intensity of sapphire under (a) 2MeV H^{+} and (b) 2MeV He[+] irradiation.　　The ordinate represents luminescence intensity normalized to the beam current of $10nA/cm^2$.　　Marks are experimental and curves represent the least-squares fits of the data to Eqs. (4-10) and (4-11) as described in 4.3.2.　　Contributions of reactions (4-2) and (4-3) are also shown.
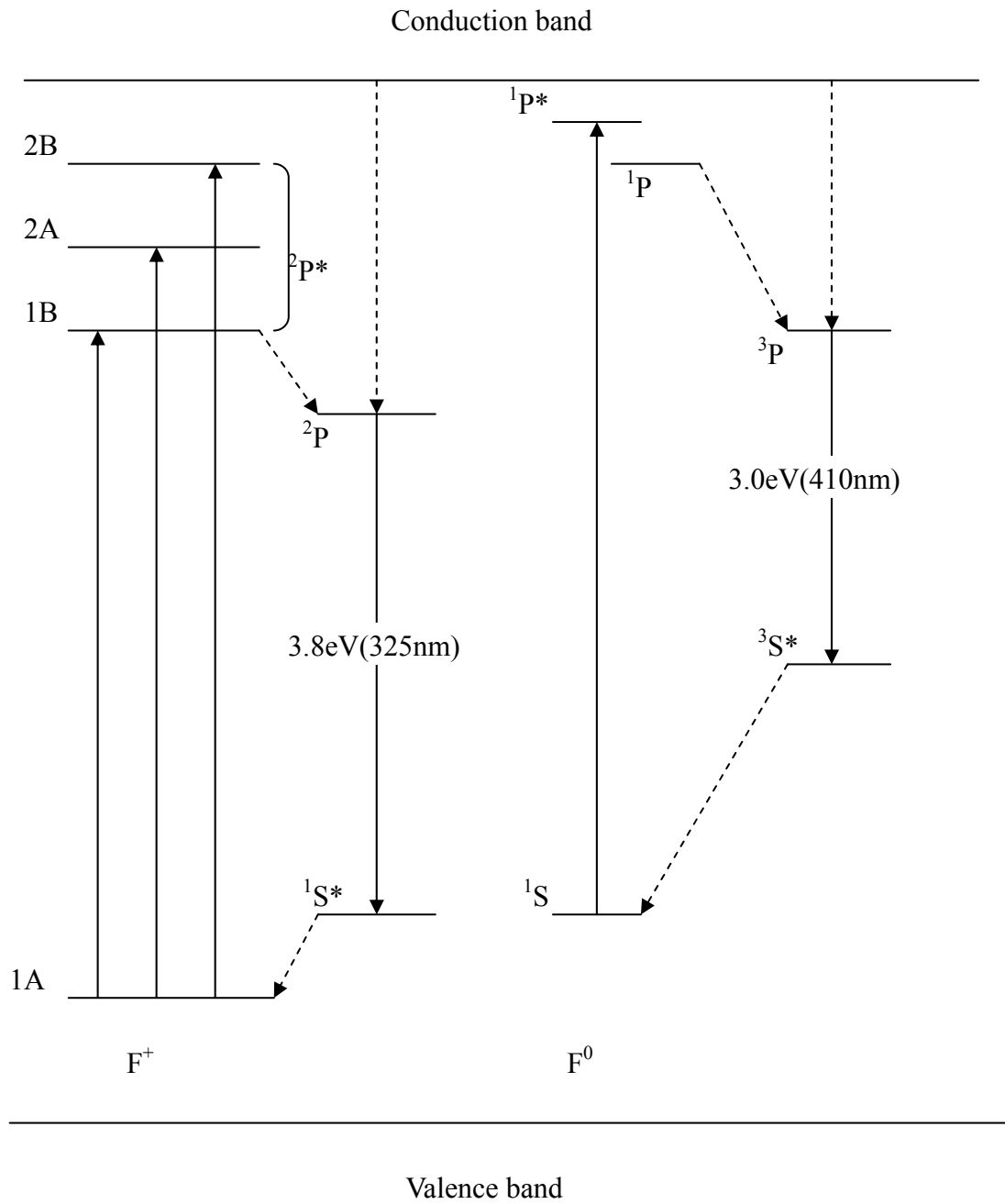
Fig.4-6.Flat-band diagram of α-alumina and sapphire summarizing the relative energy positions of F-type centers [7].
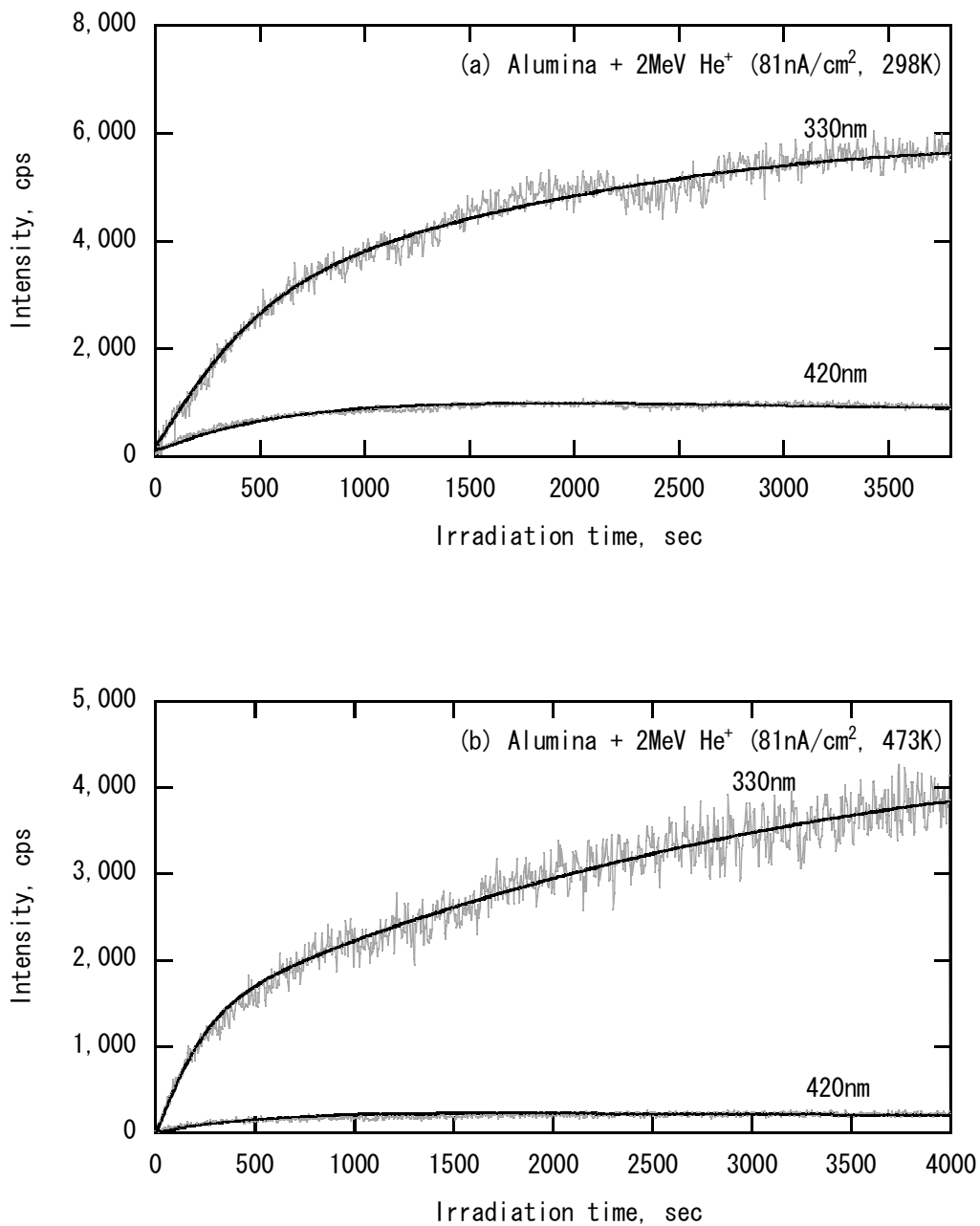
Fig. 4-7. Irradiation time dependence of the luminescence from α-alumina under 2MeV He$^+$ irradiation at (a) 298K and (b) 473K.   The luminescence intensity is given in cps for a fixed window of 0.75nm.   The specimen was annealed above 1073K for 10 minutes.
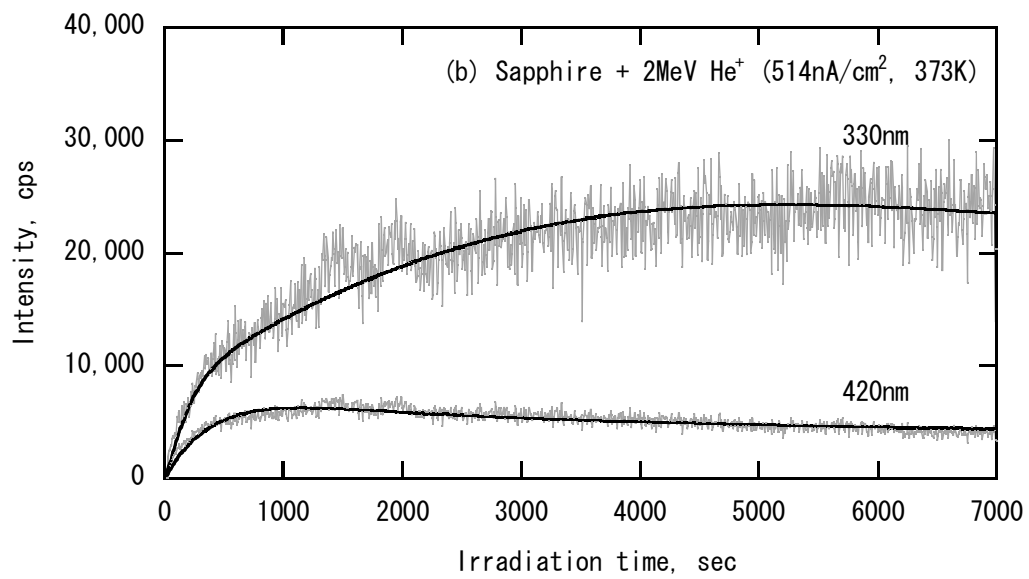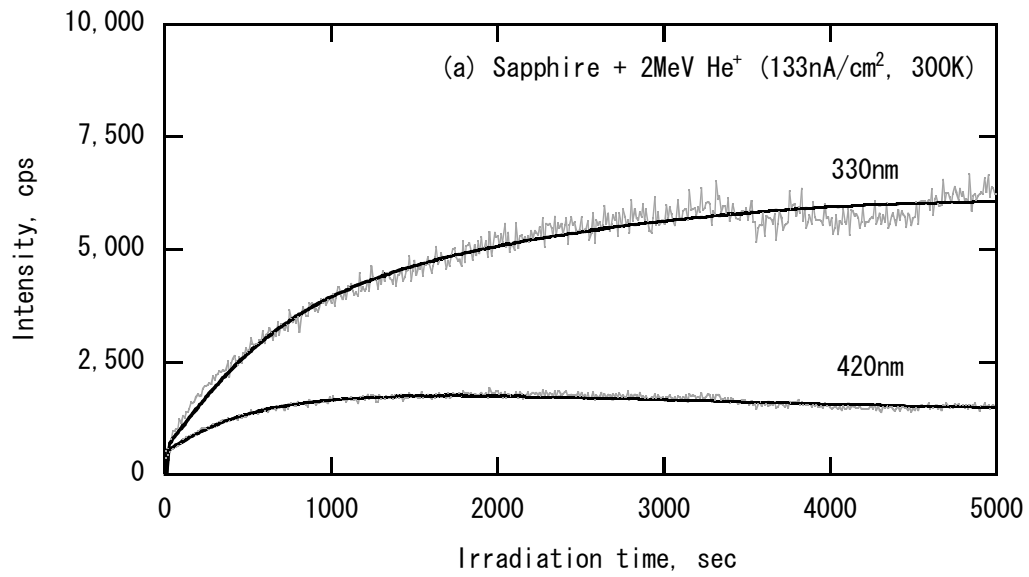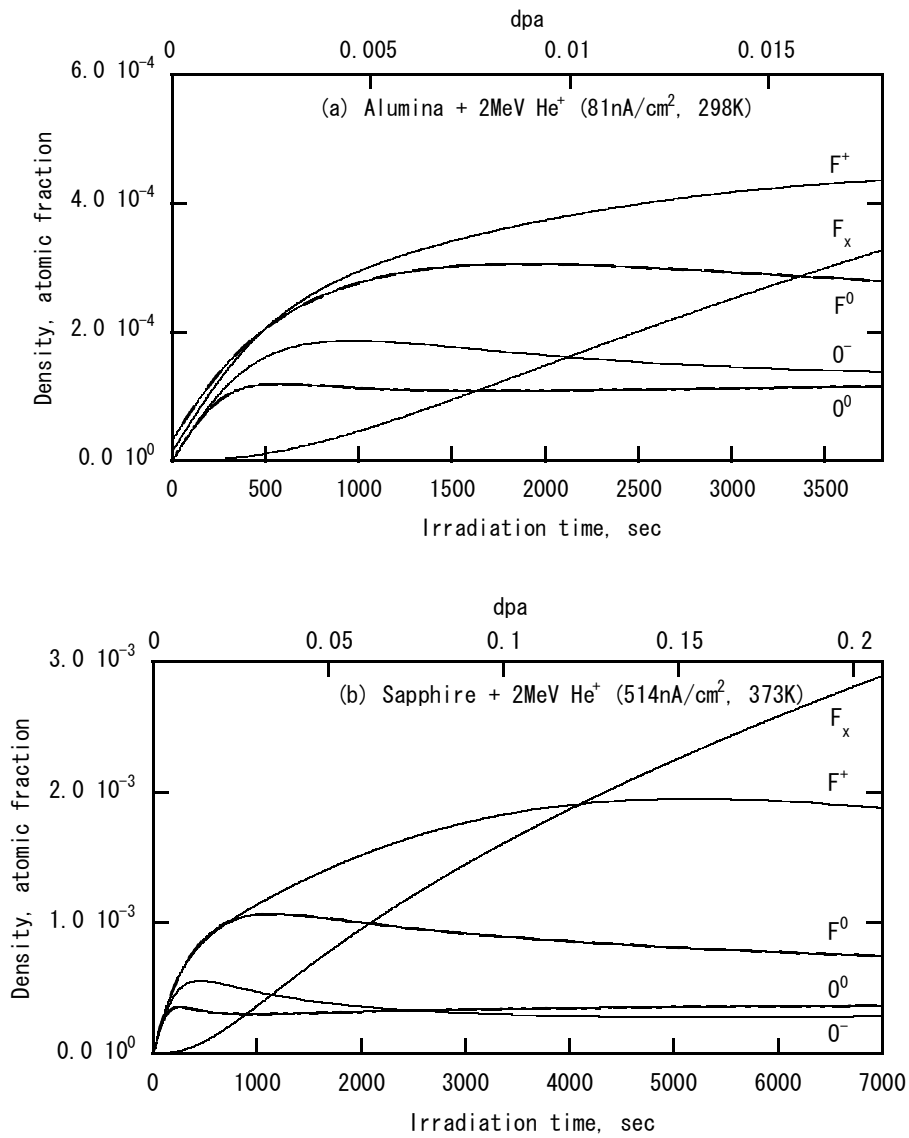
Fig. 4-8.   Irradiation time dependence of the luminescence from sapphire under
2MeV He$^+$ irradiation at (a) 300K and (b) 373K.   The luminescence
intensity is given in cps for a fixed window of 0.75nm.   The specimen
was annealed above 1073K for 10 minutes.

Fig. 4-9.   Accumulation behavior of radiation-induced defects in (a) α-alumina and (b)
sapphire under 2MeV He$^+$ irradiation.   Curves represent the results of
simulation for the observed luminescence in Figs. 4-7(a) and 4-8(b).
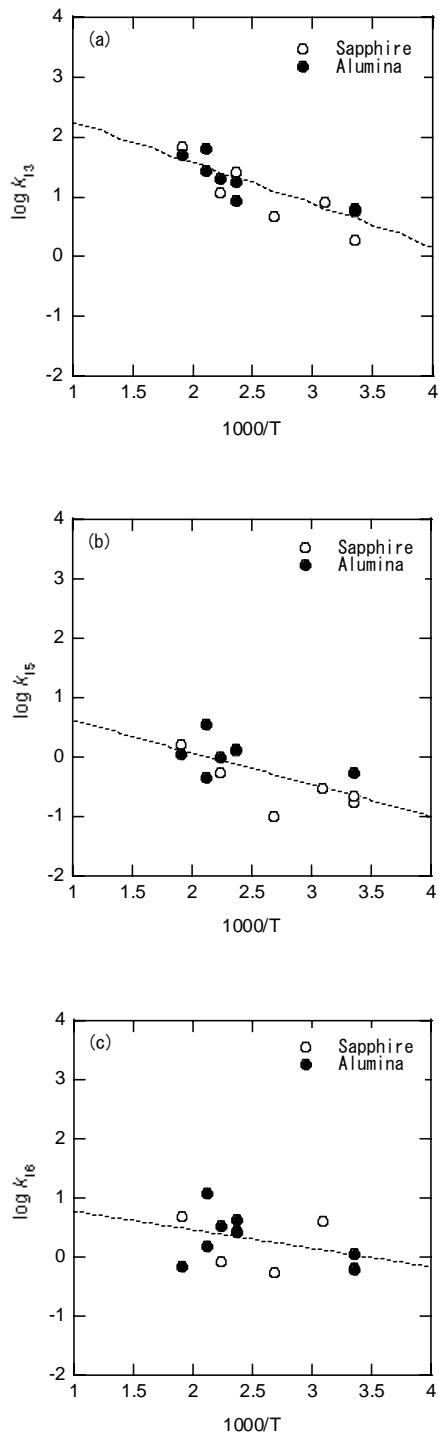
Fig. 4-10. Arrhenius plots of rate constant of (a) k_{13}, (b) k_{15}, and (c) k_{16}. Curves represent the least-squares fitting of the data to the Arrhenius equations.
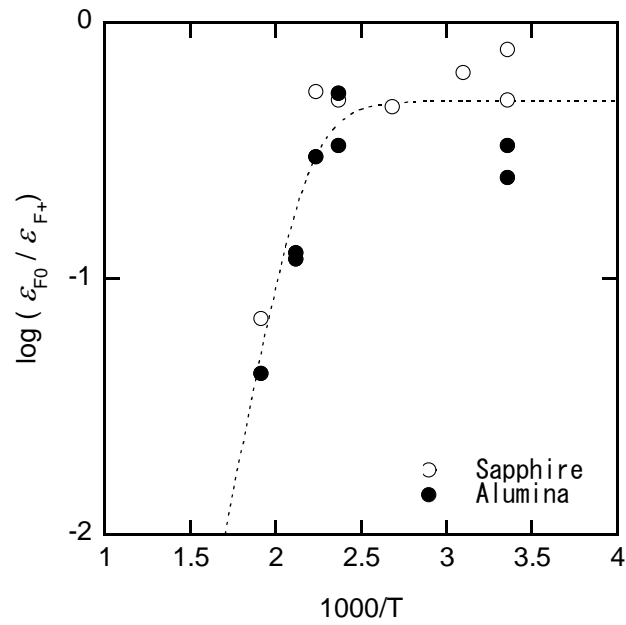
Fig. 4-11. Arrhenius plots of the ratio of the luminescence detection efficiency of the F^0 to that of the F^+.   Curve represents the least-squares fitting of the data to Eq. (4-24).

Chapter 5
Electron spin resonance measurement of irradiation defects in vitreous silica and quarts

5.1 Introduction

Irradiation behavior of ceramic materials is one of the topics of current interest, since some of these materials are to be used in the strong radiation field of proposed fusion reactors. However, the production behavior of irradiation defects under neutron irradiation has not been fully clarified in spite of the considerable progress in understanding many aspects of irradiation defects in these ceramic materials.   It is thus important to know the production behavior of irradiation defects in neutron irradiated ceramic materials.

In the case of vitreous silica, the three fundamental centers of the E' center ($\equiv$Si•), the peroxy radical (POR: $\equiv$Si–O–O•) and the non-bridging oxygen hole center (NBOHC: $\equiv$Si–O•) are known to form the basis of the present understanding of defects in this material [1].   These are all paramagnetic and have been well characterized by the electron spin resonance (ESR) techniques, compared with the diamagnetic oxygen-deficiency centers (ODCs: $\equiv$Si:Si$\equiv$).   In addition, the self-trapped holes (STHs: $\equiv$Si–O–Si$\equiv$) are also known to participate in the radiolysis process in the lower temperature range, and it has been recently suggested that the STHs play an important role even at the ambient temperature under irradiation [2].   Thus, it is needed to take into account all these defects in order to interpret the irradiation behavior of vitreous silica.

In the present study, the electron spin resonance (ESR) measurement of irradiation defects in vitreous silica and quartz was performed to study the effects of neutron and ion beam irradiation on these materials.   The obtained results are analyzed to discuss some details of the reaction mechanism of the irradiation defects.

5.2 Experimental

In the case of neutron irrdaition, vitreous silica (T-1030, T-2030) was obtained from Toshiba Ceramics Co., and weighed samples of 100mg each were irradiated with thermal neutrons at a position of 2.75×10^{13} n•cm^{-2}•sec^{-1} in the Kyoto University Research Reactor (KUR).   The irradiation time ranged from 1 min to 60 min, and neutron fluence ranged from 1.7×10^{15} n•cm^{-2} to 1.0×10^{17} n•cm^{-2}.   Table 5-1 summarizes the samples and irradiation conditions.

In the case of ion beam irradiation, specimens of vitreous silica, T-2030 (1ppm OH) and T-4040 (800ppm OH), and quartz crystal were obtained from Toshiba Ceramics Co., which were of 10 mm in diameter and about 0.5 mm in thickness.   Specimens were irradiated at room temperature with a He$^+$ ion beam, accelerated to 2 MeV with a Van de Graaff accelerator. The range and total number of displacements were estimated to be about 8 μm and 160 displacements/ion, respectively, by using the TRIM code (SRIM-98) with the displacement energies of 20 eV for Si and O.   Also, by considering inhomogeneous defect production and by taking a weighted average value for dpa, a conversion factor of 4.1×10^{20} ions•m^{-2}•dpa^{-1} for

oxygen was obtained for 2 MeV He$^+$ ions.   The size of the ion beam was about 3 mm in diameter and its intensity was monitored.   The ion beam intensity ranged from 6.0x10^{-4} to 1.3x10^{-3} A•m^{-2}, and the dose ranged from 5.0x10^{18} to 2.2x10^{20} ions•m^{-2} (0.012 to 0.54 dpa). As reported previously [2], no apparent effect of the ion beam intensity was observed on each spin density.   A thermocouple was attached to the sample surface to monitor its temperature at a distance close to beam area.   In the irradiation at room temperature, the temperature rise by beam heating was observed to be within a few degrees as estimated by taking the values of thermal diffusion coefficient, density and heat capacity of silica.

After the irradiation, first-derivative ESR spectra were recorded either at room temperature (for the E's) or at 77K (for others) on a JEOL JES-TE200 instrument operating at X-band frequencies (ν~9.26 GHz) with 100-kHz magnetic field modulation. Measurements of the g-values were accomplished by using conventional standard samples of DPPH (diphenylpicrylhyrazyl) and MgO.   Isothermal annealing experiments at 373K, 423K, 473K and 523K were carried out by moving the samples contained in fused quartz sample tubes to an external furnace.   Spin concentrations were determined by resolution of derivative spectra into a number of components, double numerical integration of every component spectra and comparison of the obtained areas with that of a DPPH sample of 1.53x10^{21} spins•g^{-1}.   The accuracy of the numerical integrations was typically of the order of ±5% for the stronger signals in the irradiated samples.   In the case of the weaker signals, these errors were over ±10% due to low signal-to-noise ratios.

5.3 Results and Discussion
5.3.1 Vitreous silica irradiated with neutrons

Fig. 5-1 illustrates a typical ESR spectrum of neutron irradiated vitreous silica of T-1030. As shown in this figure, the resolution of the observed spectra was not completed only by considering the participation of the well-known paramagnetic defect centers of the E', NBOHC and POR, and then some new variants of the O$_2^-$-type defect centers were taken into account.   In the resolution of each spectrum, the initial g-values and peak-to-peak derivative widths of Lorentzian line shapes for the E', NBOHC and POR were taken from the literatures [1] and those of the O$_2^-$-type defect centers were assumed to follow the g-value theory of Känzig and Cohen [3].

According to their theory, the g-values of O$_2^-$ ions in solids are given by the following equations:

$$g_1 = g_e \left(\frac{\Delta^2}{\lambda^2 + \Delta^2} \right)^{1/2} - \frac{\lambda}{E}\left[-\left(\frac{\lambda^2}{\lambda^2 + \Delta^2} \right)^{1/2} - \left(\frac{\Delta^2}{\lambda^2 + \Delta^2} \right)^{1/2} + 1 \right] \tag{5-1}$$

$$g_2 = g_e \left(\frac{\Delta^2}{\lambda^2 + \Delta^2} \right)^{1/2} - \frac{\lambda}{E}\left[\left(\frac{\lambda^2}{\lambda^2 + \Delta^2} \right)^{1/2} - \left(\frac{\Delta^2}{\lambda^2 + \Delta^2} \right)^{1/2} - 1 \right] \tag{5-2}$$

$$g_3 = g_e + 2\left(\frac{\lambda^2}{\lambda^2 + \Delta^2}\right)^{1/2} l \qquad\qquad (5\text{-}3)$$

where g_e is the free-electron g-value (2.00232), λ the spin-orbit coupling constant for the O$^-$ ion, Δ the splitting of the 2p π_g antibonding level, E the separation of the foregoing level from 2p σ_g bonding level (E=5.08eV for O$_2^-$ ions in NaCl [4]), and l is a correction to the orbital angular momentum (l=1 for the free molecular ion).   With a constraint of these equations, a line shape simulation was performed similarly to the case of the literatures [5-7], and a least squares fitting method was applied to the simulation in order to determine the g-values and peak-to-peak derivative widths of the component defects.   The results are summarized in Table 5-2.

The principal-axis g-values for the new variant of the O$_2^-$-type defect centers, which are denoted by X_1 and X_2, are different from those of the well known paramagnetic states of the E's, NBOHCs, and PORs.   These are attributed to some other minor states considering their production behavior.   In fact, the production yield has been observed to saturate with the increasing neutron fluence as shown below.   Thus, the production of these states might be hardly observed in the case of highly irradiated samples [8].

Figs. 5-2 and 5-3 show the neutron fluence dependence of the spin densities in the high OH (T-1030) and low OH (T-2030) samples, respectively.   Although the neutron fluence region is rather limited, it is observed that the spin densities of the E's, NBOHCs, and PORs increase with the increasing neutron fluence while those of the X_1 and X_2 show some saturation behavior.   This means that the X_1 and X_2 are of extrinsic and impurity-related centers.   In fact, the spin densities of these states are higher and become saturated earlier in the high OH (T-1030) samples than in the low OH (T-2030) samples.   Then it may be postulated that these states come from the impurity of OH.   It is also noted that the spin densities of the E' centers are higher in the high OH (T-1030) samples than in the low OH (T-2030) samples.   Some additional production of the E's is thus considered in the higher OH samples.   No apparent difference due to different OH contents is observed for the PORs and NBOHCs.

The production of the E's under irradiation may be expressed simply as

$$(\equiv\text{Si}-\text{O}-\text{Si}\equiv)^* \;\rightarrow\; \equiv\text{Si}\bullet \text{ Si}\equiv + \text{O}^- \qquad\qquad (5\text{-}4)$$

where $(\equiv\text{Si}-\text{O}-\text{Si}\equiv)^*$ denotes an excited state produced by irradiation.   The PORs are to be produced from the E's and O$_2$ molecules by [10]

$$\equiv\text{Si}\bullet \text{ Si}\equiv + \text{O}_2 \;\rightarrow\; \equiv\text{Si}-\text{O}-\text{O}\bullet \text{ Si}\equiv \qquad\qquad (5\text{-}5)$$

Recently, Griscom and Mizuguchi [2] have pointed out that reaction (5-5) hardly occurs at lower temperatures since the activation energy (E=1.17eV [9]) for the O$_2$ diffusion is rather

high.   By considering this and by considering possible break up of the O_2 molecules by neutron irradiation [11], they have suggested the following reactions for the production of the NBOHCs and PORs at lower temperatures.

$$\equiv Si\bullet\ Si\equiv + O^0\ \rightarrow\ \equiv Si-O\bullet\ Si\equiv \tag{5-6}$$

$$\equiv Si-O\bullet\ Si\equiv\ + O^0\ \rightarrow\ \equiv Si-O-O\bullet\ Si\equiv \tag{5-7}$$

The O^0s are also produced by irradiation together with the diamagnetic ODCs [12] as

$$(\equiv Si-O-Si\equiv)^*\ \rightarrow\ \equiv Si:\ Si\equiv + O^0 \tag{5-8}$$

Thus the observed neutron fluence dependence of the spin densities of the E's, NBOHCs, and PORs may be explained by considering these reactions, although it is needed to take into account the participation of the X_1s and X_2s in the reaction mechanisms.

    For the presently observed X_1 and X_2 states, the following reactions can be suggested by considering that these states are produced with the E's from the impurity OH and by assuming that the O^-s are as mobile as the O^0s.

$$\equiv Si-OH + O^-\ \rightarrow\ \equiv Si\bullet + O_2^- + H^0 \tag{5-9}$$

and/or

$$\equiv Si-OH + O^0 + e^-\ \rightarrow\ \equiv Si\bullet + O_2^- + H^0 \tag{5-10}$$

The e^-s in reaction (5-10) may be supplied from such reactions under irradiation as

$$(\equiv Si-O-Si\equiv)^*\ \rightarrow\ \equiv Si-O\bullet\ Si\equiv\ + e^- \tag{5-11}$$

$$(\equiv Si-O-Si\equiv)^*\ \rightarrow\ \equiv Si-\overset{\bullet}{O}-Si\equiv + e^- \tag{5-12}$$

Considering these reactions, it is explained that the spin densities of the E's, X_1s and X_2s are sensitive to the OH content of the sample especially in the lower fluence region, increasing with the increasing OH content.   When the spin density of the E's increases, it is expected that reactions (5-6) and (5-7) occur and that the secondary production of the NBOHCs and PORs occur.   However, such effects on the spin densities of the NBOHCs and PORs are hardly observed in the present case.   This is possibly because the density of the O^0s is decreased by such reactions as reaction (5-10).

    Figs. 5-4 and 5-5 show the results of the isochronal anneal of high OH (T-1030) and low OH (T-2030) samples, respectively.   The observed anneal behaviors are well explained by considering the above mentioned reactions.   For example, the spin densities of the E's rapidly decrease below 473K (200°C) possibly due to their recombination with the mobile O^-s. Although the recombination is not completed below that temperature, the remaining E's may recombine with the O_2^-s at higher temperatures at which the O_2^-s are expected to be as mobile as the O_2s.

Above 473K (200˚C), the O_2s and O_2^-s become mobile, and their reactions start to occur. The spin densities of the X_1s and X_2s thus decrease with the increasing temperature in this range. The NBOHCs also decrease, for example, as

$$\equiv Si-O\bullet Si\equiv \ + O_2^- \ \rightarrow \ \equiv Si-O-Si\equiv \ \ + O_2 \qquad\qquad (5\text{-}13)$$

As shown in Figs. 5-4 and 5-5, the reactions of the PORs are much different in different OH content samples. In the case of the low OH (T-2030) samples, the spin densities of the PORs increase with the increasing temperature up to 723K (450˚C). This means reaction (5-5) occurs and a definite amount of the O_2s remains in this case. In the case of the high OH (T-1030) samples, on the other hand, reaction (5-10) hardly occurs. Because of reactions (5-9) and/or (5-10), not the O_2s but O_2^-s are considered to remain predominantly in this case.

5.3.2. Vitreous silica irradiated with ion beams

Fig. 5-6 shows a typical ESR spectrum of ion beam irradiated vitreous silica of T-2030. As shown in this figure, the resolution of the observed spectra was well completed by only considering the participation of the well-known paramagnetic defect centers of the E', NBOHC and POR. Such new variants of the O_2^--type defect centers as observed in neutron irradiated specimens were not observed. The production of these states might be difficult to observe in the present case of rather high dpa values as discussed below.

Contrary to the present study using 2 MeV He$^+$ ions, Miyamaru et al. have observed the ESR signal of g=2.0025 is much higher than that of the E' in their study using 20 keV D$^+$ and He$^+$ ions [13]. By considering different incident energies, it may be postulated that they have observed the defect species produced near surface. According to Stesmans and Sceerlinck [14], in fact, the so called EX centers with g=2.0025 are produced around surface.

Fig. 5-7 shows the ion beam intensity dependence of the spin densities of the E's, NBOHCs, and PORs. Although the intensity ranges from 4.5×10^{-4} to 4.5×10^{-3} A/m^2, no apparent effect is observed on each spin density. As shown below, a cascade overlap effect is inferred from the ion beam fluence dependence, but there is almost no effect of the ion beam intensity in the studied range.

Fig.5-8 shows the effects of ion beam fluence on the spin densities of the E's, NBOHCs, and PORs. For comparison, the results of neutron irradiation are also shown in the figure as a function of the dpa value. A conversion factor of 1 dpa = 1.8×10^{24} n/m^2 for oxygen is obtained for fast neutrons following the manner in the literature [15,16], while the dpa values of ion beam irradiation are evaluated by using the TRIM code (SRIM-98). In the latter case, by considering inhomogeneous defect production and by taking a weighted average value for dpa, a conversion factor of 4.4×10^{20} ions/m^2 for oxygen is obtained for 2 MeV He$^+$ ions. In Fig. 5-8, it is seen that the dpa values of the present ion beam irradiation are much higher than those of neutron irradiation. In such a case, the contribution of the impurity (OH) related defect centers may be negligible. This is the reason why such variants of the O_2^--type

defect centers as observed in neutron irradiated specimens are not observed in the present case.

As shown in Fig. 5-8, the spin densities of the E's, NBOHCs, and PORs increase with the increasing dpa value. Above the dpa value of 10^{-2}, however, all the spin densities become saturated. Cascade overlaps are considered to be responsible for this saturation behavior, and defect clusters are produced in this region. As for the production efficiency of the defect centers, it is noted that the spin densities of the E's are rather close to the evaluated concentration of the displaced oxygen atoms, especially in the case of ion beam irradiation. This means the production efficiency of the E's is considerably high. Not only the nuclear stopping but also the electronic stopping power may be considered to take part in such a high production efficiency in this case.

Among the other defects, it may be remembered that diamagnetic oxygen-deficiency centers such as ODCs are also produced in vitreous silica. In fact, the production of the ODCs has been observed by an in-situ luminescence measurement of vitreous silica in our previous study [12]. It is thus interesting to compare the production efficiencies of all these defects, and a comparison will be given below.

In the case of neutron irradiated vitreous silica, a production and reaction mechanism has been used to explain the obtained results. The same mechanism is applied to the results of ion beam irradiation. Although some variants of the O_2^--type defect centers (X_1s and X_2s [17]) are also involved in the mechanisms at lower dpa values, the observed dpa dependence of the spin densities of the E's, NBOHCs, and PORs in Fig. 5-8 are well explained by considering these reactions.

Fig. 5-9 shows the results of the isochronal anneal of vitreous silica (T-2030) irradiated by 2 MeV He$^+$ ions to a dose of 1.5×10^{19} ions/m^2. The observed annealing behavior is well explained by considering the above reactions. For example, the spin densities of the E's rapidly decrease with the increasing temperature up to 473K (200°C) possibly due to their recombination with the O$^-$s which are adjacent to the E's. The recombination is not completed below 473K, but the remaining E's may recombine with the O$^-$s which are apart from the E's, at high temperatures at which such O$^-$s are expected to be mobile.

As for the others, it may be noted that the NBOHCs decreases and the PORs increase with the increasing temperature in a rather lower temperature region. As pointed out by Griscom and Mizuguchi [2], reactions (5-6) and (5-7) are considered to be responsible for this behavior, since reaction (5-5) hardly occurs at lower temperatures. No apparent increase of the PORs is observed at higher temperatures above 573K (300°C), and almost no contribution of reaction (5-5) is inferred from the present results.

As mentioned above, it is interesting to evaluate the densities of such diamagnetic ODCs from the present results. For the O^{0}s which are produced together with the ODCs by reaction (5-8), it may be assumed that its density will be relatively small because of its high mobility. By considering the above reaction scheme and mass balance, the densities of the ODCs and O$^-$s are thus given by

$N_{ODC} = N_{NBOHC} + 2N_{POR}$ (5-14)

$N_{O^-} = N_{E'} + N_{NBOHC} + N_{POR}$ (5-15)

where N denotes the density.   Together with the ODCs, the O^0s are produced by reaction (5-8) and are used to produce the NBOHCs and the PORs by reactions (5-6) and (5-7). Then Eq. (5-14) is obtained by considering that one NBOHC corresponds to one O^0 and one POR two O^0s.   Eq. (5-15) is also obtained similarly by considering reactions (5-4), (5-6) and (5-7).

The densities of the ODCs and O^-s are evaluated from the present results by using eqs. (5-14) and (5-15), as shown in Fig. 5-9.   It is natural that the density of the O^-s is almost the same as those of the E's.   As for the ODCs, it is recognized that the density of the ODCs is much lower than that of the E's.   The production efficiency of the ODCs is not so high as that of the E's in vitreous silica.

5.3.3. Quartz crystal

In the case of ion beam irradiation, the observed spectrum was rather simple as shown in Figs. 5-10(a) to 5-10(d).   Its resolution was well completed by only considering the participation of the well-known paramagnetic defect centers of the E's and PORs, though another signal of amorphous silicon centers ($\bullet Si \equiv Si_3$) with g=2.004 [18] becomes observed in the specimens annealed above 773K (500˚C).   Contrary to the case of vitreous silica, no apparent participation of the NBOHCs centers was observed in this case.   This is one of the differences between quartz crystal and vitreous silica.

As shown in Fig. 5-10(e), a very complicated spectrum was observed in the case of neutron irradiation.   For the lack of information on such a complicated spectrum, no resolution was performed in the present study, and double numerical integration was directly applied to the observed spectra except for some cases in which the participation of the E's and PORs was successfully distinguished from the others.   Because of their production efficiencies and isochronal anneal behavior as given below, the observed complicated components may be attributed to some variants of the O_2^-s similarly to the case of vitreous silica.

As shown in Fig. 5-8, the spin densities of the defects including the E's and PORs in quartz crystal increase with the increasing dpa value, except for the O_2^-s in the lower dpa region.   Above the dpa value of 10^{-2}, however, all the spin densities show some saturation behaviors.   Displacement cascade overlaps are considered to be responsible for this saturation behavior, and defect clusters are produced in this region.   By comparing the results of quartz crystal with those of vitreous silica, it is seen that the production efficiency of the E's in quartz crystal is much lower than that in vitreous silica.   This is one of the most important differences between quartz crystal and vitreous silica.   A similar difference is also found for the PORs.   As for the others, which are of the complicated components mentioned above, no apparent dpa dependence of the spin densities is observed similarly to the O_2^-s in vitreous silica.   This may suggest that those are mostly of some variants of the
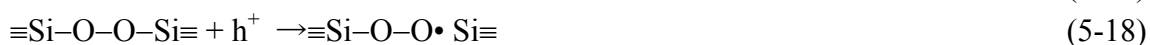
O_2^-s.

A production and reaction mechanism of the defects in vitreous silica has been discussed in 5.3.1. In the case of quartz crystal, however, the production of the E's is considerably low compared with the case of vitreous silica and no apparent production of the NBOHCs is observed. This suggests another mechanism in quartz crystal. In fact, the density of quartz crystal is much higher than that of vitreous silica, and the above mechanism in vitreous silica, which is much dependent on the mobility of such O^0s, may not be so important in quartz crystal.

The present observations in quartz crystal are well explained by a model of Hobbs and Pascucci [19]. According to them, a sufficiently localized excitation leads to severing of an Si-O bond, followed by removal of the oxygen atom previously linking two Si atoms to form a ODC and incorporation of the resulting non-bridging oxygen atom into an Si-O-O-Si peroxy linkage, as
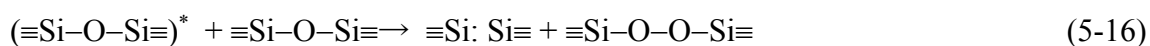
$$(\equiv Si-O-Si\equiv)^* + \equiv Si-O-Si\equiv \rightarrow \ \equiv Si: Si\equiv + \equiv Si-O-O-Si\equiv \qquad (5\text{-}16)$$

The oxygen vacancy and peroxy linkage, which form the components of a close Frenkel pair, are transformed to a E' and a POR, respectively, by subsequent hole trapping as

$$\equiv Si: Si\equiv + h^+ \rightarrow \equiv Si\bullet\ Si\equiv \qquad (5\text{-}17)$$
$$\equiv Si-O-O-Si\equiv + h^+ \rightarrow \equiv Si-O-O\bullet\ Si\equiv \qquad (5\text{-}18)$$

The E's and PORs are thus produced. No production of the NBOHCs is considered in this case, being consistent with the present observations.

Fig. 5-11 shows the results of the isochronal annealing of quartz crystal irradiated by 2 MeV He$^+$ ions to a dose of 6.5×10^{19} ions/m^2. The observed annealing behavior is also well explained by considering the above reactions. For example, the spin densities of the E's and the PORs rapidly decrease above 473K (200°C) possibly due to their recombination with each other. The E's and PORs are produced by reactions (5-17) and (5-18), respectively, in which the ODCs and peroxy linkages are the components of the close Frenkel pairs, and are likely to recombine at these temperatures.

Another type of the defects appears in the spectra of the specimens annealed above 773K (500°C). The observed g-value of 2.004 is very close to that of amorphous silicon centers [18], which are produced in the thermal Si/SiO$_2$ structure. For example, it has been reported that the degradation of the thermal Si/SiO$_2$ structure is identified as such defects creation above 640°C [20]. By comparing the temperatures, it may be considered that, in the present annealed specimens, some of holes are released from the recombination reactions of the E's and PORs to enhance the production of the amorphous silicon centers.

5.4.5 Isothermal anneal behavior of spin densities in vitreous silica

Fig. 5-12 shows the effects of ion beam fluence on the spin densities of the E's,

NBOHCs, and PORs.   It is seen that the spin densities of the E's, NBOHCs, and PORs increase with increasing dpa value.   Above the dpa value of 10^{-2}, however, all the spin densities become saturated.   As already mentioned, cascade overlaps are considered to be responsible for this saturation behavior, and defect clusters may be produced in this region. The observed saturation behaviors of the E's, NBOHCs, and PORs are discussed later by taking into account the reaction rate constants which are determined below.

Fig. 5-13 shows the results obtained from the isothermal annealing experiments with T-2030 irradiated by 2 MeV He$^+$ ions.   As seen in this figure, the spin densities of the E's and NBOHCs decrease and those of the PORs increase with the annealing time.   Similar results were also obtained for T-4040.   It is important to note that the total spin densities of the E's, NBOHCs and PORs are not changed but almost constant during each annealing experiment.   This fact strongly suggests that the E's and NBOHCs are converted to the PORs by annealing as [2]:

$$\text{E}' + \text{O} \;\rightarrow\; \text{NBOHC} , \tag{5–19}$$
$$\text{NBOHC} + \text{O} \;\rightarrow\; \text{POR} . \tag{5–20}$$

Since the total spin densities are almost constant, reactions other than (5-19) and (5-20) are considered to be less important in the present experiments.   The present observations are then analyzed by taking reactions (5-19) and (5-20).   In this case, the variations of the spin densities of the E's, NBOHCs and PORs with annealing time are calculated by solving the following equations:

$$\text{d[E']}/\text{d}t = -\,k_1[\text{E'}][\text{O}] , \tag{5-21}$$
$$\text{d[NBOHC]}/\text{d}t = k_1[\text{E'}][\text{O}] - k_2[\text{NBOHC}][\text{O}] , \tag{5-22}$$
$$\text{d[POR]}/\text{d}t = k_2[\text{NBOHC}][\text{O}] , \tag{5-23}$$

where k_1 and k_2 are the rate constants of reactions (5-19) and (5-20), respectively.   The values of the rate constants are given in atomic fraction in the present study.   Eqs. (5-21) to (5-23) are solved by the Runge-Kutta method to obtain the densities of the E's, NBOHCs and PORs, and the rate constants k_1 and k_2 are determined together with the initial density of the Os which is treated as another free parameter.   In some trials in the present analysis, possible reactions of the Os such as $\text{O} + \text{O} \rightarrow \text{O}_2$ are taken into account together with reactions (5-19) and (5-20), but no improvement is obtained in the fitting results.   It is confirmed that reactions (5-19) and (5-20) are enough to explain the observations.

As shown in Fig. 5-13, in which the calculated isothermal annealing behaviors are compared with the observations, good agreements are obtained in all the cases.   The initial density of the Os is obtained to be 5×10^{-4}, 1×10^{-3} and 9×10^{-4} in atomic fraction in the specimens of Figs. 5-13(a), (b) and (c), respectively.   The values are acceptable considering the possible scatters due to different specimens, similarly to the case of the E's, PORs and NBOHCs in Fig. 5-12.   For the formation of the Os, it may be remembered that the Os are

likely formed with the ODCs by ion beam irradiation [12].

Figs. 5-14(a) and (b) show the Arrhenius plots of the rate constants (k_1 and k_2) obtained for T-2030 and T-4040, respectively.   As summarized in Table 5-3, the Arrhenius equations of the rate constants are obtained by the least-squares fitting, and the activation energies are obtained to be about 0.40eV for every reaction of the Os in both specimen.   Also, only slight differences are found for the pre-exponential term which is possibly due to different specimens.   From the present results, it may be concluded that the activation energy for reactions of the Os in vitreous silica is about 0.40eV and that no apparent difference is found due to the OH content in the specimen.

According to the literature [21], oxygen is generally considered to diffuse as the molecular O_2, and activation energies are given in the range of 1.17 to 1.35eV by gas transport experiments, which are much higher than the present value for the O.   In his calculation study [22], Hamann found the peroxy linkage as the lowest energy configuration of an atomic O in α-SiO_2, and proposed its diffusion with the peroxy exchange barrier of 1.3eV.   This value, which is not for vitreous SiO_2 but for crystalline SiO_2, is still high similarly to the O_2.   For oxygen ions of O^- and O^{2-}, on the other hand, Jin and Chang suggested that a double Si-O-Si bridge structure is the lowest energy configuration of those ions, and reported extremely low energy barriers of 0.11-0.27eV in this case [23].   Also, Roma et al. considered such interactions as those of hydrogen impurities with the Os, although no conclusion was obtained for the consequences on oxygen diffusion [24].   In view of these various possibilities, further confirmation and consideration may be needed for details of the oxygen diffusion mechanism itself.

It is interesting and important to note that the present reaction scheme and obtained rate constants are consistent with the observed saturation behaviors of the E's, NBOHCs and PORs, as shown in Fig. 5-12.   In this case, the saturation behavior of the E's, NBOHCs and PORs are calculated by taking the following equations:

$$d[\text{E'}]/dt = g_{\text{E'}}(\phi/c) - k_1[\text{E'}][\text{O}] - k'_{\text{E'}}(\phi/c)[\text{E'}] \ , \qquad\qquad (5\text{-}24)$$
$$d[\text{NBOHC}]/dt = g_{\text{NBOHC}}(\phi/c) + k_1[\text{E'}][\text{O}] - k_2[\text{NBOHC}][\text{O}] - k'_{\text{NBOHC}}(\phi/c)[\text{NBOHC}] \ , \quad (5\text{-}25)$$
$$d[\text{POR}]/dt = g_{\text{POR}}(\phi/c) + k_2[\text{NBOHC}][\text{O}] - k'_{\text{POR}}(\phi/c)[\text{POR}] \ , \qquad\qquad (5\text{-}26)$$
$$d[\text{O}]/dt = g_{\text{O}}(\phi/c) - k_1[\text{E'}][\text{O}] - k_2[\text{NBOHC}][\text{O}] - k'_{\text{O}}(\phi/c)[\text{O}] \ , \qquad\qquad (5\text{-}27)$$

where $g_{\text{E'}}$, g_{NBOHC}, g_{POR} and g_{O} represent the production rates (atomic fraction$\cdot$dpa^{-1}) of the E's, NBOHCs, PORs and Os by ion beam irradiation, respectively, ϕ the ion beam intensity (ions$\cdot$m$^{-2}\cdot$s^{-1}), c the conversion factor (4.1×10^{20} ions$\cdot$m$^{-2}\cdot$dpa^{-1}), and k' the reaction rate constant (dpa^{-1}) of each defect by cascade overlaps.   The k_1 and k_2 values are obtained from the present results in Fig. 5-13.   For the fits of the data to Eqs (6) to (9), the $g_{\text{E'}}$, g_{NBOHC}, g_{POR} and g_{O} values are obtained to be 0.12, 0.02, 0.05, and 0.12, respectively, and the k' is obtained, as summarized in Table 5-4.

The calculated saturation behaviors agree well with the observed ones, as shown in Fig. 5-12.   No apparent contribution of reactions (5-19) and (5-20) is found in the observed

results because of the smaller k_1 and k_2 values at the irradiation temperature of 298K. It is thus recognized that the saturation behaviors are mainly due to the reactions of each defect by cascade overlaps above the dpa value of 10^{-2}. The reactions with the rate constant k' may include not only the recombination of each defect with the newly formed ones but also the transformation to the higher order defects such as oxygen molecules and multivacancies, and there may be various types of defects in this dpa region. Considering that the contribution of reactions (5-19) and (5-20) will increase with increasing temperature, it is suggested to measure the saturation behaviors at the higher temperatures and the formation of the higher order defects in further studies.

5.5 Conclusions

In the case of neutron irradiation of vitreous silica, some new states were observed in the ESR spectra together with the usual paramagnetic states of the E' centers, non-bridging oxygen hole centers (NBOHCs), and peroxy radicals (PORs). The principal-axis g-values of the new states were obtained from the analysis, and were found to be typical of O_2^- ions in solids. Considering these defects, the observed effects of the OH content, neutron fluence, and postirradiation isochronal anneal behaviors were well explained.

The spin densities of the E's, NBOHCs, and PORs were measured in the ion beam irradiated specimens and compared with the results of neutron irradiation. Both results were well explained by considering the dpa values of irradiation. It was found that the production efficiency of the E's is considerably high. Based on the proposed production and reaction mechanism, the densities of such diamagnetic ODCs were also evaluated from the present results. It was found that the production efficiency of the ODCs is not so high as that of the E's.

For comparison, the production behavior of irradiation defects in quartz crystal was studied. By comparing the obtained results with those of vitreous silica, some different production behaviors were observed. The production efficiency of the E's in quartz crystal was much lower than that in vitreous silica. Also no apparent production was observed in quartz crystal. The observed differences are explained by considering different densities of specimens. Because of much higher density of quartz crystal, the mechanism in vitreous silica, which is much dependent on the mobility of such O^0s, may not be so important in quartz crystal. In quartz crystal, the oxygen vacancy and peroxy linkage, which form the components of a close Frenkel pair, are produced and play an important role under irradiation.

The saturation behaviors of radiation-induced defects in vitreous silica were studied. The spin densities of the E's, NBOHCs, and PORs were observed to saturate above the dpa value of 10^{-2}. In isothermal annealing experiments, the sequential reactions of the E' centers with oxygen atoms to form the NBOHCs and PORs were observed to occur, and the rate constants of those reactions were determined. The activation energies were obtained to be about 0.4eV for those reactions. The proposed reaction scheme and obtained rate constants were shown to be consistent with the observed saturation behaviors of radiation-induced defects in vitreous silica.

References

[1] L. Skuja, J. Non-Cryst. Solids. 239 (1998) 16.

[2] D. L. Griscom, M. Mizuguchi, J. Non-Cryst. Solids. 239 (1998) 66.

[3] W. Känzig, M. H. Cohen, Phys. Rev. Lett. 3 (1959) 509.

[4] J. Rolfe, J. Chem. Phys. 70 (1979) 2463.

[5] P. C. Taylor, P. J. Bray, J. Magn. Res. 2 (1970) 305.

[6] R. A. B. Devine, Phys. Rev. 35 (1987) 9783.

[7] D. L. Griscom, J. Non-Cryst. Solids 149 (1992) 137.

[8] T. Tabata, M. Hasegawa, M. Fujinami, Y. Ito, H. Sunaga, S. Okada, S. Yamaguchi, J. Mucl. Mater. 239 (1996) 228.

[9] F. J. Norton, Nature 191 (1961) 701.

[10] L. Skuja, Güttler, Phys. Rev. Lett. 77 (1997) 2093. A. H. Edwards, W. B. Fowler, Phys. Rev. B26 (1982) 6649.

[11] L. Skuja, Güttler, Phys. Rev. Lett. 77 (1997) 2093.

[12] K. Moritani, I. Takagi, H. Moriyama, J. Nucl. Mater. 312 (2003) 97.

[13] H. Miyamaru, T. Tanabe, T. Iida, A. Takahashi, Nucl. Instr. Methods B 116 (1996) 393.

[14] A. Stesmans, F. Scheerlinck, J. Appl. Phys. 76 (1994) 1047.

[15] M. Hasegawa, M. Saneyasu, M. Tabata, Z. Tang, Y. Nagai, T.Chiba, Y. Ito, Nucl. Instr. Methods B 166-167 (2000) 431.

[16] C. H. de Novion, A. Barbu, Solid State Phenom. 30&31 (1993) 277.

[17] A. H. Edwards, W. B. Fowler, Phys. Rev. B26 (1982) 6649.

[18] Y. Wu, A. Stesmans, Phys. Rev. B38 (1988) 2779.

[19] L. W. Hobbs, M. R. Pascucci, J. de Phyque, Colloque C6 (1980) 237.

[20] A. Stesmans, V. V. Afanas'ev, Phys. Rev. B54 (1996) R11129.

[21] M. A. Lamkin, F. L. Riley, R. J. Fordham, J. Eur. Ceramic Soc. 10 (1992) 347.

[22] D. R. Hamann, Phys. Rev. Lett. 81 (1998) 3447.

[23] Y. –G. Jin, K. J. Chang, Phys. Rev. Lett. 86 (2001) 1793.

[24] G. Roma, Y. Limoge, L. Martin-Samos, Nucl. Instr. and Meth. in Phys. Res. B 250 (2006) 54.

Table 5-1. Sample and irradiation conditions.

Specimen	OH (ppm)	Irradiation condition	
		Irradiation time (min)	Neutron fluence (n•cm^{-2})
T-1030	200	1-60	1.7×10^{15}-1.0×10^{17}
T-2030	1	1-60	1.7×10^{15}-1.0×10^{17}

Table 5-2. g-values and peak-to-peak derivative widths determined in the present analysis*.

Defects	g-value			peak-to-peak derivative width		
	g_1	g_2	g_3	σ_1	σ_2	σ_3
E'	2.0003	2.0005	2.0017	0.05	0.05	0.05
POR	2.002	2.007	2.067	0.2	0.16	1
NBOHC	2.001	2.010	2.08	0.2	0.18	3
X_1	1.996	2.015	2.17	0.2	0.36	4
X_2	1.992	2.021	2.22	0.3	0.38	4

*The λ and Δ values in eqs. (1) to (3) were obtained to be $\lambda = 0.0527$ eV and $\Delta = 0.622$ eV for the X_1s and $\lambda = 0.0827$ eV and $\Delta = 0.752$ eV for the X_2s by employing $l = 1$ and $E = 5.08$eV [4].

Table 5-3.   Reaction rate constants obtained from the analysis of isothermal annealing data.

| Specimen | Rate constants | $k_i = A_i \exp[-E_i/kT]$ | |
		A_i (atomic fraction$^{-1} \cdot$s^{-1})	E_i (eV)
T-2030	k_1	$10^{5.0 \pm 0.7}$	0.40 ± 0.06
	k_2	$10^{5.6 \pm 0.3}$	0.39 ± 0.02
T-4040	k_1	$10^{4.8 \pm 0.2}$	0.40 ± 0.02
	k_2	$10^{5.0 \pm 0.3}$	0.38 ± 0.02

Table 5-4.   Parameter values for defect production and reactions by cascade overlaps.

Defect	g (atomic fraction$\cdot$dpa^{-1})	k' (dpa^{-1})
E'	0.12	$10^{2.4}$
POR	0.05	$10^{1.9}$
NBOHC	0.02	$10^{1.8}$
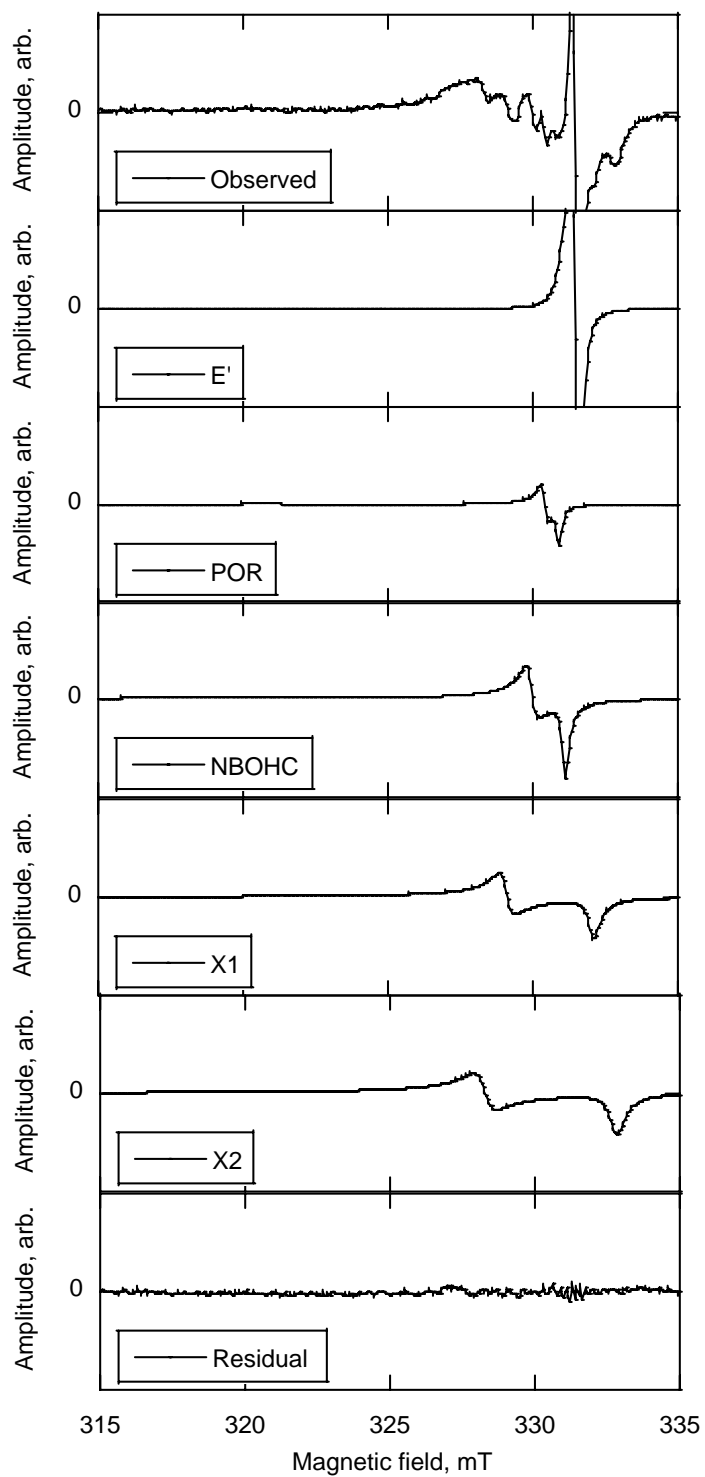
Fig. 5-1. Typical X-band ESR spectrum of the neutron-irradiated high OH (T-2030) silica and its components: (a) observed spectrum(1.6×10^{16} n•cm^{-2}), (b) E', (c) POR, (d) NBOHC, (e) X_1, (f) X_2.
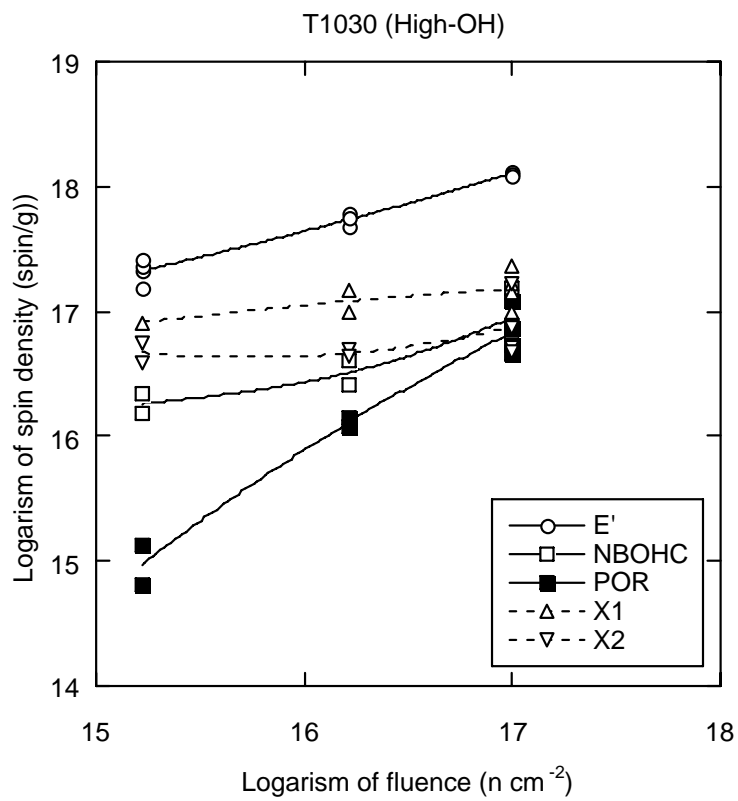
Fig. 5-2. Neutron fluence dependence of spin densities in the neutron-irradiated high OH (T-1030) silica.
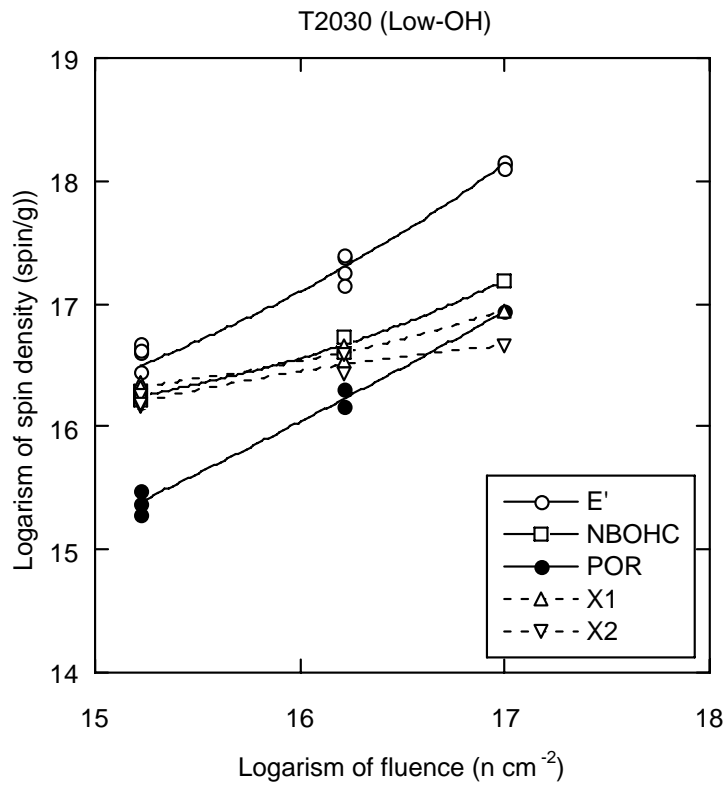
Fig. 5-3.   Neutron fluence dependence of spin densities in the neutron-irradiated low OH (T-2030) silica.
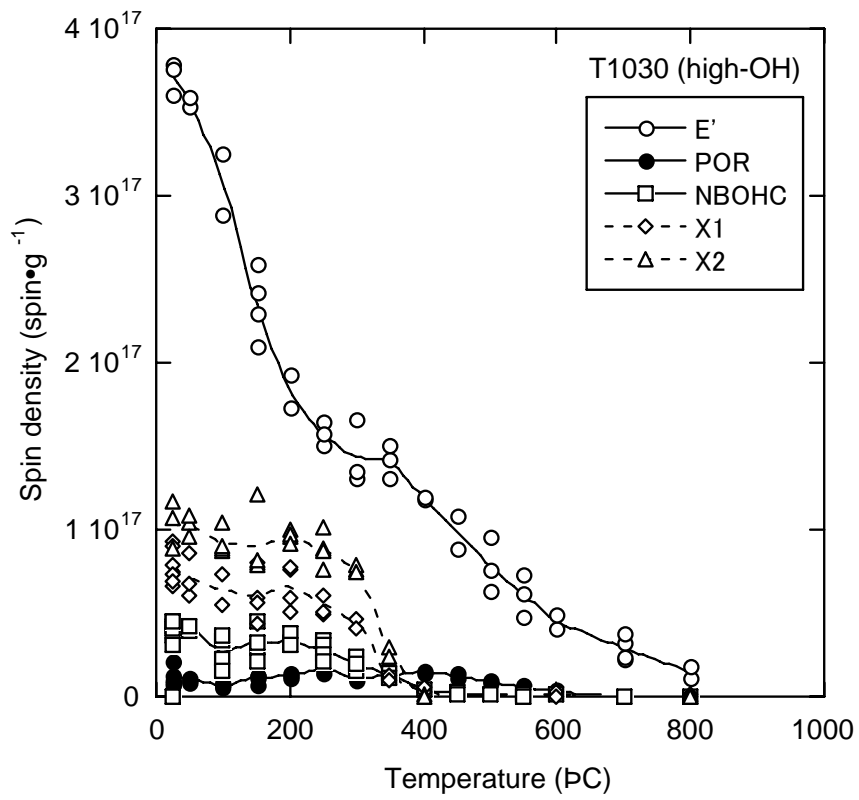
Fig. 5-4. Ten-minute isochronal anneal experiment of the neutron-irradiated high OH (T-1030) silica. Neutron fluence: 1.6×10^{16} n•cm^{-2}.
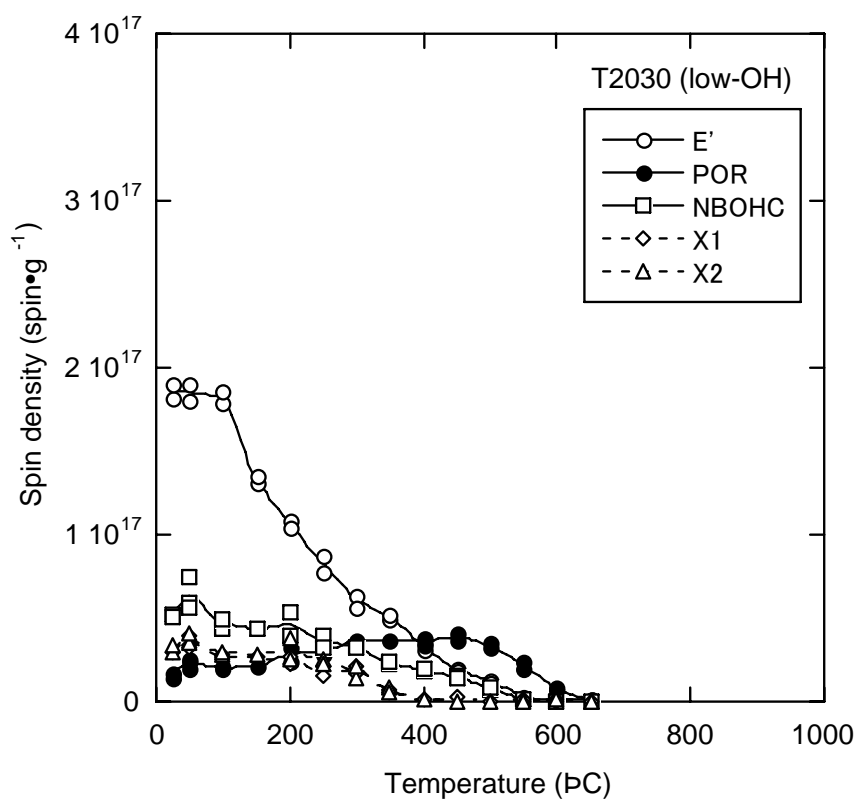
Fig. 5-5. Ten-minute isochronal anneal experiment of the neutron-irradiated low OH (T-2030) silica. Neutron fluence: 1.6×10^{16} n•cm^{-2}.
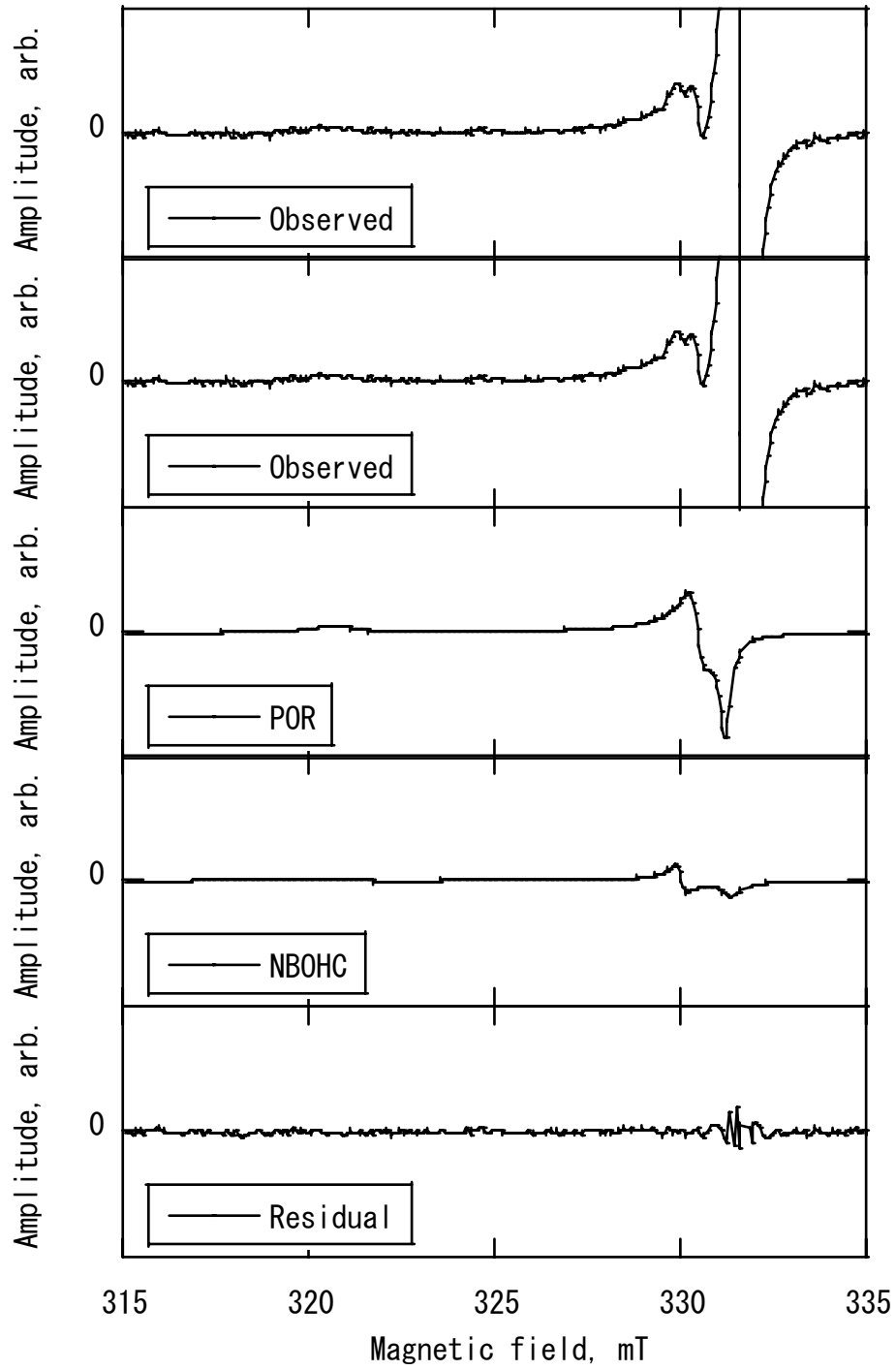
Fig.5-6. Typical X-band ESR spectrum of the 2 MeV He$^+$ irradiated vitreous silica (T-2030) and its components: (a) observed spectrum (2.0×10^{18} ions•m^{-2}), (b) E', (c) POR, (d) NBOHC, (e) others.
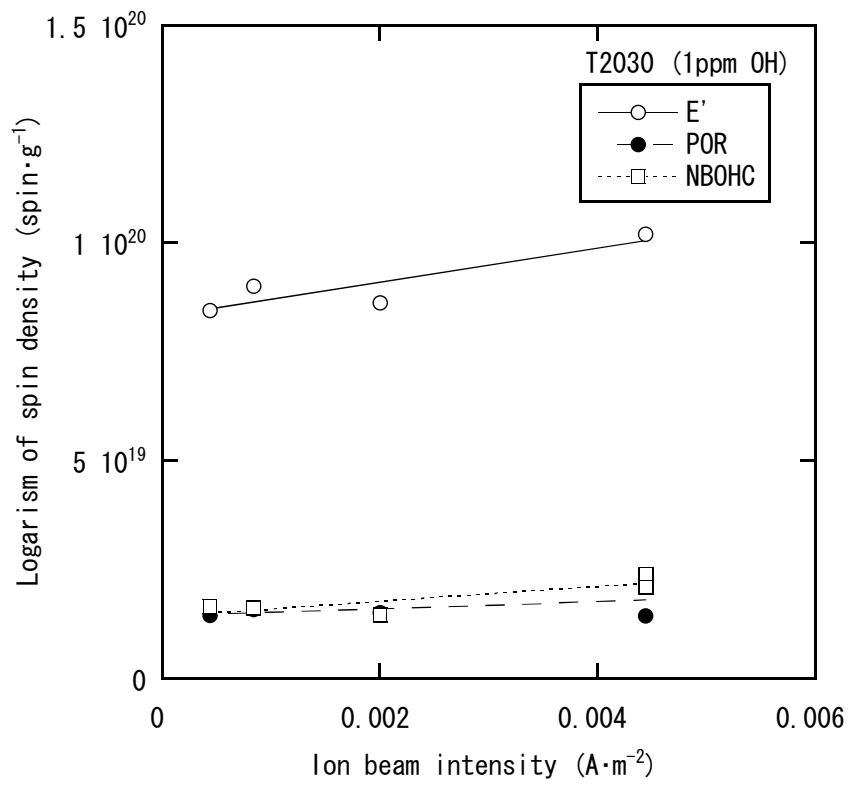
Fig. 5-7. Ion beam intensity dependence of spin densities in the 2 MeV He$^+$ irradiated vitreous silica (T-2030).   Dose: 1.5×10^{19} ions•m^{-2}.
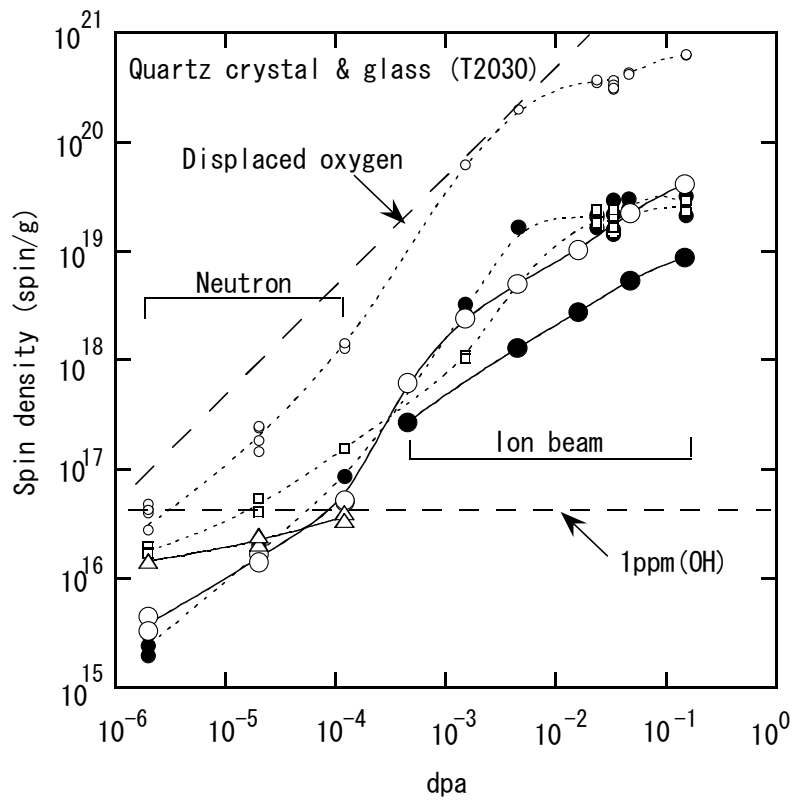
Fig. 5-8. Dpa dependence of spin densities in the 2 MeV He$^+$ irradiated and neutron irradiated vitreous silica (T-2030) and quartz crystal. Small marks are of vitreous silica and large ones of quartz crystal; open circles: E', full circles: POR, squares: NBOHC, triangles: others. Curves are drawn for aid of the eyes.
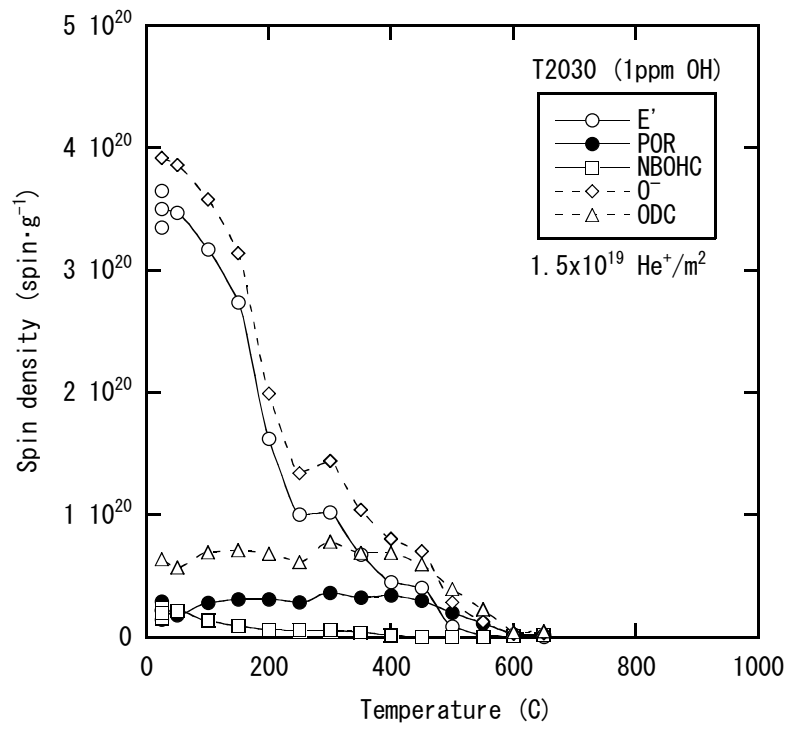
Fig. 5-9. Ten-minute isochronal anneal experiment of the 2 MeV He[+] irradiated vitreous silica (T-2030).   Dose: 1.5×10^{19} ions•m[-2].

91
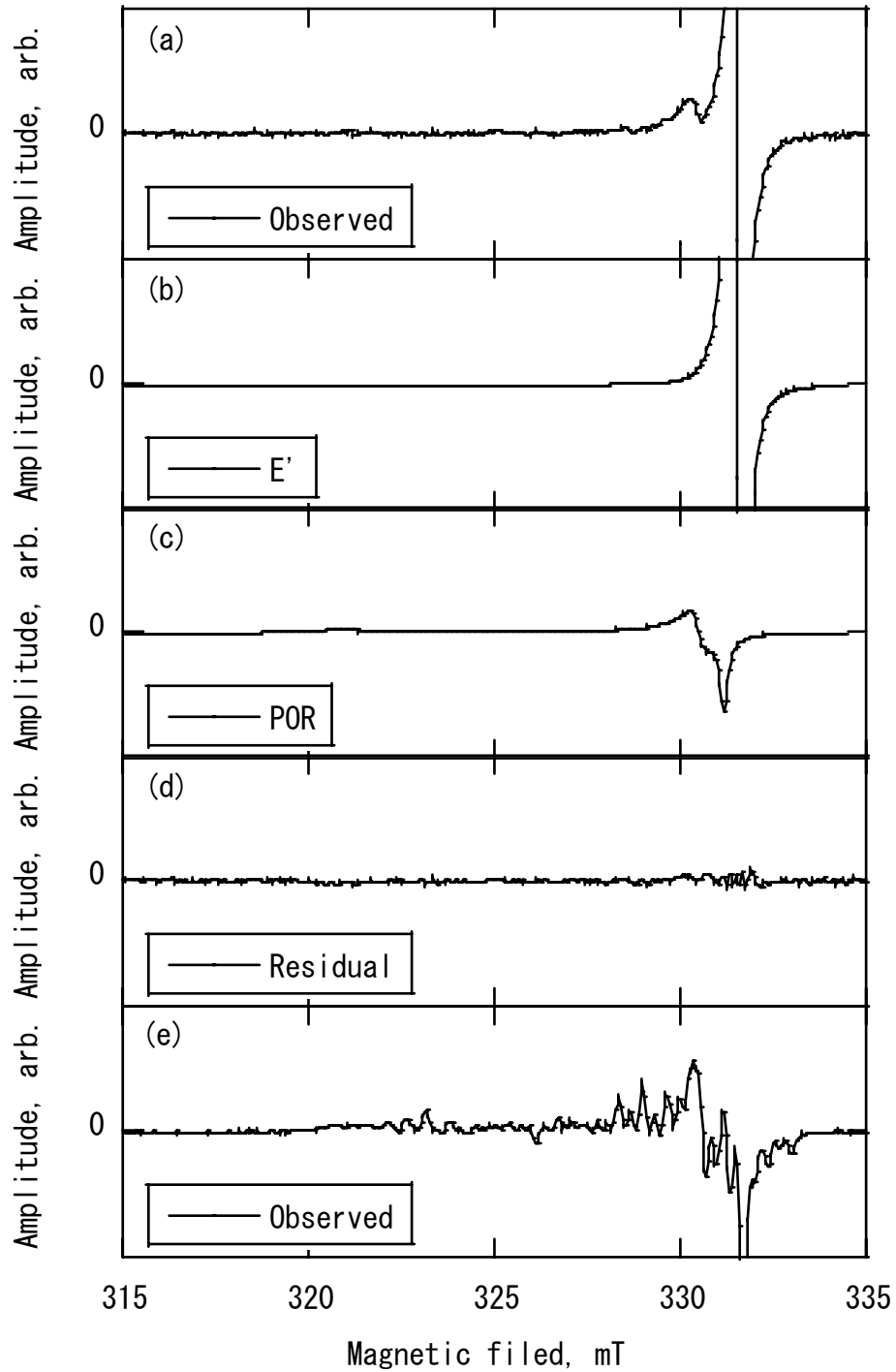
Fig. 5-10. Typical X-band ESR spectra of irradiated quartz crystal: (a) observed spectrum of the specimen irradiated by 2 MeV He$^+$ to 6.5×10^{19} ions•m^{-2}, (b) E', (c) POR, (d) others, and (e) observed spectrum with fast neutron irradiation to 2.2×10^{16} n•cm^{-2}.
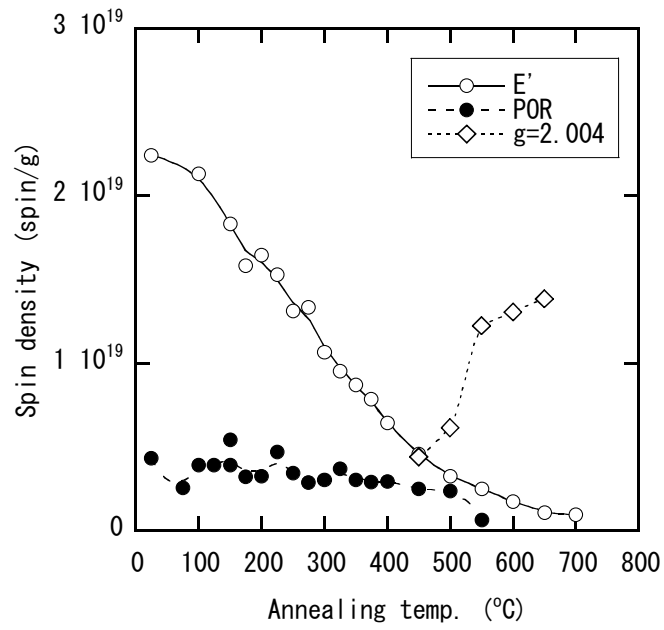
Fig. 5-11. Ten-minute isochronal anneal experiment of the 2 MeV He^{+} irradiated quartz crystal.   Dose: 6.5×10^{19} ions•m^{-2}.
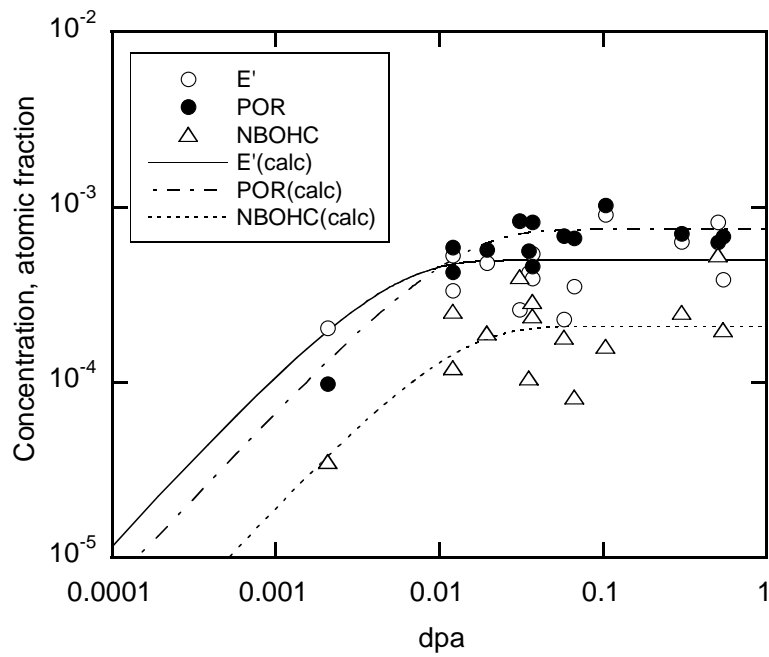
Fig. 5-12. Dpa dependence of spin densities in the 2 MeV He$^+$ irradiated vitreous silica (T-2030).   Ion beam intensity: around 6.0×10^{-4} to 1.3×10^{-3} A•m^{-2}.   Open circles: E', full circles: POR, squares: NBOHC, triangles.   Curves represent the calculated results.   See text for details.
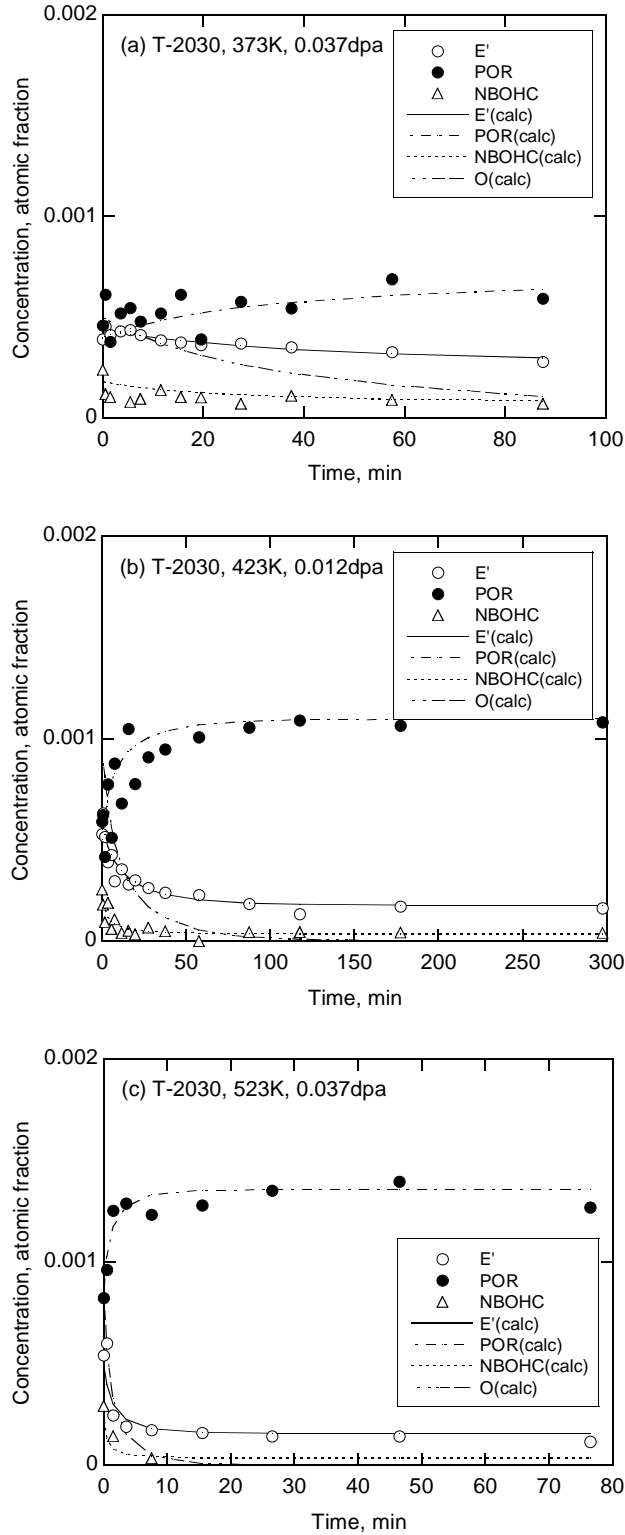
Fig. 5-13. Isothermal annealing behavior of radiation-induced defects in vitreous silica (T-2030) irradiated by 2 MeV He[+] ions at (a) 373K, (b) 423K, and (c) 523K. Marks are experimental and curves represent the least-squares fits of the data to Eqs. (5-21) – (5-23).

95
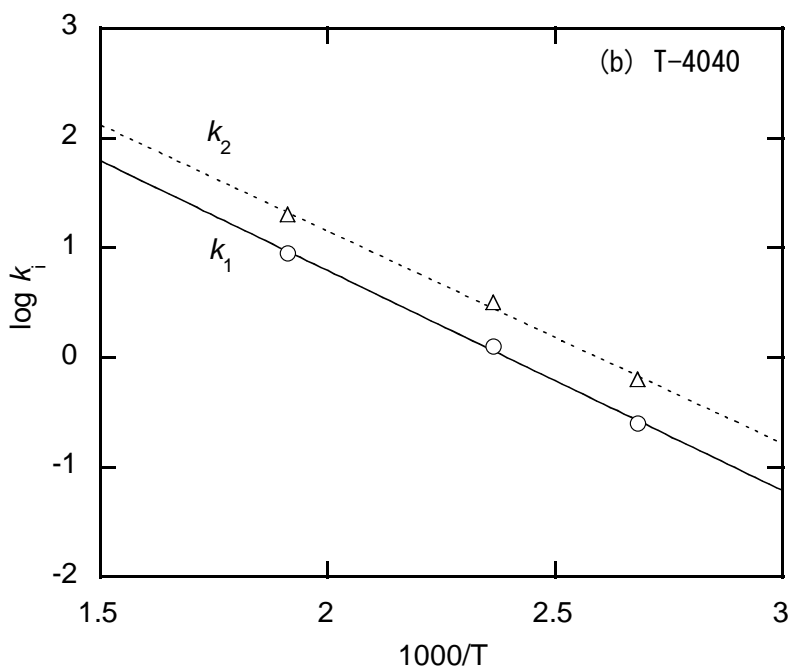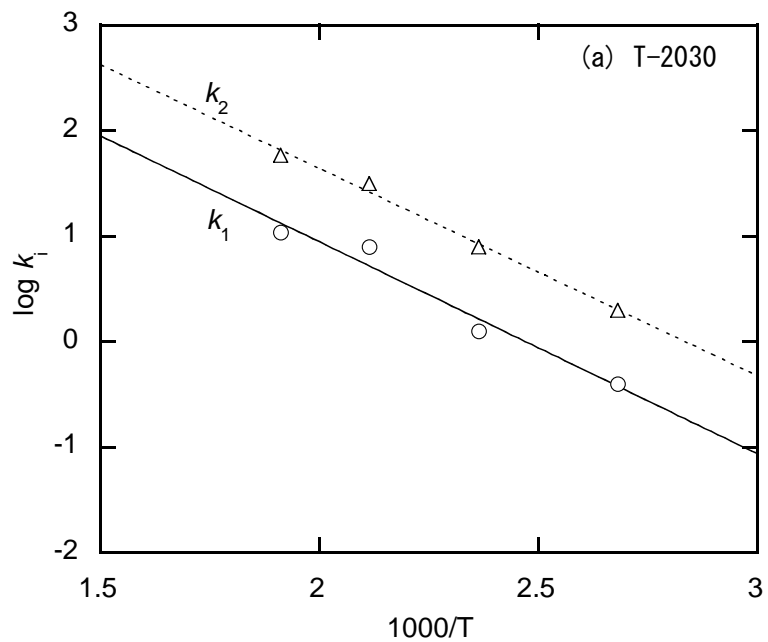
Fig. 5-14. Arrhenius plots of reaction rate constant k_1 and k_2 for (a) T-2030 and (b) T-4040. Marks are experimental and curves represent the least-squares fits of the data to the Arrhenius equations.

Chapter 6
General conclusions

The present study was performed to understand the mechanism of production and reaction mechanism of radiation-induced defects in some typical ceramic materials such as silica and alumina in relation with the effect of irradiation on tirium recovery.

In chapter 2, tritium release kinetics of lithium ortho- and metasilicates with irradiation defects was studied by out-of-pile experiments. Tritium was released mainly as HTO, but the HT yield increased with the increasing partial pressure of H_2 in the sweep gas. Some dependence of the HT yield on neutron fluence was observed. Tritium release kinetics of HTO and HT were well interpreted by taking a combined regime of diffusion and first-order reaction. The dependence of the diffusion constant and reaction rate constant on neutron fluence was determined. In the studied range, the effects of neutron fluence were observed more clearly for Li_2SiO_3 than for Li_4SiO_4, although those seemed essentially the same for the two materials.

In chapter 3, for the performance assessment of fusion reactor solid breeder materials, the production behavior of irradiation defects in the ternary lithium ceramics of Li_2SiO_3 and Li_4SiO_4 were studied by an in-situ luminescence measurement technique under ion beam irradiation of H^+ and He^+. For comparison the measurement was also performed using vitreous SiO_2. In the case of lithium silicates, the temperature dependence of the luminescence intensity and the transient behavior of the luminescence intensity on temperature changes were measured for kinetic aspects of the involved reactions, and the production mechanisms and kinetics of the irradiation defects in these lithium ceramics were determined. In the case of vitreous silica, no apparent difference was observed in the luminescence spectra of specimens of different OH contents. The temperature dependence of the luminescence intensity at 280 and 460nm was analyzed by considering the production mechanisms and kinetics of the irradiation defects of oxygen deficiency centers.

In chapter 4, the production behavior of irradiation defects in α-alumina and sapphire was studied by in-situ luminescence measurement technique under ion beam irradiation of H^+ and He^+. The luminescence intensity of F^+ centers at 330nm was observed to decrease monotonically with the increasing temperature up to 800K, while the intensity of F^0 centers at 410nm to show non-monotonic temperature dependence. In the latter case, the intensity decreased with the temperature up to 600K, and then increased above this temperature. It was also observed that the luminescence intensity at 410nm was lower in the He^+ irradiation than in the H^+ irradiation. By considering that the luminescence intensities represent the accumulated F^+ and F^0 centers, the observations were analyzed to obtain the rate constants for the production and reaction kinetics of radiation-induced defects of F-type centers.

In chapter 5, the electron spin resonance (ESR) measurement of irradiation defects in vitreous silica was performed. Together with the usual paramagnetic states of E' centers, non-bridging oxygen hole centers (NBOHCs), and peroxy radicals (PORs), some new states were observed in the ESR spectra, possibly due to O_2^- ions. The spin densities of the E'

centers, NBOHCs, and PORs were measured as a function of the dpa value and postirradiation thermal annealing temperature. The results of the ion beam irradiation were compared with those of neutron irradiation, and both results were consistently explained in terms of the dpa values. The spin densities of these centers were observed to saturate above the dpa value of 10^{-2}. In isothermal annealing experiments, sequential reactions of the E' centers with oxygen atoms to form the NBOHCs and PORs were observed to occur, and the rate constants and activation energies of those reactions were determined.

In chapter 6, the conclusions of these studies are summarized.

List of publications

Chapter 2

K. Moritani, T. Magari and H. Moriyama, Tritium Release Kinetics of Lithium Silicates with Irradiation Defects, Fusion Engng. Design 39-40 (1998) 675-683.

Chapter 3

K. Moritani, S. Tanaka, H. Moriyama, Production Behavior of Irradiation Defects in Lithium Silicates and Silica under Ion Beam Irradiation, J. Nucl. Mater. 281 (2000) 106-111.
K. Moritani, I. Takagi, H. Moriyama, "Production Behavior of Irradiation Defects in Vitreous Silica under Ion Beam Irradiation, J. Nucl. Mater. 312 (2003) 97-102.

Chapter 4

K. Moritani, I. Takagi, H. Moriyama, "Production Behavior of Irradiation Defects in α-alumina and sapphire under Ion Beam Irradiation, J. Nucl. Mater. 326 (2004) 106-113.
K. Moritani, Y. Teraoka, I. Takagi, M. Akiyoshi, H. Moriyama, Production and reaction kinetics of radiation-induced defects in α-alumina and sapphire under ion beam irradiation, J. Nucl. Mater. 373 (2008) 157-163.

Chapter 5

K. Moritani, I. Takagi, H. Moriyama, "Electron resonance measurement of irradiation-induced defects in vitreous silica", J. Nucl. Mater. 325 (2004) 169-173.
K. Moritani, I. Takagi, H. Moriyama, "Electron resonance measurement of irradiation defects in vitreous silica irradiated with neutrons and ion beams", J. Nucl. Mater. 329-333 (2004) 988-992.
K. Moritani, Y. Teraoka, I. Takagi, and H. Moriyama, "Electron Spin Resonance Measurement of Irradiation Defects Produced in Quartz Crystal", Nuclear Instruments and Methods in Physics Research B232 (2005) 317-321.
J. Takemoto, K. Moritani, I. Takagi, M. Akiyoshi, H. Moriyama, Electron spin resonance measurement of radiation-induced defects and reactions in vitreous silica irradiated with ion beams, J. Nucl. Mater. 374 (2008) 293-297.